Lecture Notes in Physics

The Editorial Policy for Monographs

The series Lecture Notes in Physics reports new developments in physical research and teaching - quickly, informally, and at a high level. The type of material considered for publication includes monographs presenting original research or new angles in a classical field. The timeliness of a manuscript is more important than its form, which may be preliminary or tentative. Manuscripts should be reasonably self-contained. They will often present not only results of the author(s) but also related work by other people and will provide sufficient motivation, examples, and applications.

Acceptance

The manuscripts or a detailed description thereof should be submitted either to one of the series editors or to the managing editor. The proposal is then carefully refereed. A final decision concerning publication can often only be made on the basis of the complete manuscript, but otherwise the editors will try to make a preliminary decision as definite as they can on the basis of the available information.

Contractual Aspects

Authors receive jointly 30 complimentary copies of their book. No royalty is paid on Lecture Notes in Physics volumes. But authors are entitled to purchase directly from Springer other books from Springer (excluding Hager and Landolt-Börnstein) at a $33\frac{1}{3}\%$ discount off the list price. Resale of such copies or of free copies is not permitted. Commitment to publish is made by a letter of interest rather than by signing a formal contract. Springer secures the copyright for each volume.

Manuscript Submission

Manuscripts should be no less than 100 and preferably no more than 400 pages in length. Final manuscripts should be in English. They should include a table of contents and an informative introduction accessible also to readers not particularly familiar with the topic treated. Authors are free to use the material in other publications. However, if extensive use is made elsewhere, the publisher should be informed. As a special service, we offer free of charge LaTeX macro packages to format the text according to Springer's quality requirements. We strongly recommend authors to make use of this offer, as the result will be a book of considerably improved technical quality. The books are hardbound, and quality paper appropriate to the needs of the author(s) is used. Publication time is about ten weeks. More than twenty years of experience guarantee authors the best possible service.

LNP Homepage (springerlink.com)

On the LNP homepage you will find:
−The LNP online archive. It contains the full texts (PDF) of all volumes published since 2000. Abstracts, table of contents and prefaces are accessible free of charge to everyone. Information about the availability of printed volumes can be obtained.
−The subscription information. The online archive is free of charge to all subscribers of the printed volumes.
−The editorial contacts, with respect to both scientific and technical matters.
−The author's / editor's instructions.

Carles Bona Carlos Palenzuela-Luque

Elements of Numerical Relativity

From Einstein's Equations to Black Hole Simulations

Springer

Authors

Carles Bona
Universidad Islas Baleares
Facultat Ciencias
Depto. Fisica
07071 Palma de Mallorca
Spain
Email: cbona@uib.es

Carlos Palenzuela-Luque
Louisiana State University
Center for Computation
and Technology
Baton Rouge, LA 70803
U.S.A.
Email: carlos@lsu.edu

Carles Bona, Carlos Palenzuela-Luque *Elements of Numerical Relativity*,
Lect. Notes Phys. 673 (Springer, Berlin Heidelberg 2005), DOI 10.1007/b135928

Library of Congress Control Number: 2005926241

ISSN 0075-8450
ISBN-10 3-540-25779-9 Springer Berlin Heidelberg New York
ISBN-13 978-3-540-25779-0 Springer Berlin Heidelberg New York

Springer is a part of Springer Science+Business Media
springeronline.com

Printed in The Netherlands

Typesetting: by the author and TechBooks using a Springer LaTeX macro package

Printed on acid-free paper SPIN: 11420293 56/TechBooks 5 4 3 2 1 0

To Montse, my dear wife and friend

Para mis padres, Francisco y Manuela,
que me enseñaron lo mas importante.
Y para mi amigo Jose y mi querida Eugenia,
que no han dejado que lo olvidara

Preface

We became involved with numerical relativity under very different circumstances. For one of us (C.B.) it dates back to about 1987, when the current Laser-Interferometer Gravitational Wave Observatories were just promising proposals. It was during a visit to Paris, at the Institut Henri Poincaré, where some colleagues were pushing the VIRGO proposal with such a contagious enthusiasm that I actually decided to reorient my career. The goal was to be ready, armed with a reliable numerical code, when the first detection data would arrive.

Allowing for my experience with the 3+1 formalism at that time, I started working on singularity-avoidant gauge conditions. Soon, I became interested in hyperbolic evolution formalisms. When trying to get some practical applications, I turned to numerical algorithms (a really big step for a theoretically oriented guy) and black hole initial data. More recently, I became interested in boundary conditions and, closing the circle, again in gauge conditions. The problem is that a reliable code needs all these ingredients to be working fine at the same time. It is like an orchestra, where strings, woodwinds, brass and percussion must play together in a harmonic way: a violin virtuoso, no matter how good, cannot play Vivaldi's *Four Seasons* by himself.

During that time, I have had many Ph.D. students. The most recent one is the other of us (C.P.). All of them started with some specific topic, but they needed a basic knowledge of all the remaining ones: you cannot work on the saxophone part unless you know what the bass is supposed to play at the same time.

This is where this book can be of a great help. Imagine a beginning graduate student armed only with a home PC. Imagine that the objective is to build a working numerical code for simple black-hole applications. This book should first provide him or her with a basic insight into the most relevant aspects of numerical relativity. But this is not enough; the book should also provide reliable and compatible choices for every component: evolution system, gauge, initial and boundary conditions, even for numerical algorithms.

This pragmatic orientation may cause this book to be seen as biased. But the idea was not to produce a compendium of the excellent work that has been made in numerical relativity during these years. The idea is rather to present a well-founded and convenient way for a beginner to get into the field. He or she will quickly discover everything else.

The structure of the book reflects the peculiarities of numerical relativity research:

- It is strongly rooted in theory. Einstein's relativity is a general-covariant theory. This means that we are building at the same time the solution and the coordinate system, a unique fact among physical theories. This point is stressed in the first chapter, which could be omitted by more experienced readers.
- It turns the theory upside down. General covariance implies that no specific coordinate is more special than the others, at least not a priori. But this is at odds with the way humans and computers usually model things: as functions (of space) that evolve in time. The second chapter is devoted to the evolution (or 3+1) formalism, which reconciles general relativity with our everyday perception of reality, in which time plays such a distinct role.
- It is a fertile domain, even from the theoretical point of view. The structure of Einstein's equations allows many ways of building well-posed evolution formalisms. Chapter 3 is devoted to those which are of first order in time but second order in space. Chapter 4 is devoted instead to those which are of first order both in time and in space. In both cases, suitable numerical algorithms are provided, although the most advanced ones apply mainly to the fully first order case.
- It is challenging. The last sections of Chaps. 5 and 6 contain front-edge developments on constraint-preserving boundary conditions and gauge pathologies, respectively. These are very active research topics, where new developments will soon improve on the ones presented here. The prudent reader is encouraged to look for updates of these front-edge areas in the current scientific literature.

A final word. Numerical relativity is not a matter of brute force. Just a PC, not a supercomputer, is required to perform the tests and applications proposed here. Numerical relativity is instead a matter of insight. Let wisdom be with you.

Palma de Mallorca,
April 2005

Carles Bona
Carlos Palenzuela Luque

Contents

1

The Four-Dimensional Spacetime

1.1 Spacetime Geometry

Physics theories are made by building mathematical models that correspond to physical systems. General Relativity, the physical theory of Gravitation, models spacetime in a geometrical way: as a four-dimensional manifold. The concept of manifold is just a generalization to the multidimensional case of the usual concept of a two-dimensional surface. This will allow us to apply the well known tools of differential geometry, the branch of mathematics which describes surfaces, to the study of spacetime geometry.

An extra complication comes from the fact that General Relativity laws are formulated in a completely general coordinate system (that is where the name of 'General' Relativity comes from). Special Relativity, instead, makes use of inertial reference frames, where the formulation of the physical laws is greatly simplified. This means that one has to learn how to distinguish between the genuine features of spacetime geometry and the misleading effects coming from arbitrary choices of the coordinate system. This is why the curvature tensor will play a central role, as we will see in what follows.

1.1.1 The Metric

We know from differential geometry that the most basic object in the spacetime geometrical description is the line element. In the case of surfaces, the line element tells us the length dl corresponding to an infinitesimal displacement between two points, which can be related by an infinitesimal change of the local coordinates x^k in the surface. In the case of the spacetime, the concept of length has to be generalized in order to include also displacements in time (which is usually taken to be the 'zero' coordinate, $x^0 \equiv ct$). This generalization is known as the 'interval' ds, which can be expressed in local coordinates as

$$ds^2 = g_{\mu\nu} dx^\mu dx^\nu \qquad (\mu, \nu = 0, 1, 2, 3) \; . \tag{1.1}$$

C. Bona and C. Palenzuela Luque: *Elements of Numerical Relativity*, Lect. Notes Phys. **673**, 1–17 (2005)
www.springerlink.com

We can easily see from (1.1) that the tensor $g_{\mu\nu}$ is going to play a central role. In the theory of surfaces, it has been usually called 'the first fundamental form'. In General Relativity it is more modestly called 'the metric' in order to emphasize its use as a tool to measure space and time intervals. The metric components can be displayed as a 4 by 4 matrix. This matrix is symmetric by construction (1.1), so that only 10 of the 16 coefficients are independent. Computing these 10 independent coefficients in a given spacetime domain is the goal of most Numerical Relativity calculations.

The metric tensor $g_{\mu\nu}$ is the basic field describing spacetime. One would need to introduce extra fields only if one wants to take into account non-gravitational interactions, like the electromagnetic or the hydrodynamical ones, but the gravitational interaction, as far as we know, can be fully described by the metric.

1.1.2 General Covariance

The most interesting property of the line element (1.1) is that it is invariant under generic (smooth) changes of the spacetime coordinates, namely

$$x^{\mu} = F^{\mu}(x^{\nu'}) \ . \tag{1.2}$$

This is because the values of space or time intervals are independent of the coordinate system one is using for labelling spacetime points. This means that the components of the metric must change in a suitable way in order to compensate the changes of the differential coefficients dx^{μ} in (1.1),

$$g_{\mu'\nu'} = g_{\mu\nu} \frac{\partial x^{\mu}}{\partial x^{\mu'}} \frac{\partial x^{\nu}}{\partial x^{\nu'}} \ . \tag{1.3}$$

We will say then that the metric transforms in a covariant way or, more briefly, that it behaves as a covariant tensor field under the general coordinate transformations (1.2).

The general covariance (1.3) of the metric means that, without altering the properties of spacetime, one can choose specific coordinate systems that enforce some interesting conditions on the metric coefficients. One can choose for instance any given (regular) spacetime point P and devise a coordinate system such that

$$g_{\mu'\nu'} \,|_{\mathrm{P}} = diag\{-c^2, +1, +1, +1\} \qquad \partial_{\rho'} \, g_{\mu'\nu'} \,|_{\mathrm{P}} = 0 \tag{1.4}$$

(local inertial coordinate system at P). This means that Special Relativity holds true locally (in the strongest sense: a single point at a time), and it will also be of great help in shortening some proofs by removing the complication of having to deal with arbitrary coordinate systems.

At this point, we must notice some ambiguity which affects to the very meaning of the term 'solution'. In the geometrical approach, one solution

corresponds to one spacetime, so that metric coefficients that can be related by the covariant transformation (1.3) are supposed to describe the same metric, considered as an intrinsic tensor, independent of the coordinate system. In this sense, we can see how in exact solutions books (see for instance [1]) different forms of the same metric appear, as discovered by different authors. In the differential equations approach, however, the term solution applies to every set of metric components that actually verifies the field equations, even if there could be some symmetry (coordinate or 'gauge') transformation relating one of these 'solutions' to another.

This is by no way a mere philosophical distinction. If General Relativity has to be (as it is) general covariant, then the field equations must have two related properties:

- The equations must be unable to fully determine all the metric coefficients. Otherwise there would be no place for the four degrees of freedom corresponding to the general covariant coordinate (gauge) transformations (1.3).
- The equations must not prescribe any way of choosing the four spacetime coordinates. Otherwise there will be preferred coordinate systems and general covariance would be broken.

But in Numerical Relativity there is no way of getting a solution without computing the values of every metric component. This means that the differential system obtained from just the field equations is not complete, and one must prescribe suitable coordinate conditions before any numerical calculation can be made. The mathematical properties of the resulting complete system will of course depend of this choice of the coordinate gauge. We will come back to this point later.

1.1.3 Covariant Derivatives

The very concept of derivative intrinsically involves the comparison of field values at neighboring points. The prize one has to pay for using arbitrary coordinate systems is that one can no longer compare just field components at different points: one must also compensate for the changes of the coordinate basis when going from one point to another. In this way we can interpret the two contributions that arise when computing the covariant derivative of a vector field:

$$\nabla_\mu v^\nu = \partial_\mu v^\nu + \Gamma^\nu_{\rho\mu} v^\rho \, . \tag{1.5}$$

The first term corresponds to the ordinary partial derivatives of the field components, whereas the second one takes into account the variation of the coordinate basis used for computing these components. The Γ symbols in (1.5) are known as 'connection coefficients' because they actually allow to compare fields at neighboring points.

The covariant derivative of tensors with 'downstairs' indices contains connection terms with the opposite sign ('downstairs' components correspond to the dual basis). In the case of the metric, for instance, one has

$$\nabla_\rho g_{\mu\nu} = \partial_\rho g_{\mu\nu} - \Gamma^\sigma_{\ \rho\mu} g_{\sigma\nu} - \Gamma^\sigma_{\ \rho\nu} g_{\mu\sigma} \tag{1.6}$$

(notice that every additional index needs its own connection term).

The connection coefficients $\Gamma^\rho_{\ \mu\nu}$ are not tensor fields. They transform under a general coordinate transformation (1.2) in the following way:

$$\Gamma^{\rho'}_{\ \ \mu'\nu'} = \frac{\partial x^{\rho'}}{\partial x^\rho} \left[\Gamma^\rho_{\ \mu\nu} \frac{\partial x^\mu}{\partial x^{\mu'}} \frac{\partial x^\nu}{\partial x^{\nu'}} + \frac{\partial^2 x^\rho}{\partial x^{\mu'} \partial x^{\nu'}} \right] . \tag{1.7}$$

The additional second derivatives terms appearing in (1.7) compensate exactly the analogous terms arising in the transformation of the partial derivative contributions in (1.5, 1.6), so that the covariant derivative of a tensor field is again a tensor field. Notice, however, that the extra second derivatives terms in (1.7) are symmetric in the lower indices. This means that the antisymmetric combinations

$$\Gamma^\rho_{\ [\mu\nu]} \equiv \frac{1}{2} \left(\Gamma^\rho_{\ \mu\nu} - \Gamma^\rho_{\ \nu\mu} \right) \tag{1.8}$$

correspond to the components of a tensor field (torsion tensor), because the antisymmetric part of the second derivatives terms in (1.7) actually vanishes.

Coming back to the metric tensor, the fact that the transformation of its first partial derivatives includes both first and second derivatives terms is the reason why one can define at any fixed point P the locally inertial coordinate system in such a way that both conditions in (1.4) hold true. It is natural to assume that the connection coefficients should also vanish in the local inertial system at P, in order to make sure that Special Relativity is fully recovered locally. These conditions imply that, in the local inertial coordinate system at P:

- The torsion (1.8) vanishes
$$\Gamma^\rho_{\ [\mu\nu]} = 0 . \tag{1.9}$$
- The metric is preserved by covariant differentiation
$$\nabla_\rho g_{\mu\nu} = 0 . \tag{1.10}$$

Notice that both (1.9) and (1.10) are tensor equations. And the vanishing of any tensor quantity in a local inertial system implies that it must actually vanish in any other coordinate system. This fact, allowing for (1.6), provides a very useful expression for the connection coefficients in terms of the first derivatives of the metric components:

$$\Gamma^\sigma_{\ \mu\nu} = \frac{1}{2} g^{\sigma\rho} [\partial_\mu g_{\rho\nu} + \partial_\nu g_{\mu\rho} - \partial_\rho g_{\mu\nu}] \tag{1.11}$$

(Christoffel symbols), where we have noted with 'upstairs' indices the components of the inverse matrix of the metric, namely

$$g^{\mu\rho} g_{\rho\nu} = \delta^{\mu}_{\ \nu} \ . \tag{1.12}$$

1.1.4 Curvature

Up to this point, all we have said could perfectly apply to the Special Relativity (Minkowski) spacetime. All the complications with covariant derivatives and connection coefficients could arise just from using non-inertial coordinate systems. Minkowski spacetime is said to be flat because a further specialization of the local inertial coordinate system can make the metric form (1.4) to apply for all spacetime points P simultaneously.

In General Relativity, in contrast, gravity is seen as the effect of spacetime curvature. So one must distinguish between the intrinsic effects of curvature (gravitation) and the sort of 'inertia forces' arising from weird choices of coordinate systems. Here again, this is a very well known problem from surface theory. The curvature of a surface can be represented by its curvature tensor (Riemann tensor, as it is known in General Relativity), which can be defined as follows:

$$(\nabla_\rho \nabla_\sigma - \nabla_\sigma \nabla_\rho)\, v^\mu = R^{\mu}_{\ \nu\rho\sigma} v^\nu \ , \tag{1.13}$$

so that it can be interpreted as a measure of the non-commutativity of (covariant) derivatives: a property that characterizes true curved spacetimes. The Riemann tensor $R^{\mu}_{\ \nu\rho\sigma}$ defined by (1.13) can be explicitly computed, allowing for (1.5), in terms of the connection coefficients:

$$R^{\mu}_{\ \nu\rho\sigma} = \partial_\rho \Gamma^{\mu}_{\ \sigma\nu} - \partial_\sigma \Gamma^{\mu}_{\ \rho\nu} + \Gamma^{\mu}_{\ \rho\lambda} \Gamma^{\lambda}_{\ \sigma\nu} - \Gamma^{\mu}_{\ \sigma\lambda} \Gamma^{\lambda}_{\ \rho\nu} \ . \tag{1.14}$$

It is clear from (1.14) that in a flat spacetime, where there exists a coordinate system in which all connection coefficients vanish everywhere, the curvature tensor is zero, namely

$$R^{\mu}_{\ \nu\rho\sigma} = 0 \tag{1.15}$$

and, like any other tensor equation, it holds in any other coordinate system. Conversely, if the tensor condition (1.15) does not hold, then (1.14) tells us that there can not be any coordinate system in which all connection coefficients vanish everywhere and the manifold considered is not flat. It follows that (1.15) is a necessary and sufficient condition for a given spacetime to be flat. So finally we have one intrinsic and straightforward way to distinguish between genuine curved spaces and flat spaces 'disguised' in arbitrary coordinate systems.

1.1.5 Symmetries of the Curvature Tensor

Riemann curvature tensor is a four-index object. In four-dimensional spacetime, this could lead up to $4^4 = 256$ components. Of course there are algebraic symmetries that contribute to reduce the number of its independent components. Part of these symmetries can be directly obtained from the generic definition (1.14), which holds for arbitrary connection coefficients. The remaining ones come from taking into account the relationship (1.11) between the connection coefficients and the metric tensor. We have summarized them in Table 1.1.

Table 1.1. Algebraic symmetries of the Curvature tensor

Generic Case Symmetries	Metric Connection (1.11)
$R^{\mu}{}_{\nu\rho\sigma} = -R^{\mu}{}_{\nu\sigma\rho}$	$R_{\mu\nu\rho\sigma} = -R_{\nu\mu\rho\sigma}$
$R^{\mu}{}_{\nu\rho\sigma} + R^{\mu}{}_{\rho\sigma\nu} + R^{\mu}{}_{\sigma\nu\rho} = 0$	$R_{\mu\nu\rho\sigma} = R_{\rho\sigma\mu\nu}$

But, even taking all these symmetries into account, one has still 20 algebraically independent components to deal with. One can easily realize, however, that lower rank tensors can be obtained by index contraction from the Riemann tensor. Allowing for the algebraic symmetries, there is only one independent way of contracting a pair of indices of the curvature tensor, namely

$$R_{\mu\nu} \equiv R^{\lambda}{}_{\mu\lambda\nu} \ , \tag{1.16}$$

which is known as 'Ricci tensor' in General Relativity. It follows from the algebraic properties of the Riemann tensor that (1.16) is symmetric in its two indices, so it has only 10 independent components. Contracting again in the same way, one can get the Ricci scalar

$$R \equiv R^{\lambda}_{\ \lambda} = R^{\rho\sigma}_{\ \ \rho\sigma} \ . \tag{1.17}$$

The Ricci tensor (1.16) and the Ricci scalar (1.17) play a major role when trying to relate curvature with the energy content of spacetime. In three-dimensional manifolds, the Ricci tensor allows to obtain algebraically all the components of the curvature tensor (both of them have only six independent components). In the four-dimensional case this is no longer possible: the importance of the Ricci tensor comes instead from the Bianchi identities,

$$\nabla_{\lambda} R^{\mu}{}_{\nu\rho\sigma} + \nabla_{\rho} R^{\mu}{}_{\nu\sigma\lambda} + \nabla_{\sigma} R^{\mu}{}_{\nu\lambda\rho} = 0 \ , \tag{1.18}$$

which can be obtained directly from (1.14). One can contract two pairs of indices in (1.18) in order to get the following 'contracted Bianchi identity' for the Ricci tensor

$$\nabla_\mu \left[R^{\mu\nu} - \frac{R}{2}\, g^{\mu\nu} \right] = 0 \,, \tag{1.19}$$

which can be interpreted as a covariant conservation law for the combination

$$G_{\mu\nu} \equiv R_{\mu\nu} - \frac{R}{2}\, g_{\mu\nu} \,, \tag{1.20}$$

which is known as the Einstein tensor.

1.2 General Covariant Field Equations

General Relativity is a metric theory of Gravitation. This means that the physical effects of Gravitation are identified with the geometrical effects of spacetime curvature. We have seen in the previous section how to describe spacetime curvature in a general covariant way, so that there are no preferred coordinate systems. In this section, we will see how to incorporate the effect of matter and non-gravitational fields. We will need first to generalize their Special Relativity description, which is made in terms of inertial reference frames, to general coordinate systems. Then, we will see how the energy content of these fields can be used as a source of spacetime curvature in Einstein's theory and the complexity of the resulting field equations, which motivates the use of some approximation techniques. Numerical approximations are singled out as the general-purpose ones, without any underlying physical assumption which could restrict its domain of applicability.

1.2.1 The Stress-Energy Tensor

In Special Relativity, the energy content of both matter and fields is described by a symmetric tensor $T^{\mu\nu}$ (stress-energy tensor). For instance, in the case of an ideal fluid, where one neglects heat transfer, viscosity and non-isotropic pressure effects, the stress energy tensor can be written as

$$T^{\mu\nu} = \tau\, u^\mu u^\nu + p\, (g^{\mu\nu} + u^\mu u^\nu) \,, \tag{1.21}$$

where u^μ is the fluid four-velocity

$$u^\mu = \gamma\, (1, \boldsymbol{v}) \tag{1.22}$$

(we are using geometrized units, so that $c = 1$), and τ and p are, respectively, the energy density and the isotropic pressure of the fluid in the comoving reference frame ($\boldsymbol{v} = 0$), where the stress-energy tensor could be written as

$$T^{\mu\nu} = diag(\tau, p\,, p\,, p\,) \,, \tag{1.23}$$

so that one can read directly the stress (isotropic pressure in this case) contribution in the space components and the energy contribution in the time

component. The neglecting of heat transfer implies that there can not be momentum contributions in the comoving frame.

Energy and momentum conservation in Special Relativity is translated into a conservation law for $T^{\mu\nu}$, which can be written in differential form as

$$\partial_\nu T^{\mu\nu} = 0 \, . \tag{1.24}$$

In the ideal fluid case (1.21), one can easily recover from (1.24) (the special relativistic versions of) the continuity equation and the Euler equation for ideal fluids. But (1.24) is a basic conservation law, valid in the general case, not just for the ideal fluid one. It is then natural to generalize (1.24) as

$$\nabla_\nu T^{\mu\nu} = 0 \, , \tag{1.25}$$

so that one gets a general covariant law with the right special relativistic limit. And one is ready now to incorporate the stress-energy tensor into the General Relativity framework.

1.2.2 Einstein's Field Equations

The general covariant conservation laws of both the Einstein and the stress-energy tensors (1.19, 1.25) provide good candidates to relate curvature with the spacetime energy content. General Relativity, Einstein's theory of Gravitation, is obtained when one imposes the direct relationship (Einstein's field equations):

$$G^{\mu\nu} = 8\pi \, T^{\mu\nu} \, , \tag{1.26}$$

where the 8π factor comes out from the Newtonian Gravitation limit (we are using here geometrical units so that both the gravitational constant G and light speed c are equal to unity).

We can read (1.26) from right to left, concluding that matter or any kind of physical field acts as a gravitational source which determines the local geometry of spacetime. In this sense, solving (1.26) as the field equations, will amount to determine the metric corresponding to a given matter and energy distribution.

But, conversely, we can also read (1.26) from left to right, noticing that the physical conservation law (1.25) can be now understood as mere consequence of (1.26) if one allows for the Bianchi identities (1.19). This means that the motion of matter under the action of gravitation is also governed by Einstein's equations. For instance, if we consider a dust-like test fluid, that is an ideal fluid of incoherent (zero pressure) particles which is insensitive to any interaction other than gravitation, it follows from (1.21, 1.25) that

$$u^\nu \nabla_\nu u^\mu = 0 \, . \tag{1.27}$$

The equation of motion (1.27) amounts to impose that the test particles move along the geodesic lines of spacetime geometry:

$$\frac{d^2x^\mu}{d\lambda^2} + \Gamma^\mu_{\rho\sigma}\frac{dx^\rho}{d\lambda}\frac{dx^\sigma}{d\lambda} = 0\ . \tag{1.28}$$

Geodesic lines are the natural generalization of straight lines for curved spacetime (lines whose tangent vector is constant, and minimal length lines also).

As far as in Newton first law straight spacetime lines correspond to the inertial motion of free particles, equation (1.27) can be interpreted as stating that test particles in a gravitational field are also in inertial motion, but following the 'straight lines' (geodesics) of the curved spacetime geometry. Gravitation is not considered then just as one more interaction, like electromagnetism or nuclear forces, but it is identified with spacetime curvature.

Coming back to the field equations (1.26), the Bianchi identities (1.19) allow us to write

$$\nabla_0(G^{0\nu} - 8\pi\, T^{0\nu}) + \nabla_k(G^{k\nu} - 8\pi\, T^{k\nu}) = 0 \qquad (k = 1, 2, 3)\ , \tag{1.29}$$

where latin indices will refer to space coordinates. This means that the subset of 4 Einstein's equations with at least one time component, namely

$$G^{0\nu} = 8\pi\, T^{0\nu}\ , \tag{1.30}$$

are first integrals of the system: they get preserved forever provided that the remaining 6 equations hold true everywhere (you can prove it first for the three space components and, allowing for the result, complete then the proof for the time one). This implies that only 6 of the 10 Einstein field equations are actually independent, so that the equations do not contain enough information to determine all of the 10 independent metric coefficients, as expected from the general covariance of the theory (see Sect. 1.1.2). We will be more precise about that point in the next chapter.

1.2.3 Structure of the Field Equations

From now on, we will look at Einstein's equations as a set of differential equations that one must solve for the spacetime metric once the energy content of spacetime is known. It is more convenient for this purpose to write (1.26) in the equivalent form

$$R_{\mu\nu} = 8\pi\left(T_{\mu\nu} - \frac{1}{2}\,T^\lambda_\lambda\, g_{\mu\nu}\right)\ , \tag{1.31}$$

that is, allowing for (1.14, 1.16),

$$\partial_\rho\Gamma^\rho_{\mu\nu} - \partial_\mu\Gamma^\rho_{\rho\nu} + \Gamma^\rho_{\rho\lambda}\Gamma^\lambda_{\mu\nu} - \Gamma^\rho_{\lambda\mu}\Gamma^\lambda_{\rho\nu} = 8\pi\left(T_{\mu\nu} - \frac{1}{2}\,T^\lambda_\lambda\, g_{\mu\nu}\right)\ , \tag{1.32}$$

where we must remember here the dependence of the connection coefficients on the metric (1.11), namely

$$\Gamma^{\sigma}_{\ \mu\nu} = \frac{1}{2}\, g^{\sigma\rho}[\partial_\mu g_{\rho\nu} + \partial_\nu g_{\mu\rho} - \partial_\rho g_{\mu\nu}] \,. \tag{1.33}$$

It is clear that (1.32) is a non-linear system of second order differential equations on the metric tensor. This means that generic solutions must have continuous first derivatives (metric coefficients must be smooth). This point is important when one tries to build up composite solutions, covering different regions of spacetime, by matching local solutions which hold only on one of such regions. This is a very common situation in local field theories, like electromagnetism, where different solutions are obtained for the 'interior' region, inside the charge distribution, and the 'exterior' or outside one. In the General Relativity case, the matching conditions for the composite solution to be valid amount to the continuity of the metric tensor and its first partial derivatives.

A closer look to (1.32) allows one to notice that the 'principal part' (the terms containing the highest order derivatives) can be put into Flux-Conservative form, that is as a four-divergence, namely

$$\partial_\rho[\Gamma^{\rho}_{\ \mu\nu} - \delta^{\rho}_{\ \mu}\Gamma^{\sigma}_{\ \sigma\nu}] \,. \tag{1.34}$$

This means that one can interpret (1.32) as a system of balance laws, like in fluid dynamics, with the principal part terms (1.34) describing transport and the remaining ones acting as sources. The right-hand-side terms, given by the stress-energy tensor, would describe sources of non-gravitational nature whereas the quadratic terms on the left-hand-side

$$\Gamma^{\rho}_{\ \rho\lambda}\Gamma^{\lambda}_{\ \mu\nu} - \Gamma^{\rho}_{\ \lambda\mu}\Gamma^{\lambda}_{\ \rho\nu} \,. \tag{1.35}$$

would describe the action of the gravitational field itself, acting as its own source.

One must be very careful, however, with the physical interpretation, because the splitting of the left-hand-side terms is not unique. Notice for instance that

$$\Gamma^{\rho}_{\ \rho\mu} = \frac{1}{2}\, g^{\sigma\rho}\partial_\mu g_{\sigma\rho} = \partial_\mu ln(\sqrt{g}) \,, \tag{1.36}$$

where g stands here for the absolute value of the determinant of the metric. This allows to rearrange terms in (1.32) so that the principal part can be written as

$$\frac{1}{\sqrt{g}}\, \partial_\rho[\sqrt{g}\,(\Gamma^{\rho}_{\ \mu\nu} - \delta^{\rho}_{\ \mu}\Gamma^{\sigma}_{\ \sigma\nu})] \,, \tag{1.37}$$

and the remaining quadratic terms are now

$$\Gamma^{\rho}_{\ \rho\mu}\Gamma^{\sigma}_{\ \sigma\nu} - \Gamma^{\rho}_{\ \lambda\mu}\Gamma^{\lambda}_{\ \rho\nu} \,, \tag{1.38}$$

instead of (1.34) and (1.35), respectively.

On the other side, from the Numerical Relativity point of view, the balance law structure of (1.32) is a blessing, because one can benefit of the experience

and results from a much more mature field: Computational Fluid Dynamics (CFD). This does not mean that all CFD techniques will work fine when applied directly to Numerical Relativity, but at least one has a very good guidance, based on years of research. We will take advantage of this fact in our numerical simulations.

For instance, one can notice that the flux-conservative structure of the principal part of the equations allows 'weak solutions'. In the case of General Relativity, this means that the metric could have first partial derivatives which are just piecewise continuous. Derivatives across the discontinuity surfaces would lead to Dirac delta terms, so that the requirement that such delta terms cancel out exactly in the field equations (1.31), when interpreted in the sense of distributions, provides the time evolution of these surfaces. It follows that the discontinuity surfaces ('gravitational shock waves') must propagate with light speed.

The use we are making of the term 'shock waves' is just inspired in Fluid Dynamics, but is not fully justified here. This is because the principal part of our equations (1.32) does not contain products of the connection coefficients with their derivatives so that, in the case of weak solutions, the Dirac delta terms appear always multiplied by continuous factors. This is in contrast with the usual situation in Fluid Dynamics, where the principal part of the Euler equation contains convective terms of the form

$$v^k \nabla_k v^i \,, \tag{1.39}$$

so that discontinuities in the fluid speed $\boldsymbol{v}$ lead to Dirac delta terms with discontinuous coefficients.

Equations that, like Euler equation, contain that kind of stronger non-linearities in the principal part are said to be 'genuine non-linear' whereas equations that, like Einstein's equations, do not contain them are said to be 'degenerate'. This is not a mere terminological distinction. In the genuine non-linear case, shocks can develop even from smooth initial data and their propagation speed can be either higher or lower than the characteristic speed (sound speed in Fluid Dynamics, where one can get either supersonic or subsonic waves). In the degenerate case, in contrast, discontinuities can never arise from smooth initial data and their propagation speed is always the characteristic one (light speed in General Relativity). In the Fluid Dynamics language, these are just 'contact discontinuities' instead of genuine shocks.

This discussion seems to suggest that Einstein's equations are in some sense easier than Euler or Navier-Stokes equations for Fluid Dynamics. This is true only if we look at the non-linearities of these equations from the qualitative point of view. But the situation is completely reversed if we look at it from the quantitative point of view. Remember that the basic quantities in (1.31) are not the connection coefficients, but the metric tensor. And notice that the metric derivatives in the expression (1.33) are always multiplied by the coefficients $g^{\rho\sigma}$ of the inverse matrix of the metric.

Every such coefficient is computed as the adjoint of the corresponding metric component (six terms) divided by the metric determinant (24 terms). Every index contraction involves the ten components of the inverse metric, that is 60 terms (plus the 24 terms denominator). Now, two index contractions are required in the quadratic contributions

$$\Gamma^{\rho}_{\lambda\mu}\Gamma^{\lambda}_{\rho\nu} \tag{1.40}$$

in (1.35). For every fixed value of μ and ν, we can expand (1.40) in terms of first metric derivatives: five such double contractions appear. This makes $5 \times 60^2 = 18000$ terms (denominators apart) per equation, that is 1.8 10^5 terms for the whole system (allowing for every value of μ and ν).

A similar estimate of the remaining contributions (including second derivatives and matter terms) can raise the count up to about 2.3 10^5 in the full general case (if one multiplies everything by the square of the metric determinant in order to remove all denominators). These quarter-of-million terms provide one of the reasons why Einstein's equations deserve their reputation as possibly the hardest ones in their class.

1.3 Einstein's Equations Solutions

1.3.1 Symmetries. Lie Derivatives

A useful strategy for simplifying the field equations system is to focus on particular solutions with some kind of symmetry. It is well known that, by adapting the coordinate system to a given symmetry of the solution, one can usually reduce the number of relevant coordinates. For instance, in the case of axial symmetry, one can take the azimuthal angle ϕ to be one of the four spacetime coordinates so that in this adapted coordinate system one has

$$\partial_\phi g_{\mu\nu} = 0 \,, \tag{1.41}$$

and the field equations can then be written in a simpler form.

As a consequence of (1.41), all the geometrical objects that can be derived from the metric without further inputs, like the curvature tensor, must share the same symmetry, namely

$$\partial_\phi R^{\mu}_{\nu\rho\sigma} = 0 \,. \tag{1.42}$$

Then, allowing for Einstein's field equations (1.31), all the physical quantities that can be computed, without further input, from the stress-energy tensor and the metric must also share the same symmetry. In the ideal fluid case (1.21), for instance, one has

$$\partial_\phi \, \tau = \partial_\phi \, p = 0 \,, \qquad \partial_\phi \, u^\mu = 0 \,, \tag{1.43}$$

so that any dependence on the azimuthal angle ϕ disappears (ϕ is an 'ignorable' coordinate).

From the group-theoretical point of view, we can identify ϕ with the parameter labelling a continuous group of transformations (rotations around one axis in this case), which is usually known as a 'Lie group'. These transformations can be interpreted as mapping every spacetime point P into a continuous set of points, one for every value of ϕ. This set of image points of a single one P defines an orbit of the group. As far as the mapping is continuous, this orbit is a curve on the manifold and one can compute its tangent vector field $\boldsymbol{\xi}$, which is known as the group generator. For instance, the vector field $\boldsymbol{\xi}$ that generates axial symmetry gets a trivial form in the adapted coordinate system, namely

$$\xi^\mu = \delta^\mu_{(\phi)} \,. \tag{1.44}$$

This group-theoretical considerations will help us in generalizing expressions like (1.41–1.44), which are valid only in the adapted coordinate system, to a general one, in keeping with the general covariance of the theory. The standard recipe of changing partial derivatives into covariant ones will not work here, because the basic equation (1.41) would be transformed in that way into an identity, valid for any spacetime independently of its symmetry properties.

The right generalization is based on the fact that the group orbits fill out spacetime: every point P is contained into its own orbit. This implies that one can just compare any tensor at P with its image under an infinitesimal transformation of the Lie group, in order to define a derivative (Lie derivative). Notice that this definition does not imply that the continuous transformations we are using should be symmetry transformations: the concepts of group orbits and generators are valid for any continuous group of transformations, not just for symmetry groups.

In the case of scalar quantities, the Lie derivative along the vector $\boldsymbol{\xi}$ reduces to the directional derivative. For instance, the first two equations in (1.43) can be written in a generic coordinate system as

$$\mathcal{L}_{\boldsymbol{\xi}}\, \tau \equiv \xi^\mu \partial_\mu \tau = 0 \,, \qquad \mathcal{L}_{\boldsymbol{\xi}}\, p = 0 \,. \tag{1.45}$$

In the case of vector quantities, like in the last equation in (1.43), an extra term appears, namely

$$\mathcal{L}_{\boldsymbol{\xi}}\, u^\mu \equiv \xi^\rho \partial_\rho u^\mu - u^\rho \partial_\rho \xi^\mu = 0 \,. \tag{1.46}$$

Notice that one could replace partial derivatives by covariant ones in (1.46) without altering the result: this is a tensor expression, valid in a general coordinate system. The same can be done with the original equation (1.41), namely

$$\mathcal{L}_{\boldsymbol{\xi}}\, g_{\mu\nu} \equiv \xi^\rho \partial_\rho g_{\mu\nu} + g_{\mu\rho}\, \partial_\nu \xi^\rho + g_{\rho\nu}\, \partial_\mu \xi^\rho = 0 \,, \tag{1.47}$$

where a correction term appears for every index, following the pattern of covariant derivatives, but with the opposite sign. As a consequence, the expression (1.47) gets a simpler form

$$\mathcal{L}_{\boldsymbol{\xi}}\, g_{\mu\nu} \equiv \nabla_\mu \xi_\nu + \nabla_\nu \xi_\mu = 0 \,, \tag{1.48}$$

which is known as the Killing equation. Any solution $\boldsymbol{\xi}$ of the Killing equation is known as a Killing vector field and can be interpreted as the generator of a one-parameter group of isometry transformations (symmetries).

Remember that for a general coordinate transformation the metric coefficients transform in the covariant way (1.3). Isometry transformations are the particular cases such that the final coefficients happen to be identical to the original ones, revealing some symmetry of spacetime. Tensors transform in a covariant way under any change of coordinates, but they are invariant only under isometry transformations. In the case of the curvature tensor, for instance, this fact translates into the generic coordinate system version of (1.42), namely

$$\mathcal{L}_{\boldsymbol{\xi}}\, R^{\mu}{}_{\nu\rho\sigma} = 0 \,, \tag{1.49}$$

which must hold for every Killing vector $\boldsymbol{\xi}$.

1.3.2 Exact Solutions

Symmetry considerations are of great help in order to find exact solutions of Einstein's field equations (1.26). Although hundreds of particular solutions have been found (see [1] for an excellent compendium), and are still being found today, only those with a high degree of symmetry are being widely used to build astrophysical or cosmological models.

Let us consider for instance the standard cosmological models. A six-parameter symmetry group is assumed, so that the orbit of any given spacetime point P is a spatial hyper-surface. The six-dimensional symmetry group can be described as consisting of a three-dimensional subgroup of rotations (which will leave the origin point O invariant), plus three more independent generators mapping the origin O into any other point of the same hyper-surface. From the physical point of view, we can just say that spacetime is spatially homogeneous and isotropic (Cosmological Principle).

As far as this is the maximum degree of symmetry for a three-dimensional manifold, it follows from a classical theorem that the spatial hyper-surfaces must be of constant curvature. One can also align the time axis with the normal vectors to these space hyper-surfaces. Putting together all these results, it follows that the line element with such maximum degree of spatial symmetry can be written as,

$$-\,dt^2 + R(t)^2 \left(\frac{dr^2}{\sqrt{1-k\,r^2}} + r^2\, d\Omega^2 \right) \tag{1.50}$$

(Friedman-Robertson-Walker metrics, FRW in what follows), where $R(t)$ is an arbitrary function and the parameter k can be

$$k = +1 \,,\; -1 \,,\; 0 \,, \tag{1.51}$$

corresponding respectively to positive, negative or zero curvature of the space hyper-surfaces. As commented in the former subsection, all the quantities obtained from the metric without further input must share its symmetries. This means that the stress-energy tensor of the FRW metrics corresponds to an ideal fluid (1.21) with uniform energy density and pressure distribution

$$\tau = \tau(t) \qquad p = p\,(t)\ . \tag{1.52}$$

The particular expressions for both the energy density τ and the pressure p will depend of course of the specific expression for the 'cosmological radius' $R(t)$ that is being used.

Another widely used solution, the Schwarzschild line element, describes an static and spherically symmetric spacetime. From the group-theoretical point of view, it can be obtained by imposing a four-dimensional group of symmetries. One of the group generators is supposed to describe time translations, so that we can use an adapted time coordinate in which all metric components are time-independent. Also, as in the previous case, the group contains a three-dimensional subgroup of rotations around an origin point O, so that any given point P is mapped into any other point belonging to the same spherical surface with center at O.

The use of the term 'spherical surface' here is fully justified because a three-parameter subgroup is the maximum degree of symmetry for a two-dimensional surface. These surfaces must be then of constant curvature, which is assumed to be positive in the spherical case. One can even define the Schwarzschild radial coordinate r so that the area S of such spherical surfaces is precisely

$$S = 4\pi r^2\ . \tag{1.53}$$

The corresponding vacuum metric is then given by

$$-\,(1-2M/r)\,dt^2 + \frac{dr^2}{1-2M/r} + r^2\,d\Omega^2\ , \tag{1.54}$$

where M is an arbitrary parameter (Schwarzschild mass). The Schwarzschild metric (1.54) can be used to describe spacetime in the vicinity of an isolated spherical body of mass M.

Let us remember at this point that we are talking here about local solutions. Schwarzschild spacetime, for instance can not be properly described as static inside the 'horizon surface' at

$$r = 2M\ . \tag{1.55}$$

(Schwarzschild radius). The lines labelled by the t coordinate can no longer be interpreted as time lines due to the change of sign of the corresponding coefficient in (1.54). However, one can always build up a composite metric by matching a suitable interior (non-vacuum) metric to the exterior region of (1.54), outside the Schwarzschild radius. The interior metric itself needs not

be static: one could even use a FRW metric corresponding to pressureless fluid (dust) to model the spherical collapse of an isolated dust ball (Oppenheimer-Schneider collapse).

The same idea works backwards: one can consider the Schwarzschild metric (1.54) as describing an spherical void in an expanding FRW dust universe. As far as the FRW metrics are homogeneous, one can get an arbitrary distribution of non-overlapping voids in this way. This is known as the Einstein-Strauss 'Swiss cheese' model, in which the static local metrics are compatible with the overall cosmological evolution.

1.3.3 Analytical and Numerical Approximations

Symmetry considerations can be of great help for building exact models of simple configurations. These simplified models can even serve as a guide for describing systems departing from the given symmetry by some amount: one can consider these symmetry deviations as a perturbation of the exact model. But more complex configurations, like the ones commonly encountered in Astrophysics, with a lot of details to be accounted for, can be very far from any symmetry, so that perturbations around a symmetric background could not be used in a consistent way. This is why one can consider using some other approximation scheme in order to handle with such more realistic models up to the required accuracy level.

The weak field approximation scheme consists in replacing the exact line element by some perturbation series starting with the Minkowski metric of Special Relativity. The adimensional quotient M/R is used as the perturbation parameter, where M is the typical mass of the objects considered and R the typical distance of the configuration. This approach works fine in astrophysical scenarios involving ordinary stars, like our Sun, where

$$M = 1.47\,\mathrm{km}\,, \qquad R = 7\;10^5\,\mathrm{km}\,, \tag{1.56}$$

and even in the vicinity of a neutron star ($R = 10\,\mathrm{km}$ for the same mass). It can also be combined with the slow motion approximation scheme, where V/c is the adimensional parameter, V being the typical speed of the problem.

But all these schemes fail in the most extreme scenarios, where one has both strong fields and high speeds: Supernova explosions, matter accretion into a Black Hole or the late stages of a binary system, when the two orbiting bodies merge into a single compact object. These are not just curiosities that can be left aside from our research agenda. On the contrary, these astrophysical configurations are very good candidates as gravitational wave sources. This is because the effects on Earth of gravitational waves coming from deep space are so tiny that one needs something really dramatic at the source (strong fields evolving really fast) in order to have a chance, even a small one, for detecting it. You can see [2] and [3] for an overview of the current interferometer and resonant (bar or sphere) detection facilities, respectively.

This is where Numerical Relativity comes into play. Numerical approximations do not rely on the smallness of physical parameters, that could prevent to apply it to some otherwise interesting physical situations. The approximation here consists on the discretization of the continuous set of arbitrary functions. Any function f is replaced by a finite set of values

$$f(t) \;\rightarrow\; \{f^{(n)}\} \quad (n = 1, \ldots, N) \; . \tag{1.57}$$

The term discretization comes precisely from the fact that the continuous set of values of f is replaced by a discrete (and finite) set of N numbers. The adimensional parameter related to the order of the numerical approximation is just $1/N$, independently of the physics of the problem. This is why one can apply numerical approximations to any physical situations, without having to restrict oneself to any particular dynamical regime.

The discrete set of values $\{f^{(n)}\}$ can be constructed in different ways, depending on the particular numerical approach which is being used:

- In the **Spectral Methods** approach, the values $f^{(n)}$ correspond to the coefficients of the development of the function f in a series of some specific set of basis functions $\{\phi^{(n)}\}$, namely

$$f = \sum_{1}^{N} f^{(n)} \phi^{(n)} \; . \tag{1.58}$$

- In the **Finite Elements** approach, the values $f^{(n)}$ correspond rather to the integrals of the function f over a set of finite domains with volume V_n, namely

$$f^{(n)} = \int_{V_n} f \; dV \; . \tag{1.59}$$

  Notice that it can be formally consider as a particular case of the spectral methods approach by choosing the basis functions $\phi^{(n)}$ to be zero outside the corresponding volume V_n.
- In the **Finite Difference** approach, the continuous spacetime itself is replaced by a lattice of points (numerical grid). The values $f^{(n)}$ are just the values of the function f for this discrete set of grid points. In the case of the time dependence, for instance, one has

$$f^{(n)}(t) = f(t_n) \; . \tag{1.60}$$

  This can be formally interpreted as the limit case of the Finite Elements approach when the volumes V_n tend to zero, so that the set of (normalized) basis functions $\{\phi^{(n)}\}$ tends to a set of Dirac delta functions.

Although all these approaches are currently used to deal with the space variables, time evolution in Numerical Relativity is usually dealt with finite differences (1.60). This can be interpreted as describing spacetime by a series of snapshots, step by step, like in a movie film. In the following section, we will see how to reformulate the field equations in order to keep with this description.

2

The Evolution Formalism

2.1 Space Plus Time Decomposition

The general covariant approach to General Relativity is not adapted to our experience from everyday life . The most intuitive concept is not that of spacetime geometry, but rather that of a time succession of space geometries. This 'flowing geometries' picture could be easily put into the computer, by discretizing the time coordinate, in the same way that the continuous time flow of the real life is coded in terms of a discrete set of photograms in a movie.

In this sense, we can say that General Relativity theory, when compared with other physical theories like electromagnetism, has been built upside down. In Maxwell theory one starts with the everyday concepts of electric charges, currents, electric and magnetic fields. One can then write down a (quite involved) set of field equations, Maxwell equations, that can be easily interpreted by any observer. Only later some 'hidden symmetry' (Lorentz invariance) of the solution space is recognized, and this allows to rewrite Maxwell equations in a Lorentz-covariant form. But the price to pay is gluing charges and currents on one side, and electric and magnetic fields on the other, into new four-dimensional objects that obscure the direct relation to experience of the original (three-dimensional) components.

In General Relativity, we have started from the top, so that we must go downhill, in the opposite sense:

- By selecting an specific (but generic) time coordinate.
- By decomposing every four-dimensional object (metric, Ricci and stress-energy tensors) into more intuitive three-dimensional components.
- By writing down the (much more complicated) field equations that translate the manifestly covariant ones (1.31) in terms of these three-dimensional pieces.

General covariance will then become a hidden feature of the resulting '3+1 equations'. The equations themselves will no longer be covariant under

C. Bona and C. Palenzuela Luque: *Elements of Numerical Relativity*, Lect. Notes Phys. **673**, 19–39 (2005)
www.springerlink.com

a general coordinate transformation. But, as far as the solution space will be the same as before making the decomposition, general coordinate transformations will still map solutions into solutions (as it happens with Lorentz transformations in Maxwell equations). The underlying invariance of the equations under general coordinate transformations is then preserved when performing the 3+1 decomposition. General covariant four-dimensional equations just show up this invariance in an explicit way.

2.1.1 A Prelude: Maxwell Equations

Maxwell equations are usually written as

$$\nabla \cdot \boldsymbol{E} = 4\pi\rho \tag{2.1}$$

$$\nabla \cdot \boldsymbol{H} = 0 \tag{2.2}$$

$$-\partial_t \boldsymbol{E} + \nabla \times \boldsymbol{H} = 4\pi \boldsymbol{j} \tag{2.3}$$

$$\partial_t \boldsymbol{H} + \nabla \times \boldsymbol{E} = 0 \tag{2.4}$$

where it is clear that the charge and current densities, ρ and $\boldsymbol{j}$, act as the sources of the electric and magnetic fields, $\boldsymbol{E}$ and $\boldsymbol{H}$.

The second pair of equations (2.3, 2.4) can be interpreted as providing a complete set of time evolution equations for the electric and magnetic fields (evolution system), whereas the first two equations (2.1, 2.2) do not contain time derivatives and can be interpreted then as constraints. These constraints are first integrals of the evolution system if we allow for the charge continuity equation, namely

$$\partial_t \rho + \nabla \cdot \boldsymbol{j} = 0 \,. \tag{2.5}$$

Now, we can start joining pieces. The charge and current densities can be combined to form a four-vector J^μ,

$$J^\mu \equiv (\rho, \boldsymbol{j}) \,. \tag{2.6}$$

The electric and magnetic fields can be combined in turn to form an antisymmetric tensor, namely

$$F_{\mu\nu} \equiv \begin{pmatrix} 0 & -E_j \\ E_i & F_{ij} \end{pmatrix} \,, \qquad F_{ij} \equiv \epsilon_{ijk} H^k \tag{2.7}$$

(electromagnetic field tensor)

The pair (2.1, 2.3) of Maxwell equations can then be written in the manifestly covariant form

$$\nabla_\nu F^{\mu\nu} = 4\pi J^\mu \,, \tag{2.8}$$

whereas the other pair (2.2, 2.4) can be written as

$$\nabla_\rho F_{\mu\nu} + \nabla_\mu F_{\nu\rho} + \nabla_\nu F_{\rho\mu} = 0 \,. \tag{2.9}$$

Notice that, allowing for the antisymmetry of the electromagnetic tensor, the four-divergence of (2.8) leads immediately to the covariant version of the charge continuity equation (2.5), namely

$$\nabla_\mu J^\mu = 0 \, . \tag{2.10}$$

This strongly reminds the General Relativity situation, where Einstein's equations (1.31), allowing for the Bianchi identities (1.19), lead to the conservation of the stress-energy tensor.

2.1.2 Spacetime Synchronization

Coming back to the General Relativity case, the 3+1 spacetime decomposition is based on two main geometrical elements:

- The first one is the choice of a **synchronization**. This amounts to foliate spacetime by a family of spacelike hypersurfaces, so that any spacetime point belongs to one (and only one) slice. This geometrical construction can be easily achieved by selecting a regular spacetime function

$$\phi(x^\mu) \tag{2.11}$$

  such that the level hypersurfaces of ϕ (defined by $\phi = const$) provide the desired foliation. In order to consider ϕ as a local time coordinate, we must make sure that the resulting slicing is spacelike, namely

$$g^{\mu\nu} \partial_\mu \phi \, \partial_\nu \phi < 0 \, . \tag{2.12}$$

  Every single slice can be considered as a three-dimensional manifold. It is clear that curves on this manifold are also spacetime curves and therefore the spacetime metric can be directly used for measuring lengths on any three-dimensional slice. In that way, the three-dimensional metric γ_{ij} on every slice is induced by the spacetime metric $g_{\mu\nu}$. The overall picture can be easily understood by fully identifying the function ϕ with our time coordinate, that is

$$\phi(x^\mu) \equiv t \, , \qquad \partial_\mu \phi = \delta_\mu^{\ 0} \, , \tag{2.13}$$

  so that the three-dimensional line element

$$dl^2 = \gamma_{ij} \, dx^i dx^k \qquad (i, \, j = 1, 2, 3) \tag{2.14}$$

  can be obtained from the four-dimensional one by restricting it to the constant time surfaces, namely

$$\gamma_{ij} = g_{ij} \, . \tag{2.15}$$

- The second ingredient is the choice of a **congruence of time lines**. The simplest way is to get it as the integral curves of the system

$$\frac{dx^\mu}{d\lambda} = \xi^\mu \ , \tag{2.16}$$

so that the congruence is fully determined by the choice of the field of tangent vectors ξ^μ. The affine parameter λ in (2.16) can be chosen to match the spacetime synchronization by imposing

$$\xi^\mu \partial_\mu \phi = 1 \ . \tag{2.17}$$

Notice that (2.17) is a very mild condition. It just requires that the time lines are not tangent to the constant time slices. It does not even demand the time lines to be timelike, in contrast with the stronger requirement (2.12) for the time slices (see Fig. 2.1).

Again, the meaning of (2.17) is more transparent if we use ϕ as the local time coordinate, that is (2.13),

$$\xi^\mu = \delta_0^{\ \mu} \ , \tag{2.18}$$

so that the time lines equation (2.16) can be trivially integrated

$$x^0 = t \ , \qquad x^i = constant \tag{2.19}$$

We will focus first in the analysis of the time slicing. To do this, we will use normal coordinates, so that the time lines are chosen to be normal to the constant time slices. In this way we refrain from using the three extra degrees of freedom that would allow us to freely choose the tangent vector field ξ. Here we will not use any other ingredient that the slicing itself: we restrict ourselves then to the trivial choice

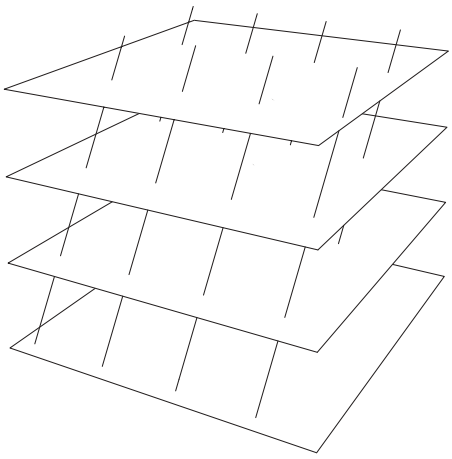

Fig. 2.1. The time slicing and the congruence of time lines. Time lines are not necessarily timelike, but they can not be tangent to the spacelike slices: they must 'thread' them. Notice that the slicing provides a natural choice of the affine parameter along the time lines

$$\xi_\mu \sim \partial_\mu \phi \ , \tag{2.20}$$

or, in local adapted coordinates (2.13),

$$g_{0i} = 0 \tag{2.21}$$

(normal coordinates). The line element can then be written, allowing for (2.15, 2.21) as

$$ds^2 = -\alpha^2 dt^2 + \gamma_{ij}\ dx^i dx^j \ , \tag{2.22}$$

where the factor α relates the coordinate time t with the proper time τ

$$d\tau = \alpha\ dt \ . \tag{2.23}$$

It follows that the factor α (lapse function) gives us the rate at which proper time is elapsed along the normal lines (the time lines in normal coordinates). Notice that the lapse function can take different values at different spacetime points. This means that the amount of proper time elapsed when going from one slice to another can depend on the location. On the contrary, the amount of elapsed coordinate time is, by construction, independent of the space location (see Fig. 2.2). The particular case in which the lapse function α is constant corresponds to the geodesic slicing (the name will be justified in the next subsection). The combination of geodesic slicing plus normal space coordinates is known as the Gauss coordinate system.

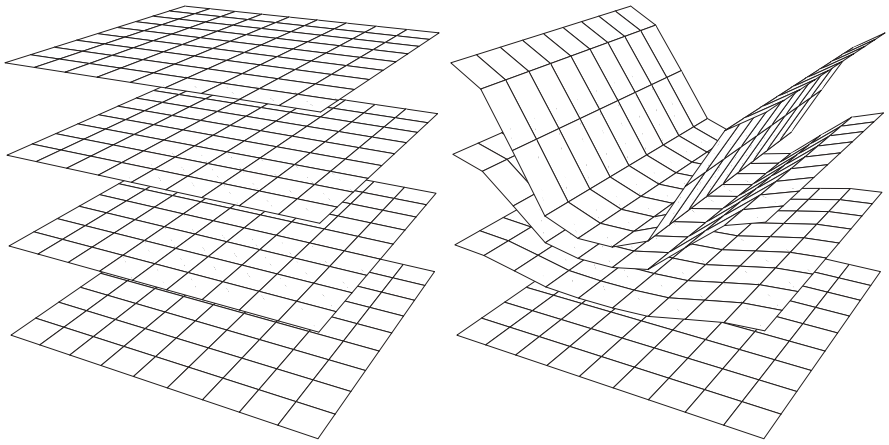

Fig. 2.2. The same time slicing is plotted by using either the local coordinate time (*left*) or the proper time (*right*) as the vertical coordinate. We have chosen a particular lapse function α such that proper time evolution slows down in the central region, while keeping a uniform rate elsewhere. This lapse-related degree of freedom will be of great help in numerical simulations of gravitational collapse, where we will like to freeze proper time evolution in the regions where a collapse singularity is going to be formed (singularity avoidance). This local proper time freezing does not affect the coordinate time evolution, represented in the left-hand-side plot, so numerical simulations can keep running

2.1.3 The Eulerian Observers

As stated before, in normal coordinates the congruence of time lines is provided by the slicing itself. We can view this congruence as the world lines of a field of observers which are at rest with respect to the spacetime synchronization (Eulerian observers). Their four-velocity field u^μ coincides, up to a sign, with the field of unit normals n^μ to the slices

$$n_\mu = \alpha\, \partial_\mu \phi \,, \qquad g^{\mu\nu} n_\mu n_\nu = -1 \,. \tag{2.24}$$

The relative sign comes from the normalization condition (2.17), that is

$$u^\mu = -n^\mu \,, \qquad u^\mu n_\mu = 1 \,. \tag{2.25}$$

In normal adapted coordinates, we have

$$u^\mu = \frac{1}{\alpha}\, \delta^\mu_{\ 0} \,, \qquad n_\mu = \alpha\, \delta_\mu^{\ 0} \,, \tag{2.26}$$

so that the tangent vector field u points forward in time.

The motion of any set of observers, represented by a congruence of time lines, can be decomposed into different kinematical pieces as follows

$$\nabla_\mu u_\nu = -u_\mu \dot{u}_\nu + \omega_{\mu\nu} + \chi_{\mu\nu} \,, \tag{2.27}$$

where every piece describes a different feature of the motion:

- **Acceleration**, described by the four-vector

$$\dot{u}_\mu \equiv u^\rho \nabla_\rho u_\mu \,. \tag{2.28}$$

  It is the only non-trivial projection of (2.27) along u^μ.
- **Vorticity**, described by the antisymmetric tensor $\omega_{\mu\nu}$. It is the antisymmetric part of the projection of (2.27) orthogonal to u^μ ($\omega_{\mu\nu} u^\nu = 0$).
- **Deformation**, described by the symmetric tensor $\chi_{\mu\nu}$. It is the symmetric part of the projection of (2.27) orthogonal to u^μ ($\chi_{\mu\nu} u^\nu = 0$). It can be further decomposed into its trace, the expansion scalar

$$\theta \equiv tr(\chi) \,, \tag{2.29}$$

  and its traceless part, the shear tensor

$$\sigma_{\mu\nu} = \chi_{\mu\nu} - \frac{\theta}{3} \left(g_{\mu\nu} + u_\mu u_\nu\right) \,. \tag{2.30}$$

In the case of the Eulerian observers, there is no vorticity because, by construction, they are orthogonal to the constant-time hypersurfaces. Their motion is then characterized only by the acceleration vector and the deformation tensor. In adapted normal coordinates, allowing for (2.22), the acceleration vector is given by

$$\dot{u}_\mu = (0,\, \partial_i\, ln\alpha)\ , \tag{2.31}$$

so that the choice of a constant lapse corresponds to the inertial motion (free fall) of the Eulerian observers (this justifies the term 'geodesic slicing' we used in the previous subsection for the $\alpha = constant$ case).

The deformation tensor of the Eulerian observers consists also on space components only when written in adapted normal coordinates, namely,

$$\chi_{\mu\nu} = \begin{pmatrix} 0 & 0 \\ 0 & -K_{ij} \end{pmatrix}\ . \tag{2.32}$$

The three-dimensional symmetric tensor K_{ij} in (2.32) is known as the extrinsic curvature of the slicing, whereas the minus sign in (2.32) arises from the sign convention (2.25).

The extrinsic curvature can be easily computed from (2.27). In normal adapted coordinates (2.26), we have

$$K_{ij} = -\frac{1}{2\alpha}\, \partial_t\, \gamma_{ij}\ . \tag{2.33}$$

Notice that K_{ij} admits then a double interpretation:

- From the time lines point of view, it provides the deformation $\chi_{\mu\nu}$ of the congruence of normal lines, as it follows from (2.27, 2.32).
- From the slices point of view, it provides, up to a one half factor, the Lie derivative of the induced metric γ_{ij} along the field of unit normals n^μ, as it follows from (2.25, 2.27), and the space components of the four-dimensional identity

$$\mathcal{L}_n(g_{\mu\nu}) = \nabla_\mu n_\nu + \nabla_\nu n_\mu\ . \tag{2.34}$$

Of course, these two points of view are equivalent, because the congruence of normal lines can be obtained from the slicing in a one-to-one way.

2.2 Einstein's Equations Decomposition

2.2.1 The 3+1 Form of the Field Equations

Let us summarize the results of the previous section:

- We have decomposed the four-dimensional line element into the 3+1 normal form (2.22), where the distinct geometrical meaning of the lapse function α and the induced metric γ_{ij} has been pointed out. This is analogous to decompose the electromagnetic tensor into its electric and magnetic field components.
- Einstein's field equations, contrary to Maxwell ones, are of second order. This means that one needs also to decompose the first derivatives of the four-dimensional metric. We have started doing so in the previous subsection, where we have identified the pieces describing either the acceleration

or the deformation tensor of the Eulerian observers (the lapse gradient and the extrinsic curvature K_{ij} of the slices). The remaining first derivatives can be easily computed in terms of the pieces we have got (see Table 2.1, where the full set of connection coefficients is displayed).

Table 2.1. The 3+1 decomposition of the four-dimensional connection coefficients. Notice that the symbol $\widehat{\Gamma}^{\mu}_{\rho\sigma}$ stands for the connection coefficients of the four-dimensional metric, whereas in what follows we will note as Γ^{k}_{ij} the connection coefficients of the induced three-dimensional metric γ_{ij}

$\widehat{\Gamma}^{0}_{00} = \partial_t \, ln(\alpha)$	$\widehat{\Gamma}^{k}_{00} = \alpha \gamma^{kj} \partial_j \, \alpha$
$\widehat{\Gamma}^{0}_{i0} = \partial_i \, ln(\alpha)$	$\widehat{\Gamma}^{k}_{i0} = -\alpha \gamma^{kj} K_{ij}$
$\widehat{\Gamma}^{0}_{ij} = -1/\alpha \, K_{ij}$	$\widehat{\Gamma}^{k}_{ij} = \Gamma^{k}_{ij}$

We have then for the moment a complete decomposition of the 'left-hand-side' of the field equations. The corresponding decomposition of the source terms is just the well known decomposition of the four-dimensional stress-energy tensor $T_{\mu\nu}$ into parts which are either longitudinal (aligned with n_μ), transverse (orthogonal to n_μ) or of a mixed type, namely:

- The **energy density**

$$\tau \equiv 8\pi \, T^{\mu\nu} n_\mu n_\nu \tag{2.35}$$

- The **momentum density**

$$S_i \equiv 8\pi \, T^{\mu}_{i} n_\mu \tag{2.36}$$

- The **stress tensor**

$$S_{ij} \equiv 8\pi \, T_{ij} \ , \tag{2.37}$$

which names arise from the physical interpretation that can be made from the point of view of the Eulerian observers (the 8π factors are included here for further convenience).

Now we are in position to translate the four-dimensional field equations (1.31) in terms of the 3+1 quantities. We will reproduce here for clarity the original equations in terms of the four-dimensional connection coefficients, so that we can apply the results of Table 2.1 in an straightforward way:

$$\partial_\rho \widehat{\Gamma}^{\rho}_{\mu\nu} - \partial_\mu \widehat{\Gamma}^{\rho}_{\rho\nu} + \widehat{\Gamma}^{\rho}_{\rho\lambda} \widehat{\Gamma}^{\lambda}_{\mu\nu} - \widehat{\Gamma}^{\rho}_{\lambda\mu} \widehat{\Gamma}^{\lambda}_{\rho\nu} = 8\pi \left(T_{\mu\nu} - \frac{1}{2} \, T^{\lambda}_{\lambda} \, g_{\mu\nu} \right) \ . \tag{2.38}$$

The space components of (2.38) can then be written, after some algebra, as

$$\frac{1}{\alpha} \, \partial_t K_{ij} = -\frac{1}{\alpha} \, \nabla_i \alpha_j + R_{ij} - 2K^2_{ij} + trK \ K_{ij} - S_{ij} + \frac{1}{2} \, (trS - \tau) \, \gamma_{ij} \ , \tag{2.39}$$

where the covariant derivatives and the Ricci tensor on the right-hand-side are the ones obtained by considering every slice as a single three-dimensional surface with metric γ_{ij} (traces are taken with the inverse matrix γ^{ij}). The same can be done with the mixed $(0i)$ components, namely

$$0 = \nabla_j \left(K_i{}^j - trK \, \delta_i{}^j \right) - S_i \ , \tag{2.40}$$

where we get a first surprise: no time derivative appears on the left-hand-side.

The remaining component of (2.38), the (00) one, leads in turn to

$$\frac{1}{\alpha} \, \partial_t \, trK = -\frac{1}{\alpha} \, \triangle \alpha + tr(K^2) + \frac{1}{2} \left(trS + \tau \right) . \tag{2.41}$$

This is also surprising, because the time derivative of the trace of K_{ij} can be obtained also from the space components equation (2.39). If we do so, we get by substituting the result into (2.41),

$$0 = tr \ R + (tr \ K)^2 - tr(K^2) - 2\tau \ , \tag{2.42}$$

where again no time derivative appears, like in (2.40).

2.2.2 3+1 Covariance

General covariance is lost when decomposing the four-dimensional field equations (2.38) into their 3+1 pieces (2.39, 2.40, 2.42). As far as the solution space has not been changed in the process, general coordinate transformations still map solutions into solutions: the underlying invariance of the theory is intact. The four-dimensional, general covariant, version (2.38) just makes this underlying invariance manifest.

This does not mean, however, that covariance is completely lost. A closer look to the right-hand-side terms of the 3+1 system (2.39–2.42) shows that they are actually covariant under general space coordinate transformations

$$y^i = F^i(x^j, t) \ , \tag{2.43}$$

which preserve the geometry of every single slice. They are also unchanged under an arbitrary time coordinate rescaling

$$t' = G(t) \ , \tag{2.44}$$

which affects just the labelling of the slices, but not the slicing itself. We will call in what follows '3+1 covariance' the covariance under the restricted set of slicing-preserving coordinate transformations (2.43, 2.44).

The 3+1 covariance of the right-hand sides of the system (2.39–2.42) follows from the fact that they are composed of two kinds of geometrical objects:

- three-dimensional tensors, like the metric γ_{ij} or the Ricci tensor R_{ij}, which are intrinsically defined by the geometry of the slices, when considered as individual manifolds

- pieces which can be obtained from four-dimensional tensors by using the field of unit normals n_μ, which is intrinsically given by the slicing. This is the case of the three-acceleration $\partial_i \, ln\alpha$, the deformation (extrinsic curvature) K_{ij}, and the different projections of the stress-energy tensor.

This means that, in spite of the fact that we have used normal coordinates in their derivation, equations (2.40) and (2.42) keep true in a generic coordinate system. Before getting a similar conclusion about the tensor equation (2.39), which contains a time derivative, let us consider the case of the simpler scalar equation (2.41). We know from the previous considerations that the right-hand-side term will behave as a 3+1 scalar. We will consider now the transformation properties of the time derivative in left-hand-side step by step:

- It transforms under (2.43) as

$$\left(\frac{\partial \, trK}{\partial \, t}\right)_{x=const} = \left(\frac{\partial \, trK}{\partial \, t}\right)_{y=const} - \beta^k \, \left(\frac{\partial \, trK}{\partial \, y^k}\right)_{t=const} \tag{2.45}$$

  where we have introduced the shift β^k:

$$\beta^k(y,t) \equiv \left(\frac{\partial \, y^k}{\partial \, x^r}\right) \left(\frac{\partial \, x^r}{\partial \, t}\right)_{y=const} . \tag{2.46}$$

- Concerning the time rescaling (2.44), let us notice that the lapse function is not a 3+1 scalar. It follows from its very definition (2.22) that it will transform instead as

$$\alpha' = \alpha \, \left(\frac{\partial \, t}{\partial \, t'}\right) \, , \tag{2.47}$$

  so that the combination

$$\frac{1}{\alpha} \, \partial_t \tag{2.48}$$

  is preserved. Notice that the rescaling factor in (2.47) is independent of the space coordinates, so that the three-acceleration $\partial_i \, ln\alpha$ transforms as a 3+1 vector, as expected.

Putting these results together, it follows that the generic form of equation (2.41) can be obtained from their expression in normal coordinates by the following replacement

$$\frac{1}{\alpha} \, \partial_t \, trK \quad \rightarrow \quad \frac{1}{\alpha} \, (\partial_t - \beta^k \partial_k) \, trK \, . \tag{2.49}$$

The 3+1 covariance of the resulting expression is clear if we notice that it has the intrinsic meaning of 'taking the proper time derivative of trK along the normal lines', no matter what is our coordinate system. The same idea can lead to the corresponding generalization of the tensor equation (2.39), or any other of the same kind, by using as a rule of thumb the generic replacement

$$\frac{1}{\alpha} \, \partial_t \quad \rightarrow \quad \frac{1}{\alpha} \, (\partial_t - \mathcal{L}_\beta) \, . \tag{2.50}$$

2.2.3 Generic Space Coordinates

It follows from the previous considerations that the full set of Einstein's field equations can be decomposed in a generic coordinate system as follows:

$$\frac{1}{\alpha}\,(\partial_t - \mathcal{L}_\beta)\,\gamma_{ij} = -2K_{ij} \tag{2.51}$$

$$\frac{1}{\alpha}\,(\partial_t - \mathcal{L}_\beta)\,K_{ij} = -\frac{1}{\alpha}\,\nabla_i\,\alpha_j + R_{ij} - 2K_{ij}^2 + trK\;K_{ij} - S_{ij} + \frac{1}{2}\,(trS - \tau)\,\gamma_{ij} \tag{2.52}$$

$$0 = \nabla_j\,(K_i{}^j - trK\;\delta_i{}^j) - S_i \tag{2.53}$$

$$0 = tr\,R + (tr\,K)^2 - tr(K^2) - 2\tau\;. \tag{2.54}$$

A simpler version, in Gauss coordinates, was obtained by Lichnerowicz [4]. It was extended to the general case, although in the tetrad formalism, by Choquet-Bruhat [5]. The particular version presented here is the one which became popular from the work of Arnowitt, Deser and Misner (ADM) about the Hamiltonian formalism [6], and they are often referred as ADM equations for that reason. We will refer instead to (2.51–2.54) as the 3+1 field equations, preserving the ADM label for the developments that followed.

The time-dependent space coordinates transformation (2.43), when applied to the line element (2.22), transforms it to the general form

$$ds^2 = -\alpha^2 dt^2 + \gamma_{ij}\,(dy^i + \beta^i dt)\,(dy^j + \beta^j dt)\;, \tag{2.55}$$

where it is clear that the new time lines $y = constant$ are no longer orthogonal to the constant time slices. The decomposition (2.55) is actually the most general one, where the four coordinate degrees of freedom are represented by the lapse α and the shift β^k, whereas the normal coordinates form (2.22) is recovered only in the vanishing shift case.

Using a non-zero shift is certainly a complication. For instance, the inverse matrix of the four-dimensional metric is given by

$$\hat{g}^{00} = -\frac{1}{\alpha^2}\;, \qquad \hat{g}^{0i} = \frac{1}{\alpha^2}\,\beta^i\;, \qquad \hat{g}^{ij} = \gamma^{ij} - \frac{1}{\alpha^2}\,\beta^i\,\beta^j\;, \tag{2.56}$$

and the connection coefficients contain now much more terms (see Table 2.2).

There are physical situations, however, in which a non-zero shift can be very convenient, for instance:

- When rotation is an important overall feature (spinning black holes, binary systems, etc.). If we want to adapt our time lines to rotate with the bodies, then we can not avoid vorticity and normal coordinates can no longer be used. The shift choice will be then dictated by the overall motion of our system, so that our space coordinates will rotate with the bodies (co-rotating coordinates).

- When one needs to use space-like ('tachyon') time lines. As discussed before, this is allowed provided that the constant time slices remain space-like. But one can not have both things in normal coordinates: the squared norm of the vector $\xi^\mu = \delta^\mu_0$, tangent to the time lines is given by

$$\xi \cdot \xi = -\alpha^2 + \gamma_{rs}\,\beta^r \beta^s \ , \tag{2.57}$$

so that one would need a super-luminal shift

$$|\beta| > \alpha \tag{2.58}$$

to do the job. This is mandatory if we want to move a Black Hole across the numerical domain [7]. This can be also very useful when performing numerical simulations in the vicinity of a Black Hole, if we want to prevent the horizon from growing too fast, enclosing all of our numerical grid before we have enough time to properly study the exterior region [8, 9, 10].

Table 2.2. Same as Table (2.1) for the generic coordinates case. The symbol ∇ stands here for the covariant derivative with respect to the induced metric γ_{ij}

$\widehat{\Gamma}^0_{00} = (\partial_t \alpha + \beta^k \alpha_k - K_{ij}\beta^i \beta^j)/\alpha$	$\widehat{\Gamma}^0_{i0} = (\partial_i\, \alpha - K_{ij}\beta^j)/\alpha$
$\widehat{\Gamma}^k_{00} = \gamma^{kj}[\partial_t \beta_j + \alpha\, \alpha_j - 1/2\, \partial_j(\gamma_{rs}\beta^r \beta^s)] - \beta^k \widehat{\Gamma}^0_{00}$	$\widehat{\Gamma}^k_{ij} = \Gamma^k_{ij} - \beta^k \widehat{\Gamma}^0_{ij}$
$\widehat{\Gamma}^k_{i0} = -\alpha\, K_i{}^k + \nabla_i \beta^k - \beta^k \widehat{\Gamma}^0_{i0}$	$\widehat{\Gamma}^0_{ij} = -1/\alpha\, K_{ij}$

2.3 The Evolution System

2.3.1 Evolution and Constraints

The 3+1 decomposition (2.51–2.54) splits Einstein's field equations into two subsets of equations of a different kind:

- **Evolution equations**. These govern the time evolution of the basic dynamical fields $\{\gamma_{ij}\ ,\ K_{ij}\}$, that is (2.51) and:

$$(\partial_t - \mathcal{L}_\beta)\ K_{ij} = -\nabla_i\, \alpha_j + \alpha \left[R_{ij} - 2K^2_{ij} + trK\ K_{ij} \right.$$
$$\left. - S_{ij} + \frac{1}{2}\,(trS - \tau)\ \gamma_{ij} \right] , \tag{2.59}$$

where, as stated before, no evolution equation is provided for any of the kinematical (coordinate gauge) fields $\{\alpha\ ,\ \beta^i\}$.

- **Energy and Momentum constraints**. These are constraints on the extrinsic curvature components K_{ij} and their space derivatives:

$$\mathcal{E} \equiv \frac{1}{2}\,[\,tr\,R + (tr\,K)^2 - tr(K^2)\,] - \tau = 0 \tag{2.60}$$

$$\mathcal{M}_i \equiv \nabla_j\,(K_i{}^j - trK\;\delta_i{}^j) - S_i = 0\;. \tag{2.61}$$

  The names of energy and momentum correspond to the matter terms appearing in each equation.

Notice that we can always re-combine the equations, leading to different partitions of the full system. The constraint subset (2.60, 2.61), however, can be univocally characterized as the one in which no time derivative of K_{ij} appears. This is not the case of the evolution subset: the one we have got with (2.59) will be called the Ricci evolution system, because it corresponds to the space components of the four-dimensional Ricci tensor, as it was obtained in (2.39). One can use the energy constraint (2.60) to cancel out the energy density τ contribution in (2.59), so that the evolution subsystem will consist now in (2.51) plus

$$\begin{aligned}(\partial_t - \mathcal{L}_\beta)\;K_{ij} = &-\nabla_i\,\alpha_j + \alpha\,[R_{ij} - 2K_{ij}^2 + trK\;K_{ij} - S_{ij}\,] \\ &-\frac{\alpha}{4}\,[\,tr\,R + (tr\,K)^2 - tr(K^2) - 2\,tr\,S\,]\,\gamma_{ij}\;.\end{aligned} \tag{2.62}$$

The subset (2.51, 2.62) will be called Einstein evolution system, because it can be obtained from the space components of the four-dimensional Einstein tensor, as it can be easily seen from the matter terms appearing there. Although the Ricci and the Einstein evolution systems are not equivalent when considered independently, the complete set formed by any of them plus the energy and momentum constraints is the same one, the individual equations being just combined in different ways. We will make use of this re-combination freedom in what follows.

2.3.2 Constraints Conservation

A first look at the 3+1 version (2.59–2.61) of the field equations shows its strong resemblance with the non-covariant form (2.1–2.4) of Maxwell equations, where there is also a subset of evolution equations (2.3–2.4) for the basic dynamical fields $\{\boldsymbol{E}, \boldsymbol{H}\}$ and a subset of constraints (2.1–2.2) on their space derivatives. The question arises whether the time derivative of the constraints, allowing for the evolution equations, would lead to new constraints. In the case of Maxwell equations, one can easily verify that this is not the case by taking the time derivatives of (2.1–2.2) and using both the evolution equations (2.3–2.4) and the charge conservation equation (2.5). This means that the constraints are first integrals of the full evolution system: they are preserved during time evolution. The four-dimensional version of Maxwell

equations (2.8, 2.9) gives us the key to understand this result: both sides are conserved. The left-hand side is conserved by the antisymmetry of the electromagnetic field tensor $F^{\mu\nu}$, whereas the conservation of the right-hand-side amounts to that of the charge-current four-vector J^{μ} (2.10).

In the case of the Einstein equations, the straightforward procedure of taking the time derivatives of the constraints (2.60–2.61) and then using the evolution equations (2.59) is impractical, even using an algebraic computing program. One can however take advantage of the lesson learned in the Maxwell case and look instead to the four-dimensional form of the field equations (1.26), where again we find that both sides are conserved. The Einstein tensor $G^{\mu\nu}$ on the left-hand side is conserved due to the contracted Bianchi identities (1.19), whereas the conservation of the right-hand-side amounts to that of the stress-energy tensor $T^{\mu\nu}$ (1.25). This is the idea that we advanced when discussing equation (1.29).

We will address here this point in a more detailed way. Let us start by deriving the 3+1 version of (1.25). The most convenient way is to follow the standard procedure, that is

- by computing it first in normal coordinates.
- by expressing the results in terms of 3+1 covariant quantities
- by using then the standard replacement (2.50) to get the general expression, valid in any coordinate system.

We give just the final result:

$$\frac{1}{\alpha}\left(\partial_t - \mathcal{L}_\beta\right)\,\tau + \nabla_j\,S^j = \tau\;trK - 2\,S^j\,\partial_j\,ln\alpha + K_{ij}\,S^{ij} \tag{2.63}$$

$$\frac{1}{\alpha}\left(\partial_t - \mathcal{L}_\beta\right)\,S_i + \nabla_j\,S_i^{\ j} = S_i\,trK - S_i^{\ j}\,\partial_j\,ln\alpha - \tau\,\partial_i\,ln\alpha\;, \tag{2.64}$$

which is the 3+1 version of the general covariant equation (1.25) (remember that all the indices are raised and lowered here with the induced metric γ_{ij}).

In the same way, we can also translate into the 3+1 language the corresponding conservation equation (1.29) for the difference between the left-hand-side and the right-hand-side of Einstein's field equations, namely

$$\frac{1}{\alpha}\left(\partial_t - \mathcal{L}_\beta\right)\,\mathcal{E} + \nabla_j\,\mathcal{M}^j = \mathcal{E}\;trK - 2\,\mathcal{M}^j\,\partial_j\,ln\alpha + K_{ij}\,\mathcal{P}^{ij} \tag{2.65}$$

$$\frac{1}{\alpha}\left(\partial_t - \mathcal{L}_\beta\right)\,\mathcal{M}_i + \nabla_j\,\mathcal{P}_i^{\ j} = \mathcal{M}_i\,trK - \mathcal{P}_i^{\ j}\,\partial_j\,ln\alpha - \mathcal{E}\,\partial_i\,ln\alpha\;, \tag{2.66}$$

where we have noted

$$\mathcal{P}_{ij} \equiv G_{ij} - 8\pi\,T_{ij}\;. \tag{2.67}$$

Now we can see how any eventual deviation from the energy and momentum constraints $\{\mathcal{E}, \mathcal{M}_i\}$ would propagate, assuming that the time evolution is given by the Einstein system (2.62):

$$\mathcal{P}_{ij} = 0 \tag{2.68}$$

$$\frac{1}{\alpha}\left(\partial_t - \mathcal{L}_\beta\right)\mathcal{E} + \nabla_j \mathcal{M}^j = \mathcal{E}\, trK - 2\,\mathcal{M}^j\,\partial_j\, ln\alpha \tag{2.69}$$

$$\frac{1}{\alpha}\left(\partial_t - \mathcal{L}_\beta\right)\mathcal{M}_i = \mathcal{M}_i\, trK - \mathcal{E}\,\partial_i\, ln\alpha\,. \tag{2.70}$$

The corresponding result for the Ricci evolution equation (2.59) can be obtained in an analogous way, by substituting the corresponding condition

$$\mathcal{P}_{ij} = \mathcal{E}\,\gamma_{ij} \tag{2.71}$$

into the full system (2.65, 2.66). Independently of the choice, the resulting expression will be a linear homogeneous system on $\{\mathcal{E}, \mathcal{M}_i\}$, so that our statement that the vanishing of such quantities provides a set of first integrals of the evolution equations holds true, as anticipated from the four-dimensional version (1.29).

2.3.3 Evolution Strategies

The structure of the 3+1 field equations (2.59–2.61) is so similar to that of the Maxwell equations (2.1–2.4), that one can get some inspiration for the equation-solving strategies in electromagnetism in order to do the same in the gravitational case. One can start by solving the constraint equations (2.60, 2.61) to compute up to four of the six dynamical degrees of freedom (represented here by the components of the extrinsic curvature K_{ij}). As far as the constraints are first integrals of the evolution system, the remaining equations (2.59) can be used later for computing the two remaining dynamical degrees of freedom.

This 'constrained evolution' approach is specially convenient in astrophysical scenarios where the general relativistic effects can be described as lower order corrections to the Newtonian Gravity ones. This is because Newtonian Gravity is completely analogous to electrostatics, in the sense that the time evolution of the fields is not provided by the equations. The constraints (2.60, 2.61) contain then all the Newtonian effects whereas genuine relativistic effects, like the field dynamics leading to gravitational waves, must be found instead in the evolution subset (2.59). One could say that the constraints contain all the dynamical degrees of freedom, apart from the two of them corresponding to gravitational radiation and the ones related with the coordinate gauge freedom, as we will justify later.

From the Numerical Relativity point of view, the constrained evolution approach, although it can be useful to deal with specific physical situations, is not very convenient for building a general purpose code. There are many reasons for this:

- Constraint equations (2.60, 2.61) are of elliptic type (exemplified by the Laplace equation). This means that particular solutions are of a non-local

nature: they depend strongly on boundary conditions and any local perturbation spreads immediately all over the numerical domain. Spectral methods are specially suited for elliptic equations: they allow to put the outer boundary very far away, even at infinity, where one can set up very reliable boundary conditions, and they usually provide smooth and accurate solutions without consuming too much computational resources.

- Evolution equations (2.59), on the contrary, are more close to the hyperbolic type (exemplified by the wave equation), in the sense that local perturbations propagate over the numerical domain with some finite characteristic speed. This allows the appearance of non-smooth perturbations, even shocks, that are very difficult to deal with using spectral methods. Either finite differences or finite elements discretization are the numerical methods of choice for hyperbolic equations.
- There is no generical way of algebraically splitting the dynamical degrees of freedom in order to single out the ones corresponding to gravitational radiation. As we will see in the next section, such an algebraic splitting can only be done if one knows in advance the gravitational waves propagation direction. This could be the case in highly symmetrical cases: the gravitational radiation degrees of freedom can be just neglected in the spherical case, so that the radial direction could be used in problems with approximate spherical symmetry. But there is no such rule for the generic case that could be used in a general-purpose numerical code.

The obvious alternative to the constrained evolution approach is to use just the six evolution equations (2.59) to compute everything. The constraints (2.60, 2.61) could be enforced just on the initial and boundary data, because they are first integrals of the evolution system and this would be enough to ensure their validity inside the computational domain. One can even use the constraints as a quality check of the calculations. This approach, named 'free evolution' [11], continues to be by far the most commonly used in Numerical Relativity codes, usually implemented with either finite differences or finite elements discretization. This approach has very deep theoretical and practical implications, which will be discussed thoroughly in the next chapter.

2.4 Gravitational Waves Degrees of Freedom

2.4.1 Linearized Field Equations

Let us come back to the full set (evolution plus constraints) of 3+1 equations (2.51–2.54). To avoid coordinate complications, we will choose Gauss coordinates, that is normal coordinates (zero shift) and Geodesic slicing (with $\alpha = 1$), that is

$$ds^2 = -dt^2 + \gamma_{ij}\, dx^i\, dx^j \ . \tag{2.72}$$

As discussed in the previous chapter, any metric can be written down at a given spacetime point P in a locally inertial coordinate system such that the

first derivatives of the metric coefficients vanish at P. Then, as we can get as close as we want to P, we can safely split the space metric in (2.72) into two components:

- An Euclidean (flat) background of the form

$$\alpha_0 = 1 \,, \qquad \gamma^0_{ij} = \delta_{ij} \,. \tag{2.73}$$

- A linear perturbation which, when superimposed to the background, allows one to recover the full metric

$$\delta\gamma_{ij} = \gamma_{ij} - \gamma^0_{ij} \,. \tag{2.74}$$

  For further convenience, we will relax here the geodesic slicing condition, allowing also for linear perturbations of the lapse function, namely

$$\delta\alpha = \alpha - \alpha_0. \tag{2.75}$$

Of course, as far as the extrinsic curvature can be obtained from the first time derivative of the space metric, one must have for consistency

$$K^0_{ij} = 0 \,, \qquad \delta K_{ij} = K_{ij} \,. \tag{2.76}$$

We can substitute the perturbations (2.74–2.76) into the 3+1 equations (2.51–2.54) for the vacuum case. We get, up to the linear order:

$$\partial_t \, (\delta\gamma_{ij}) = -2 \, (\delta K_{ij}) \tag{2.77}$$
$$\partial_t \, (\delta K_{ij}) = -\partial^2_{ij} \, (\delta\alpha) + \delta R_{ij} \tag{2.78}$$
$$0 = \delta^{rs}[\partial_r \, (\delta K_{si}) - \partial_i \, (\delta K_{rs})] \tag{2.79}$$
$$0 = tr \, (\delta R) \,, \tag{2.80}$$

where the trace is computed with the flat background metric (2.73) and the linear order expression for the Ricci tensor is given by

$$\delta R_{ij} = -\frac{1}{2} \, \delta^{rs}[\partial^2_{rs}(\delta\gamma_{ij}) + \partial^2_{ij}(\delta\gamma_{rs}) - \partial^2_{ir}(\delta\gamma_{js}) - \partial^2_{jr}(\delta\gamma_{is})] \,. \tag{2.81}$$

2.4.2 Plane-Wave Analysis

In order to fully analyze the linear system (2.77–2.80), it is convenient to Fourier-transform the local perturbation and look at the behavior of a generic plane-wave component, propagating along a given direction n_i, namely

$$\delta\alpha = e^{i\,\omega\cdot x} \, a(\omega, t) \tag{2.82}$$
$$\delta\gamma_{ij} = e^{i\,\omega\cdot x} \, h_{ij}(\omega, t) \tag{2.83}$$
$$\delta K_{ij} = e^{i\,\omega\cdot x} \, k_{ij}(\omega, t) \,, \tag{2.84}$$

where $\omega_k = \omega \, n_k$, $\delta^{\,ij} \, n_i \, n_j = 1$.

Now we can translate the partial differential equations system (2.77–2.80) into the ordinary differential equations one

$$\partial_t\ h_{ij} = -2\ k_{ij} \tag{2.85}$$
$$\partial_t\ k_{ij} = \omega^2/2\ [\, h_{ij} - n_i\, h_{nj} - n_j\, h_{ni} + (tr\, h + 2\, a)\, n_i\, n_j\,] \tag{2.86}$$
$$0 = k_{ni} - n_i\, tr\, k \tag{2.87}$$
$$0 = tr\, h - h_{nn}\ , \tag{2.88}$$

where the symbol n replacing an index means contraction with n_i. It is then useful to decompose the Fourier modes into longitudinal (aligned with the propagation direction n_i) and transverse components (tangent to the wavefronts, which are the surfaces orthogonal to n_i). One gets then three different types of modes, according to their time evolution:

- Three **static** modes, as we get from (2.87):

$$\partial_t\ (h_{ni} - n_i\, tr\, h) = -2\ (k_{ni} - n_i\, tr\, k) = 0 \tag{2.89}$$

- One **gauge** mode, which evolution is fully determined by lapse perturbations,

$$\partial_t\ tr\, h = -2\ tr\, k\ , \qquad \partial_t\ tr\, k = \omega^2\, a\ , \tag{2.90}$$

  where we have used (2.88)
- Two **wave** modes, oscillating with the Fourier frequency ω,

$$\partial_t\, h_{\perp\perp} = -2\ k_{\perp\perp}\ , \qquad \partial_t\, k_{\perp\perp} = \omega^2/2\ h_{\perp\perp}\ , \tag{2.91}$$

  where the symbol $\perp$ replacing an index means the projection orthogonal to n_i. There are only two independent modes in (2.91), because the trace part vanishes if we allow for (2.88), that is

$$tr\,(h_{\perp\perp}) = tr\ h - h_{nn} = 0\ . \tag{2.92}$$

  This static mode was yet included in (2.89).

Let us focus in the gauge mode (2.90) for a while. In the Gauss coordinate system no lapse perturbations are allowed ($a = 0$). This means that the equations allow then for a linear growth of the trace $tr\, h$ of the metric perturbation, which corresponds to the linear term of the space metric determinant, namely

$$\gamma \equiv det(\gamma_{ij}) \simeq 1 + e^{i\,\omega\cdot x}\,(tr\, h + \cdots) \tag{2.93}$$

so that the first equation in (2.90) corresponds to the evolution of the space volume element $\sqrt{\gamma}$

$$\partial_t\ \sqrt{\gamma} = -\alpha\, tr\, K \tag{2.94}$$

and the linear gauge mode corresponds then to an overall expansion (or collapse) of the space metric. This is one of the main reasons why Geodesic slicing is not suitable for numerical simulations, because discretization errors coupled

with the gauge mode can produce an artificial linear growing which is easily amplified by the non-linear terms, leading to a numerical blow up. This is why we have relaxed this condition to allow for generic gauge perturbations.

A much suitable choice in this context would be instead the Maximal slicing condition,

$$tr\, K = 0 \,, \tag{2.95}$$

which ensures that the gauge modes are also static ($\partial_t\, tr\, h = 0$). The time evolution of $tr\, K$ is given by (2.41), so that the Maximal slicing condition is preserved if and only if the lapse function verifies the consistency condition

$$\frac{1}{\alpha}\, \triangle\alpha = tr(K^2) + \frac{1}{2}\,(trS + \tau) \,, \tag{2.96}$$

which reduces to the Laplace equation, up to the linear order, in the vacuum case.

Maximal slicing has been widely used in Numerical Relativity codes [12, 13], leading to smooth and stable lapse profiles at the cost of solving the elliptic (Laplace-like) equation (2.96) at every time step. In the non-vacuum case, equation (2.96) reduces at the linear order to the Poisson-like equation

$$\triangle(\delta\alpha) = 4\pi\,\rho \,, \tag{2.97}$$

where we have considered the mass density ρ as the first order contribution to the energy density τ (this amounts to consider kinetic and pressure effects as higher order terms). This is precisely the field equation in Newtonian Gravity

$$\triangle\,\phi = 4\pi\,\rho \,, \tag{2.98}$$

which determines the gravitational potential ϕ for a given mass distribution.

It follows that the lapse perturbation $\delta\alpha$ can be identified with the gravitational potential ϕ in the Newtonian limit. This is consistent if we define the Newtonian limit by the following two conditions:

- We consider perturbations of the Minkowski background up to the linear order.
- We ignore any evolution effect (apart from the ones produced by the motion of the sources): this means neglecting gravitational waves, but also enforcing maximal slicing, as we have seen.

This explains why the maximal slicing condition (2.96) is so effective in providing smooth lapse profiles, independently of the riddles produced by time evolution in other field components.

2.4.3 Gravitational Waves and Gauge Effects

Let us summarize now some results from the previous analysis. If we use normal coordinates with maximal slicing, then, up to the linear order, the

only dynamical effects on every Fourier component are the ones described by the two transverse traceless degrees of freedom given by

$$\partial_t \; < h_{\perp\perp} >= -2 \; < k_{\perp\perp} > , \qquad \partial_t \; < k_{\perp\perp} >= \omega^2/2 \; < h_{\perp\perp} > , \tag{2.99}$$

where we have noted by $< \cdots >$ the traceless part, for instance

$$< k_{\perp\perp} > \equiv \; k_{\perp\perp} - \frac{1}{2}\, tr\,(k_{\perp\perp})\, \delta_{\perp\perp} \; . \tag{2.100}$$

Equations (2.99) imply that the dynamical behavior of the selected Fourier component can be described as the one of a plane wave propagating with the speed of light along the selected direction n_i, that is

$$\delta\, K_{ij} \sim e^{i\,\omega(n\cdot x \,\pm\, t)} \; . \tag{2.101}$$

From the physical point of view, it follows that Gravitational waves should be transverse and traceless, and should propagate with light speed. One could wonder whether the fact that gravitational radiation consists of two degrees of freedom could be anticipated by the following naive balance: six components in K_{ij} minus four constraints give precisely two 'gravitational radiation' components.

The fallacy in this argument can be easily discovered if one tries to apply it to Maxwell equations (2.1–2.4). There we have six components in the electric and magnetic fields, minus two constraints, so that four components are left. But electromagnetic radiation has only one degree of freedom. This means that there are non-radiative dynamical contributions to the electromagnetic field that contribute to the linear order. The true balance should read: six electromagnetic field components minus two constraints gives four dynamical degrees of freedom, but only one of them is of a radiative type. In Einstein's equations, instead, non-radiative dynamical effects do not show up at the linear order, where we just find gravitational radiation, aside from eventual gauge effects.

We have found one such gauge effects: the linear mode (2.90) that appears when using geodesic slicing. Another kind of gauge effect would show up when using harmonic slicing, which can be defined as

$$\Box\, t = 0 \;\longleftrightarrow\; \partial_t\, (\alpha/\sqrt{\gamma}) = 0 \; , \tag{2.102}$$

where the box symbol stands for the covariant wave operator acting on functions, namely

$$\Box\, \Phi \;\equiv\; g^{\mu\nu}(\partial^2_{\mu\nu}\Phi - \widehat{\Gamma}^{\rho}_{\mu\nu}\partial_\rho\Phi) \; . \tag{2.103}$$

The gauge perturbation $\delta\alpha$ is then dynamically related with the space volume perturbation. In Fourier space we have

$$\partial_t \; (a - tr\, h) = 0 \tag{2.104}$$

and the gauge mode (2.90) can be written as

$$\partial_t\ a = -tr\, k\ , \qquad \partial_t\ tr\, k = \omega^2\, a\ , \tag{2.105}$$

which reproduces the same propagation behavior as that of gravitational waves

$$\delta\alpha \sim e^{i\,\omega(n\cdot x \pm t)}\ . \tag{2.106}$$

These 'gauge waves' do not describe any physical effect: they are rather an artifact of the gauge choice. We have introduced the harmonic slicing here mainly for two reasons

- It provides an oscillatory gauge behavior that is between the linear one of geodesic slicing and the static one of maximal slicing. We will use a generalization of this condition it in the next chapter in order to obtain hyperbolic evolution systems with a view to numerical simulations.
- The direct relationship (2.102) between the lapse function and the space volume element can be used to avoid collapse singularities in numerical simulations of black hole spacetimes (singularity avoidance, see Fig. 2.2).

3

Free Evolution

3.1 The Free Evolution Framework

3.1.1 The ADM System

As we mentioned in the previous chapter, the 'free evolution' approach is by far the most commonly used today in Numerical Relativity codes. It consists on using just the evolution equations to compute the full set of dynamical quantities (γ_{ij}, K_{ij}) . We have seen that the subset of evolution equations is not unique: evolution equations can be modified by adding constraints in many different ways. This implies that we must distinguish among different versions of free evolution, depending on the particular variant of the evolution equations which is selected in each case. The first choice is to take just the space components of the four-dimensional Ricci tensor, namely

$$(\partial_t - \mathcal{L}_\beta)\ \gamma_{ij} = -2\alpha\, K_{ij} \tag{3.1}$$

$$(\partial_t - \mathcal{L}_\beta)\ K_{ij} = -\nabla_i\, \alpha_j + \alpha \left[R_{ij} - 2K_{ij}^2 + trK\ K_{ij} - S_{ij} + \frac{1}{2}\,(trS - \tau)\ \gamma_{ij} \right] \tag{3.2}$$

(ADM evolution system).

The constraints are not enforced during evolution, although one can use the differences

$$\mathcal{E} \equiv \frac{1}{2}\,[\,tr\,R + (tr\,K)^2 - tr(K^2)\,] - \tau = 0 \tag{3.3}$$

$$\mathcal{M}_i \equiv \nabla_j\ (K_i{}^j - trK\ \delta_i{}^j) - S_i = 0 \tag{3.4}$$

as error indicators in order to monitor the quality of the numerical simulations.

The consistency of the free evolution approach relies in the fact that energy and momentum constraints are first integrals of the evolution system. In the

C. Bona and C. Palenzuela Luque: *Elements of Numerical Relativity*, Lect. Notes Phys. **673**, 41–65 (2005)
www.springerlink.com

previous chapter, we derived this result (2.65, 2.66) from the conservation of both the Einstein and the stress-energy tensors. In the specific case of the ADM system (3.1, 3.2), allowing for (2.71), we get the 'subsidiary system'

$$\frac{1}{\alpha}\left(\partial_t - \mathcal{L}_\beta\right)\,\mathcal{E} + \nabla_j\,\mathcal{M}^j = 2\,\mathcal{E}\;trK - 2\,\mathcal{M}^j\,\partial_j\,ln\alpha \tag{3.5}$$

$$\frac{1}{\alpha}\left(\partial_t - \mathcal{L}_\beta\right)\,\mathcal{M}_i + \nabla_i\,\mathcal{E} = \mathcal{M}_i\,trK - 2\,\mathcal{E}\,\partial_i\,ln\alpha\;, \tag{3.6}$$

so that it is clear again that Einstein's solutions will be recovered if and only if the initial data verify

$$\mathcal{E} = 0 \qquad \mathcal{M} = 0\;. \tag{3.7}$$

In numerical simulations, however, one must allow for the errors which are inherent to any approximation. This is why we are interested on using a well-posed evolution system. By this we mean that small perturbations of the initial data should not carry us too far away from the original solution (a more precise definition can be found for instance in [14]). A well-posed evolution system implies the stability of the solutions at the continuum level, which is a necessary condition for the stability of numerical solutions. In this way, we could ensure that violations of the constraints (3.7) arising during numerical evolution would not grow too fast, so that the numerical solution would be a consistent approximation to the exact Einstein's equations solution, to the required accuracy level.

3.1.2 Extended Solution Space

Let us analyze the situation in more detail. It is clear that the free evolution approach implies using an extended solution space, even at the continuum level: less equations to be fulfilled means more solutions. As a consequence, Einstein's solutions span just a subset of the extended solution space. This subset is characterized by the conditions (3.7), which amount to enforce energy and momentum constraints. This is fully consistent because the subsidiary system (3.5, 3.6) ensures that the constraints (3.7) are preserved, so that every true Einstein's solution remains so during time evolution. As a consequence, there is a clear cut separation between the original solutions and the extended ones.

The situation is depicted in Fig. 3.1. The fact that the ADM system (3.1, 3.2) be well-posed would ensure the stability of the extended set solutions (represented as a rectangle). But true Einstein's solutions, being a subset of the extended ones, would also be stable as a result. This means that they would remain inside their constrained subset (represented as a circle).

Notice also that the extension is not unique: we could choose (2.62) (Einstein evolution system) instead of (3.2) (Ricci evolution system) for the time evolution of the extrinsic curvature, and we would get as a result a different extension of the Einstein's original solution space.

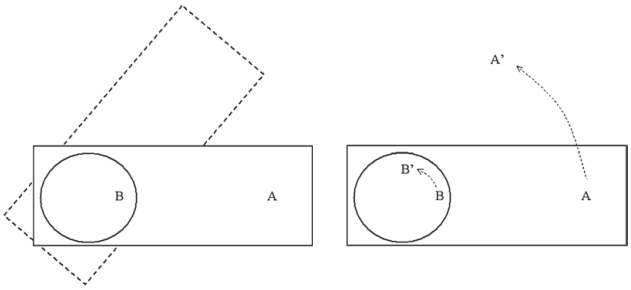

Fig. 3.1. The original Einstein's equations solution space is represented by a *circle*, which is contained into the *rectangle* representing the extended solution space of the ADM free evolution system. The *dotted rectangle* in the *left* drawing represents a different extension of the original solution space. Stability of the ADM solutions would mean that the computed solutions would not drift far away from the exact ones during time evolution. Then, ADM-extended solutions (point A, for instance) would still be solutions after some time, to the required level of accuracy (they will not drift outside the rectangle). This would imply also that true Einstein's equations solutions (point B, for instance) would remain true solutions, to the required level of accuracy (they will not drift outside the circle). The plot on the right drawing shows the effect of a general coordinate transformation, represented here as a mapping with circular *dotted lines*. Point A is mapped into point A', which is outside the ADM-extended solution space. Point B is mapped instead into B', which still represents a true solution

From a different point of view, we must remark that the extended solution space is no longer invariant under general coordinate transformations. Remember that the complete 3+1 version of Einstein's equations has the same solution space of the four-dimensional version. This means that a general coordinate transformation maps solutions into solutions, in spite of the fact that the equations themselves are covariant only under the restricted set of transformations (2.43, 2.44) (3+1 Covariance).

The ADM system is still 3+1 covariant, but remember again that we have obtained it by keeping only the space components of the four-dimensional equations and neglecting the remaining ones. This way we have broken the underlying invariance of the full set of Einstein's solutions, so that general coordinate transformations will no longer map extended solutions into solutions, as depicted in Fig 3.1.

3.1.3 Plane-Wave Analysis

Let us now apply to the ADM system (3.1, 3.2) the plane-wave analysis, as we did in the previous chapter for the complete 3+1 system. But we will first generalize it with a view to further applications:

- The uniform background will be allowed now to take (constant) values different from the Minkowski ones, that is

$$ds^2 = -{\alpha_0}^2\, dt^2 + \gamma^0_{ij}\, dx^i\, dx^j \ . \tag{3.8}$$

This means that index raising and lowering will be made using γ^0_{ij}, which can be now different from δ_{ij}. As a consequence, light rays propagating in the background along a given direction n_i travel with coordinate speed (space interval versus coordinate time interval)

$$\frac{dx^i}{dt} = \pm\, \alpha_0\, n^i \ . \tag{3.9}$$

- The Fourier components of the linear perturbations will be rescaled as follows

$$\delta\alpha = e^{i\,\omega\cdot x}\, a(\omega, t) \tag{3.10}$$
$$\delta\gamma_{ij} = e^{i\,\omega\cdot x}\, h_{ij}(\omega, t) \tag{3.11}$$
$$\delta K_{ij} = (i\omega)\, e^{i\,\omega\cdot x}\, k_{ij}(\omega, t) \ , \tag{3.12}$$

where we must notice the $i\omega$ factor in the last definition. This is because we will look for wave propagation behavior along the chosen direction n_i, that is

$$e^{i\,\omega(n\cdot x\, -\, v\, t)} \ , \tag{3.13}$$

so that the $i\omega$ factor is expected from the equation (3.1) defining the extrinsic curvature in terms of the metric.
- The harmonic slicing condition (2.102) will be generalized to

$$\partial_t\, ln\, \alpha = -\alpha\, f\, tr\, K \tag{3.14}$$

(generalized harmonic slicing), where f is an arbitrary factor that we will include so that geodesic slicing is recovered for $f = 0$ and the original harmonic slicing condition is recovered for $f = 1$.

One can now substitute the perturbations (3.10–3.12) into the linearized ADM system plus the coordinate condition (3.14). This is straightforward if one allows for the expression (2.81) for the three-dimensional Ricci tensor perturbations. In the vacuum case, one gets

$$\partial_t\ (a/\alpha_0) = -i\omega\alpha_0\, f\, tr\, k \tag{3.15}$$
$$\partial_t\ h_{ij} = -2\, i\omega\alpha_0\, k_{ij} \tag{3.16}$$
$$\partial_t\ k_{ij} = -i\omega\alpha_0/2\ [\, h_{ij} - n_i\, h_{nj} - n_j\, h_{ni} + (tr\, h + 2\, a/\alpha_0)\, n_i\, n_j\,] \tag{3.17}$$

and we will write down this linear system in matrix form:

$$\partial_t\, \mathbf{u} = -i\, \omega\, \mathbf{A}\, \mathbf{u} \ , \tag{3.18}$$

where $\mathbf{u}$ is the array of (the Fourier components of the) perturbations,

$$\mathbf{u} = (a\ ,\ h_{ij}\ ,\ k_{ij}) \ . \tag{3.19}$$

The geometric properties of the matrix $\mathbf{A}$ (characteristic matrix) are obviously related with the dynamics of the perturbations:

- The eigenvectors of **A** describe modes evolving in time as plane waves (3.13), provided that their corresponding eigenvalues are real. Notice, however, that every physical mode will affect some component of both the metric and its time derivative (the extrinsic curvature), so that it will consist on two eigenvectors.
- Every (real) eigenvalue provides the propagation speed v of the corresponding characteristic mode (characteristic speeds).

The fact that one has a complete set of eigenvectors corresponding to real eigenvalues is important from the physical point of view, because it means that all the modes are wave-like, so that they keep bounded during time evolution. A first order system verifying this would be said to be 'strongly hyperbolic' [14]. The systems we are considering here are of a mixed type: first order in time, but second order in space. This is why we will coin the term 'pseudo-hyperbolic' for systems of mixed order with this property. Also, we will use the term 'weakly pseudo-hyperbolic' in this context when all the eigenvalues are real, but **A** can not be fully diagonalized, so that the set of eigenvectors is not complete (the analogous of weak hyperbolicity for fully first order systems).

In the case of the ADM system, the characteristic matrix can easily put into a block-diagonal form. One gets from (3.10–3.12) three uncoupled sectors, containing different types of terms:

- **The Transverse sector**, given by

$$\partial_t\, h_{\perp\perp} = -2\, i\omega\alpha_0\ k_{\perp\perp}\ , \qquad \partial_t\, k_{\perp\perp} = -i\omega\alpha_0/2\ h_{\perp\perp}\ , \tag{3.20}$$

  which consists in six degenerate eigenvectors with light speed $v = \pm\,\alpha_0$ as their characteristic speed.
- **The Mixed sector**, given by

$$\partial_t\, h_{n\perp} = -2\, i\omega\alpha_0\ k_{n\perp}\ , \qquad \partial_t\, k_{n\perp} = 0\ , \tag{3.21}$$

  which consists in a four-dimensional degenerate box with zero as the common eigenvalue, but only two eigenvectors ($k_{n\perp}$), so that the other two ($h_{n\perp}$) can grow linearly with time.
- **The Gauge sector**, given by

$$\partial_t\, tr\, h = -2\, i\omega\alpha_0\ tr\, k\ , \tag{3.22}$$

$$\partial_t\, (a/\alpha_0) = -i\omega\alpha_0\, f\, tr\, k\ , \tag{3.23}$$

$$\partial_t\, tr\, k = -i\omega\alpha_0\ a\ , \tag{3.24}$$

  which can be fully diagonalized in the generic case, with eigenvalues zero and $v = \pm\,\sqrt{f}\,\alpha_0$ (gauge speed). The only exception is the $f = 0$ case, which corresponds to geodesic slicing: the gauge sector can not be fully diagonalized and therefore non-oscillatory growing modes appear, as discussed in the previous chapter.

It follows that the ADM system can be at most weakly pseudo-hyperbolic, when the gauge parameter f is non-negative. But the mixed sector shows that, independently of gauge considerations, the system can not be pseudo-hyperbolic in the strong sense so that the linear growing modes in the mixed sector can not be avoided. This is in contrast with what we got for the full Einstein system, where either the maximal or the harmonic slicing conditions allowed us to dispose of such annoying modes. This is the price one pays for neglecting the constraints in the free evolution approach. We will see in the next section how high this price can be in numerical simulations and, in the following ones, how one can modify the ADM system (3.1, 3.2) in order to obtain free evolution pseudo-hyperbolic systems more suitable for building numerical codes.

Could we conclude that the ADM system (3.1, 3.2) is well posed?. Well, it is just a matter of definition. In the mathematical literature, the concept of 'perturbations growing not too fast' is defined in a weak way, so that polynomial growth is admissible [14]. In this sense, the linear modes we have found are not a problem and the ADM system could be well-posed in this weak sense. But we could adopt on physical grounds a stronger requirement so that 'perturbations growing not too fast' is replaced by 'perturbations having an upper bound' and the ADM system can not be well posed in this strong sense.

3.2 Robust Stability Test-Bed

In this section, we will perform a simple numerical test-bed [15] in order to check out the results of the previous section. The idea is to start from initial data consisting in a flat background (Minkowski metric) plus a random perturbation in every dynamical field. The initial level of the random noise must be small enough to make sure that we are testing just the linear regime, allowing even for the cumulative effects during the time elapsed in the simulation. One should see then a linear growth of the noise level when using the weakly pseudo-hyperbolic ADM system, in contrast with the constant noise level one should get when using any of the pseudo-hyperbolic systems which will be discussed in the following sections.

Besides its use as a cross-check of analytical calculations, the robust stability test-bed can be also useful in two other ways:

- As a direct check of the pseudo-hyperbolic character of a given system, when the analytical calculations are hard to perform, or even when one wants to explore the non-linear regime.
- As a tool for tuning the numerical methods: fixing the time resolution or other adjustable parameters in order to keep stability by avoiding at the same time adding too much numerical dissipation.

We will take advantage of these possibilities here, but let us first introduce what we consider to be the simplest discretization methods, which will be used in our test-bed simulations.

3.2.1 The Method of Lines

The method of lines (MoL) [16] is the generic name of a family of discretization methods in which the time and space variables are dealt with separately. This is in keeping with the 3+1 framework, where the natural way of time discretization is by using finite differences whereas one would like to keep all the options open for space discretization: finite differences, finite elements or even spectral methods.

To illustrate the idea, let us consider a 'semi-discrete' system in which only the time coordinate is discretized, whereas space derivatives are kept at the continuum level, that is

- The evolution of the array $\mathbf{u}$ of dynamical fields is written as

$$\partial_t \, \mathbf{u} = \mathbf{S} \tag{3.25}$$

  where the right-hand side array $\mathbf{S}$ contains the remaining terms in the evolution equations, including the space derivatives ones.
- The continuous flow of time is then approximated by a discrete succession of instants, labelled as $\{t_n\}$. The values of the $\mathbf{u}$ array at every instant are then labelled as

$$\mathbf{u}^{(n)} = \mathbf{u}(t_n) \; . \tag{3.26}$$

- The first order approximation for the time evolution between two successive instants, separated by a time interval Δt, is provided by the basic Euler step (forward time difference)

$$\mathbf{u}^{(n+1)} = \mathbf{u}^{(n)} + \Delta t \; \mathbf{S}(t_n, \mathbf{u}^{(n)}) \; . \tag{3.27}$$

In this way, we are disguising in (3.25) the original system of partial differential equations (PDE) as a system of ordinary differential equations (ODE), assuming that we will manage to compute the right-hand-side term $\mathbf{S}$ at every time level, but ignoring for the moment the details. This 'black box' approach allows us to apply the well known ODE discretization techniques to get the required time resolution, using the Euler step (3.27) as the basic building block.

A simple Runge-Kutta algorithm would read for instance [17]

$$\mathbf{S}^{(n)} = \mathbf{S}(t_n, \mathbf{u}^{(n)}) \tag{3.28}$$

$$\mathbf{u}^{*} = \mathbf{u}^{(n)} + \Delta t \; \mathbf{S}^{(n)} \tag{3.29}$$

$$\mathbf{u}^{(n+1)} = \frac{1}{2} \; \mathbf{u}^{(n)} + \frac{1}{2} \; \mathbf{u}^{*} + \frac{\Delta t}{2} \; \mathbf{S}^{*} \; , \tag{3.30}$$

so that one gets second order time accuracy, meaning that time discretization errors are of order $(\Delta t)^3$, as it can be easily verified by developing (3.30) as a Taylor series in time around t_n . Higher order time accuracy can be achieved in a similar way.

'Dumb' algorithms, like (3.30), do not incorporate any quality control, which could adjust dynamically the time step to fulfill some accuracy criterion, by reducing it when needed to preserve the required accuracy or even by enlarging it when possible in order to save computational resources. Let us remember that the preservation of the constraints (3.7) provides such kind of criteria, so that 'clever' algorithms with variable step size can be devised in a natural way [18]. The only warning is that the discretization of the space derivatives, which we have ignored for the moment, can set an upper limit for the size of the time step, dictated by the stability condition of the space discretization algorithm. We will discuss this in what follows.

3.2.2 Space Discretization

As stated before, the method of lines can be used with any space discretization method. We will choose here again the finite difference method, so that every space slice, corresponding to a given instant, will be approximated as a three-dimensional grid. Every grid node will be labelled by a set of three indices (i, j, k), one for every coordinate axis. The field values at the grid nodes will be then represented by the array

$$\mathbf{u}_{i,j,k} = \mathbf{u}(t, x_i, y_j, z_k) \; . \tag{3.31}$$

The space derivatives in the right-hand-side of (3.25) can be discretized in many ways. In the simplest case, we will use evenly spaced numerical grids, so that the space intervals are of constant size along every direction, namely

$$\Delta x \; , \qquad \Delta y \; , \qquad \Delta z \; . \tag{3.32}$$

Then we can get second order space accuracy for the partial derivatives easily by using centered differences. In the case of the first x derivatives, for instance, the simplest choice is

$$2\,\partial_x u \sim (u_{i+1,j,k} - u_{i-1,j,k})/\Delta x \; , \tag{3.33}$$

and the same rule can be applied to the other directions. This 'centering' strategy can also be applied to second partial derivatives, namely

$$2\,\partial_{xx} u \sim (u_{i+1,j,k} + u_{i-1,j,k} - 2u_{i,j,k})/(\Delta x)^2 \; , \tag{3.34}$$

$$\begin{aligned} 4\,\partial_{xy} u \sim (&u_{i+1,j+1,k} - u_{i-1,j+1,k} \\ &-u_{i+1,j-1,k} + u_{i-1,j-1,k})/(\Delta x \Delta y) \; , \end{aligned} \tag{3.35}$$

in order to get again the required second order accuracy.

Numerical grids are obviously of a finite size, so that they must begin and end at some point along every direction. For these boundary points, one can no longer use expressions like (3.33) or (3.34), which would require neighbor nodes on both sides: at least one such neighbors does not exist at the outermost

grid points. As far as we are not interested in boundary effects for the moment, we will assume here that our grid has periodic boundaries along every axis (from the geometrical point of view, this implies the topology of a three-torus). Allowing for this, we will assume that the last two nodes at the end of any axis are identical to the first two ones at the beginning, and vice-versa. For instance:

$$u_{N,j,k} = u_{2,j,k} \ , \qquad u_{1,j,k} = u_{N-1,j,k} \ , \tag{3.36}$$

so that the centered expressions for the first and second partial derivatives (3.33, 3.34) are applied only for $i = 2, \ldots N-1$, whereas (3.36) provides the required values at the boundary points $i = 1, N$. We are aware that, in most Numerical Relativity applications, periodic boundary conditions like (3.36) would not be consistent with the physics of the problem. But for the moment we are planning to deal just with some test-bed problems, where periodic boundaries could be assumed consistently, in order to focus on the numerical treatment of the generic (interior) points.

In the finite difference approach, the set of grid points needed to discretize space derivatives at a given point P is named as 'the stencil'. The stencil provides the numerical domain of dependence of the selected point P, in the sense that any perturbation at one of the stencil points will change the computed value at P after a single Euler step (3.27). We can even define the numerical propagation speed as

$$v^i_{num} = \frac{s \Delta x^i}{\Delta t} \ , \tag{3.37}$$

where s stands here for the stencil size, that is the maximum number of stencil points besides P along any direction. For instance, we have $s = 1$ in the second derivative expressions (3.34), but one could use instead

$$4\, \partial_{xx}\, u \sim (u_{i+2,j,k} + u_{i-2,j,k} - 2u_{i,j,k})/(\Delta x)^2 \ , \tag{3.38}$$

which would imply $s = 2$.

From the physical point of view, as far as our system describes propagation with some characteristic speeds, the field values at P are causally determined by the values inside the past half-cone with vertex at P, which slope is given by (the inverse of) the largest characteristic speed of the system. This provides the physical domain of dependence of P. In our case, the largest characteristic speed is either light speed $v = \alpha_0$ or the gauge speed $v = \sqrt{f}\, \alpha_0$ (usually $f > 1$, so that gauge speed is actually the largest one).

As seen in Fig. 3.2, depending on the size of the time step Δt, the physical domain of dependence of P can be or not fully contained in the numerical domain of dependence. Consistency requires that the numerical domain of dependence should contain every point that can have a physical influence on P. Otherwise the numerical solution is not allowing for the causal behavior of the dynamical system and this will lead to numerical instabilities, which is the only way our numerical algorithm has to avoid converging to the physical solution.

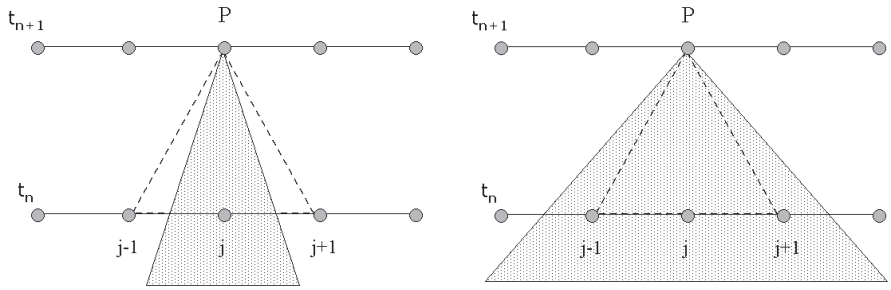

Fig. 3.2. The numerical domain of dependence of a point P in a finite difference grid is represented as a *dotted triangle*, which slope is the inverse of the numerical propagation speed ($s = 1$ here). The physical domain of dependence of P is represented as a *dark triangle*, which slope is the inverse of the largest characteristic speed along the given axis. The Courant stability condition is fulfilled in the left drawing, where the physical domain of dependence is fully contained into the numerical one. Violating the Courant condition, as depicted in the right drawing, would lead to numerical instabilities

A necessary condition for numerical stability will be then the Courant condition, stating that the largest characteristic speed v_{max} along every given direction n_i can not exceed the corresponding numerical speed,

$$v_{max} \; < \; n_i \, v^i_{\;num} \; . \tag{3.39}$$

For instance, let us consider the x direction and let us assume $f \geq 1$; the Courant condition (3.39) provides then an upper limit for the numerical time step, namely

$$\Delta t \; < \; \frac{s \Delta x}{\alpha_0 \sqrt{f \, \gamma_0^{xx}}} \; . \tag{3.40}$$

In numerical simulations, the time step limit (3.40) must be checked at the beginning of every new time level computation. It must be checked at every grid point and along every axis, keeping always the most restrictive upper bound on the time step. Usually, an extra safety factor is included, so that the upper bound gets even more restrictive. This supplementary factor is usually adjusted by trial and error, either in order to avoid an excess of numerical dissipation or to suppress other unexpected instabilities.

3.2.3 Numerical Results

Let us now proceed to the numerical simulation. We will set up a cubic grid of 'only' 50 points along every axis, with periodic boundary conditions. Although we have 50^3 points, the job can be done easily by using a standard personal computer, even a laptop. Space resolution is not an issue here (we will evolve just noise), so that the number of points could be reduced as needed: for

instance, we could take advantage of the periodic boundaries condition to set up instead a 'channel' of $50 \times 5 \times 5$ points if we want a quicker response.

We will measure time in 'crossing time' units. This means the time it would take for a light ray to make a full trip across the numerical grid. We will choose our time step to be

$$dt = 0.03\, dx\ . \tag{3.41}$$

Notice that the light speed value is one in the background (Minkowski) metric, so that the Courant condition (3.40) would allow us to take a time step even ten times larger. But we prefer to be extremely cautious here about introducing too much numerical dissipation which could artificially lower the noise level, masking the true properties of the evolution system.

We have plotted in Fig. 3.3 our results for the standard harmonic case ($f = 1$). We see the expected linear growth of the ADM system. Notice the catastrophic exponential growth after some 150 crossing times, revealing a non-linear instability. We will limit ourselves to discussing the linear regime as a test for the wave propagation properties of the system. In this sense, the linear growth of the ADM plot in Fig. 3.3 confirms the weakly hyperbolic character of the ADM system.

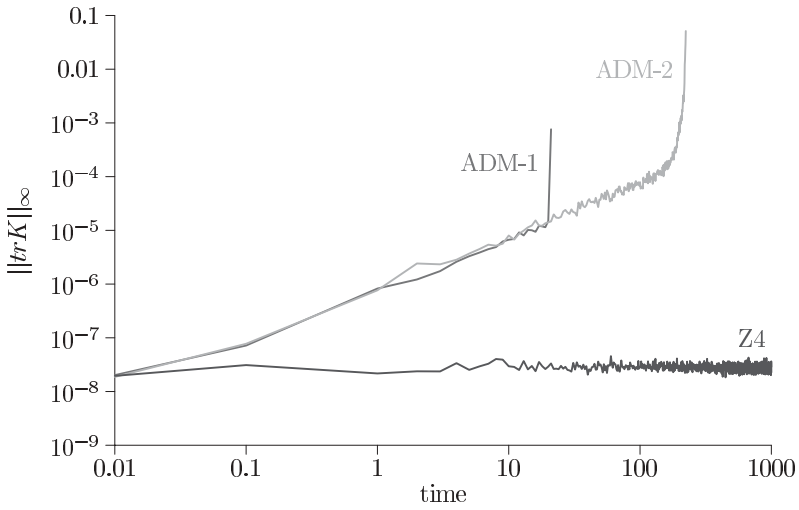

Fig. 3.3. The maximum of (the absolute value of) trK is plotted against the number of crossing times in a logarithmic scale. The initial level of random noise remains constant during the evolution in the case of any of the pseudo-hyperbolic systems that we will describe in what follows (the Z4 one is shown here). In the case of the ADM free evolution system, which is only weakly pseudo-hyperbolic, a linear growth is detected up to the point where the code crashes. The label ADM-1 corresponds to a numerical simulation using a fully first order version of the ADM system, which will be introduced in the next chapter

The Z4 system, which will be introduced at the end of this chapter, shows instead the constant behavior which one would expect from a strongly pseudo-hyperbolic system. The same qualitative behavior is shown by the BSSN system, that will also be introduced later.

Let us briefly discuss the role of numerical dissipation. Every discrete algorithm is just an approximation to the exact equations. Discretization error terms can be classified into two main categories

- **Dispersion errors**, which affect the propagation speeds in a way that depends of the frequency of every perturbation.
- **Dissipation errors**, which affect the growth of perturbations.

The wrong sign in the dominant dissipation error terms (perturbations explosion) leads to unstable numerical codes. The right sign there leads to stable codes, at the price of some amount of dissipation. The more accurate the numerical algorithm is, the less numerical dissipation it contains.

This is why we recommend using at least third-order accurate algorithms for time evolution. In the simulations presented here, the following third-order Runge-Kutta algorithm [17]

$$\mathbf{u}^{*} = \mathbf{u}^{(n)} + \Delta t\, \mathbf{S}^{(n)} \tag{3.42}$$

$$\mathbf{u}^{**} = \frac{3}{4}\, \mathbf{u}^{(n)} + \frac{1}{4}\, \mathbf{u}^{*} + \frac{\Delta t}{4}\, \mathbf{S}^{*} \tag{3.43}$$

$$\mathbf{u}^{(n+1)} = \frac{1}{3}\, \mathbf{u}^{(n)} + \frac{2}{3}\, \mathbf{u}^{**} + \frac{2}{3}\, \Delta t\, \mathbf{S}^{**}\,, \tag{3.44}$$

is used instead of the simple second-order one (3.30). We can see the difference by comparing Figs. 3.3 and 3.4, where in the latter the third-order Runge-Kutta algorithm (3.44) is replaced by the 'Iterative Cranck-Nicolson' (ICN) method, which is a second-order predictor-corrector algorithm. Although everything else is the same (space and time resolution, space discretization method, initial data), we see that reducing the accuracy of the time evolution discretization is enough to completely distort the plots, masking the effects we were looking for.

3.3 Pseudo-Hyperbolic Systems

Allowing for the performance of the ADM system in the robust stability testbed, one can wonder that it was the evolution system of reference until the beginning of the 1990's. Poor resolution, as a consequence of the available computing resources, combined with the use of dissipative numerical methods, masked the weakly stable nature of the formalism, as we have seen in Fig. 3.4. Free evolution with the ADM system has been the approach actually used by the main Numerical Relativity groups in the long way from the pioneering spherically symmetric or axially symmetric numerical codes [11, 12] towards the generic three-dimensional simulations that are routinely performed today.

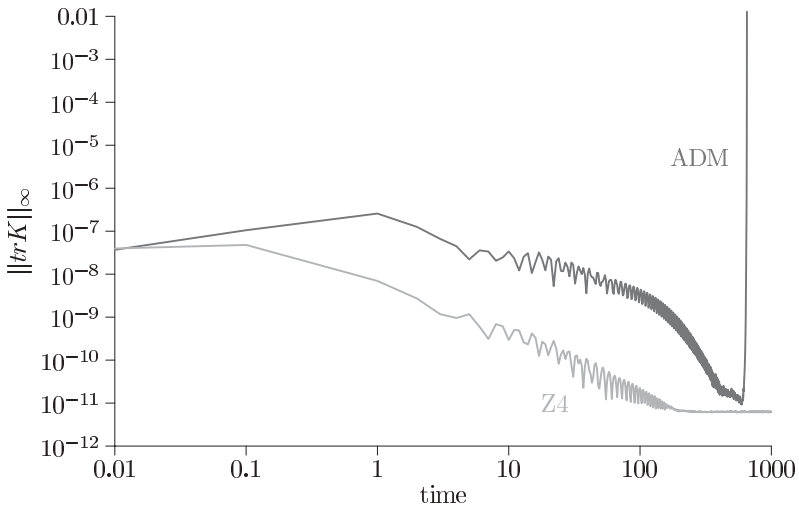

Fig. 3.4. Same as in the previous figure, but replacing the third order Runge-Kutta time-evolution algorithm by a second order predictor-corrector one (ICN). Numerical dissipation is severely distorting the plots, by masking the linear growth in the ADM case and dramatically reducing the initial noise level in the pseudo-hyperbolic case. Notice than both dt and dx are the same as in the previous figure, and we are using also the same space discretization algorithm: only the time evolution method has changed

3.3.1 Extra Dynamical Fields

Looking for a better alternative, one can take advantage of an old result, currently used in analytical approximation schemes to Einstein's field equations. The standard expression of the three-dimensional Ricci tensor in terms of the connection coefficients

$$R_{ij} = \partial_k \Gamma^k_{ij} - \partial_i \Gamma^k_{kj} + \Gamma^k_{kr}\Gamma^r_{ij} - \Gamma^k_{ri}\Gamma^r_{kj} \ , \tag{3.45}$$

can be rewritten, by reordering the second partial derivatives, as the De Donder-Fock [20, 21] decomposition

$$R_{ij} = \gamma^{rs}\left[-\frac{1}{2}\,\partial^2_{rs}\gamma_{ij} + \partial_{(i}\Gamma_{j)rs} - \Gamma^k_{ij}\,\Gamma_{krs} + \gamma^{kl}\left(\partial_k\gamma_{ir}\,\partial_l\gamma_{js} - \Gamma_{irk}\,\Gamma_{jsl}\right)\right] . \tag{3.46}$$

A first look at the second derivative terms in (3.46) reveals that they can be written as the sum of the ordinary Laplacian of the space metric plus the symmetrized partial derivatives of the combination

$$\Gamma_i = \gamma^{rs}\,\Gamma_{irs} \ . \tag{3.47}$$

The Laplacian term is welcome if one wants to get the expected oscillatory behavior for the linear perturbations. In analytical perturbation approaches, which use the four-dimensional version of the decomposition (3.46), the four-dimensional analogous of the quantities (3.47) are made to vanish by a very particular choice of the four spacetime coordinates (harmonic coordinates), taking advantage of the non-tensor character of (3.47). We will not follow that way, because we prefer to preserve our coordinate freedom as longer as possible. Therefore, we must adopt another strategy, which should work in a generic coordinate system.

The crucial point is to consider instead the quantities Γ_i as the components of a new dynamical field, no longer related with the metric derivatives trough (3.47). To be consistent with this interpretation, one must provide an independent evolution equation for the 'extra' field. And this can be done if we allow for the fact that the momentum constraint (3.4) contains space derivatives of the extrinsic curvature, which can be seen itself as a time derivative of the space metric. One can then switch the order of space and time derivatives in (3.4), by rewriting it as the evolution equation of the combination

$$V_i = \frac{1}{2}\left(\Gamma^k_{ki} - \Gamma_i\right) , \tag{3.48}$$

which is directly related with Γ_i.

Let us write down the linearized version of the resulting 'Bona-Massó' system in order to see its structure in a more transparent way:

$$\partial_t\ (\delta\gamma_{ij}) = -2\alpha_o\ (\delta K_{ij}) \tag{3.49}$$

$$\partial_t\ (\delta K_{ij}) = -\partial^2_{ij}\,(\delta\alpha) + \alpha_o\,(\delta R_{ij}) \tag{3.50}$$

$$\partial_t\ (\delta V_i) = 0\ , \tag{3.51}$$

where the linear perturbation of the Ricci tensor is given now by

$$\delta R_{ij} = -\frac{1}{2}\,\gamma_o{}^{rs}[\,\partial^2_{rs}(\delta\gamma_{ij}) - \partial^2_{ij}(\delta\gamma_{rs})\,] - \partial_i\,(\delta V_j) - \partial_j\,(\delta V_i)\ . \tag{3.52}$$

Notice that the perturbations of the extra field V_i are considered here to be independent of the metric and gauge perturbations, so that their evolution equation (3.51) is a genuine part of the free evolution system. This does not mean that the momentum constraint (3.4) has disappeared. It has only been transformed into the algebraic form (3.48), that is

$$V_i = \frac{1}{2}\,\gamma^{\,rs}[\,\partial_i\,(\gamma_{rs}) - \partial_r\,(\gamma_{is})\,]\ , \tag{3.53}$$

which can still be used to monitor the quality of the simulation.

The Bona-Massó evolution system was first obtained in the context of fully first order systems, which we will discuss in the next chapter. In the first (1992) paper [22], it was shown to be hyperbolic in that context for the harmonic

slicing case. This result was later (1995) extended to the generalized harmonic case [23], which includes the robust slicing conditions currently used at that time to deal with spherically symmetric black holes. It opened the way to the use in the Numerical Relativity context of the 'shock-capturing' algorithms currently used in Computational Fluid Dynamics (CFD). These advanced techniques produced a breakthrough in the state-of-the-art numerical black-hole simulations, as shown in Fig 3.5.

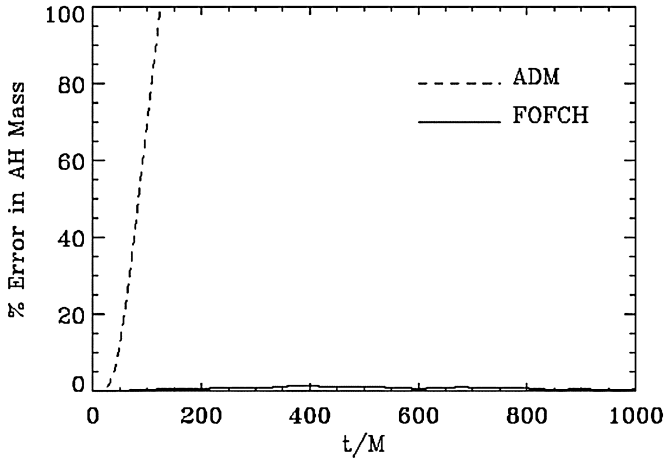

Fig. 3.5. The error in the apparent horizon mass of a spherically symmetric black hole is plotted against time. The analytical result is known to be time-independent. The term FOFCH, for 'First-Order Flux-Conservative Hyperbolic', refers here to a 1D code based on (the first order version of) the Bona-Massó formalism [23]. The use of advanced CFD techniques, which require a full set of characteristic eigenvectors, when combined with the use of robust slicing conditions, allow to continue the black hole evolution 'forever', provided that the boundary conditions are set in a suitable way

3.3.2 The BSSN System

The idea of transforming the momentum constraint into an evolution equation for some extra fields is also behind the formalism introduced just a little bit later by Shibata and Nakamura [24], much widely known after the work of Baumgarte and Shapiro [25] (BSSN system). The metric coefficients γ_{ij} are there expressed in terms of a conformal metric:

$$\tilde{\gamma}_{ij} = e^{-4\,\phi}\,\gamma_{ij} \tag{3.54}$$

with unit determinant, so that

$$e^{4\,\phi} = \gamma^{1/3} = [det(\gamma_{ij})]^{1/3} \tag{3.55}$$

The second fundamental form K_{ij} is also decomposed into its trace and trace-free components, namely

$$K = \gamma^{ij}\, K_{ij} \tag{3.56}$$

$$\tilde{A}_{ij} = e^{-4\,\phi}\, \left(K_{ij} - \frac{1}{3}\, K\, \gamma_{ij} \right) . \tag{3.57}$$

The conformal decomposition (3.54) allows one to compute easily the connection coefficients of the conformal metric in terms of the original ones, namely

$$\tilde{\Gamma}^k_{ij} = \Gamma^k_{ij} - 2\,[\,\delta^k_i \phi_j + \delta^k_j \phi_i - \phi^k \gamma_{ij}\,] , \tag{3.58}$$

so that one can split the three-dimensional Ricci tensor appearing in the ADM evolution equations (3.2) into the corresponding Ricci tensor of the conformal metric plus some space derivatives of the conformal factor:

$$R_{ij} = \tilde{R}_{ij} - 2\,\tilde{\nabla}_i \phi_j + 4\,\phi_i \phi_j - \tilde{\gamma}_{ij}\,\tilde{\gamma}^{rs} (2\,\tilde{\nabla}_r \phi_s + 4\,\phi_r \phi_s) . \tag{3.59}$$

The extra field in the BSSN formalism is provided by the contracted conformal connection, that is

$$\tilde{\Gamma}^i = \tilde{\gamma}^{rs} \tilde{\Gamma}^i_{rs} \;= -\tilde{\gamma}^{ij}_{\;\;,j} , \tag{3.60}$$

which can be related with the extra fields (3.48) of the Bona-Massó formalism as follows

$$V_i = -\frac{1}{2}\, \tilde{\gamma}_{ij} \tilde{\Gamma}^j + 4\,\phi_j , \tag{3.61}$$

so that the conformal Ricci tensor can be finally written as

$$\begin{aligned} \tilde{R}_{ij} = {} & \frac{1}{2}\, \tilde{\gamma}^{rs}\, [\, -\partial^2_{rs} \tilde{\gamma}_{ij} + 4\, \tilde{\Gamma}^k_{r(i}\, \tilde{\Gamma}_{j)ks} + 2\, \tilde{\Gamma}^k_{ri}\, \tilde{\Gamma}_{ksj}\,] \\ & + \tilde{\gamma}_{k(i}\, \partial_{j)} \tilde{\Gamma}^k + \tilde{\Gamma}^k\, \tilde{\Gamma}_{(ij)k} . \end{aligned} \tag{3.62}$$

The full list of BSSN independent dynamical fields is then given (in the zero shift case) by

$$u = \{\alpha,\ \phi,\ \tilde{\gamma}_{ij},\ K,\ \tilde{A}_{ij},\ \tilde{\Gamma}^i\} . \tag{3.63}$$

Up to now, the formulas (3.54–3.61) just provide a recombination of the basic dynamical fields, but no new equations. The main differences between the BSSN and the Bona-Massó evolution systems are

- The evolution equation for the trace K of the extrinsic curvature in the BSSN case is not the one that would follow from taking the trace of the evolution equation of K_{ij} in a straightforward way. One must use instead the energy constraint to transform the trace equation, before doing all the replacements, into

$$\partial_t\, K = -\triangle\, \alpha + \alpha\, \left[tr(K^2) + \frac{1}{2}\, (trS + \tau) \right] . \tag{3.64}$$

This is another instance of the use of the energy constraint to modify the free evolution system: we did the same in the previous chapter, where we compared the 'Ricci' evolution system (2.59) with the 'Einstein' one (2.62). We will see in the following section how to do it in a more systematic way.

- The conformal decomposition, as used in the BSSN formalism, generates new constraints. It follows from (3.54–3.57) that

$$det(\tilde{\gamma}) = 1 \,, \qquad trA = 0 \,. \tag{3.65}$$

These algebraic constraints can be very useful for monitoring numerical errors. The current practice is to 'correct' these errors by rescaling $\tilde{\gamma}_{ij}$ and resetting the trace of $\tilde{A}_{ij}$ to zero from time to time during the calculation, even after every single time step. This 'semi-constrained' approach can affect convergence tests, where the rate of convergence that one could expect from the discretization method of the 'free evolution' algorithm can differ from the actual results.

3.3.3 Plane-Wave Analysis

Now we can proceed to perform the plane-wave analysis that we introduced for the ADM system at the beginning of this chapter. We will do it just for the Bona-Massó case in order to avoid the complications associated with the conformal decomposition. Remember that this decomposition, as well as the selection of one or another of the related quantities (3.61) as the extra field, is only a rearrangement of the dynamical quantities, so that the intrinsic properties of the evolution system remain actually the same ones. This means that our results will apply also to the BSSN system, with only a minor difference in the gauge sector, due to the use of the modified equation (3.64) for $tr\,K$.

Let us start then from the linearized system (3.49–3.51). The Fourier components of the dynamical perturbations will be written as follows

$$\delta\alpha = e^{i\,\omega\cdot x}\, a(\omega, t) \tag{3.66}$$

$$\delta\gamma_{ij} = e^{i\,\omega\cdot x}\, h_{ij}(\omega, t) \tag{3.67}$$

$$\delta K_{ij} = (i\omega)\, e^{i\,\omega\cdot x}\, k_{ij}(\omega, t) \tag{3.68}$$

$$\delta V_k = (i\omega)\, e^{i\,\omega\cdot x}\, v_k(\omega, t) \,, \tag{3.69}$$

where we have scaled the Fourier coefficients of V_k with the same $i\omega$ factor as the K_{ij} ones.

One can now substitute (3.66–3.69) into the linear system (3.49–3.51) plus (the linear version of) the coordinate condition (3.14) in order to get the time evolution equations for the array of the Fourier-transformed perturbations,

$$\mathbf{u} = (a \,,\; h_{ij} \,,\; k_{ij} \,,\; v_k) \,. \tag{3.70}$$

Notice that one must use now the expression (3.52) instead of (2.81) for the three-dimensional Ricci tensor perturbations. In the vacuum case, one gets

$$\partial_t\ (a/\alpha_0) = -i\omega\alpha_0\, f\, tr\, k \tag{3.71}$$
$$\partial_t\ h_{ij} = -2\, i\omega\alpha_0\, k_{ij} \tag{3.72}$$
$$\partial_t\ k_{ij} = -i\omega\alpha_0/2\ [\, h_{ij} + 2(n_i\, v_j + n_j\, v_i) + (tr\, h + 2\, a/\alpha_0)\, n_i\, n_j\,] \tag{3.73}$$
$$\partial_t\ v_k = 0\ . \tag{3.74}$$

In order to write down the characteristic matrix, it is convenient to rearrange the dynamical fields array (3.70) in a way that clearly separates the transverse, longitudinal and gauge sectors, as we did in the ADM case:

$$\mathbf{u} = (h_{\perp\perp}\ ,\ k_{\perp\perp}\ ,\ h_{n\perp}\ ,\ k_{n\perp}\ ,\ v_\perp\ ,\ trh\ ,\ trk\ ,\ a/\alpha_0\ ,\ v_n)\ . \tag{3.75}$$

The characteristic matrix is given in this basis in a simple block-diagonal form

$$\mathbf{A} = \begin{pmatrix} 0 & 2\alpha_0 & & & & & & & \\ \alpha_0/2 & 0 & & & & & & & \\ & & 0 & 2\alpha_0 & 0 & & & & \\ & & \alpha_0/2 & 0 & \alpha_0 & & & & \\ & & 0 & 0 & 0 & & & & \\ & & & & & 0 & 2\alpha_0 & 0 & \\ & & & & & 0 & \alpha_0 & 2\alpha_0 & \\ & & & & & f\alpha_0 & 0 & 0 & \\ & & & & & & & 0 & \end{pmatrix} \tag{3.76}$$

(the values not shown are zero), so that it follows that

- The **eigenvalues** (propagation speeds) are either zero (static modes, like the (3.74) ones), or the background metric light speed $\pm\alpha_0$, or the 'gauge speed' $\pm\sqrt{f}\,\alpha_0$. The requirement of real propagation speeds amounts then to the condition $f \geq 0$ on the gauge parameter f.
- A complete set of **eigenvectors** can be obtained in the generic case, with the only exception of geodesic slicing ($f = 0$), where gauge speed vanishes leading to an extra degeneracy which prevents putting $\mathbf{A}$ in full diagonal form.

We can conclude that the Bona-Massó system is pseudo-hyperbolic for all the generalized harmonic slicing cases for which

$$f > 0\ . \tag{3.77}$$

The same is true for the BSSN system, where only minor changes appear in the corresponding characteristic matrix when compared with (3.76). The main one arises from the choice of the evolution equation (3.64) for $tr\, K$, and it amounts to the vanishing of the $2\alpha_0$ coefficient in the last column (gauge sector). Therefore, it does not affect neither the values of the propagation speeds nor the completeness of the set of eigenvectors.

3.4 The Z4 Formalism

The second order pseudo-hyperbolic formalisms we have discussed here represent an improvement over the free evolution ADM system, both at the theoretical and the numerical applications level, where the pseudo-hyperbolicity property ensures the absence of growing modes in linear perturbations. This fact has proven very useful in 3D Numerical Black Hole simulations, using either the Bona-Massó [26] or the BSSN formalisms [27, 28].

These formalisms, however, share two drawbacks:

- Energy and momentum constraints are treated in a different way. Energy constraint is treated like in the ADM case, by relaxing it during time evolution. Momentum constraint, instead, is considered to provide the evolution equation for some extra dynamical field (V_i or $\tilde{\Gamma}^i$, respectively).
- These extra dynamical quantities have no tensor behavior: neither V_i nor $\tilde{\Gamma}^i$ transform as three-vectors under general space coordinates transformations.

These considerations suggest that these are just intermediate steps towards more advanced formalisms, in which the energy constraint is not left aside and the supplementary dynamical quantities have a well defined tensor character. All these requirements are fulfilled by the 'Z4 formalism'. [29, 30], which will be discussed in what follows.

3.4.1 General Covariant Field Equations

The field equations in the Z4 formalism can be written in a general covariant form at the four-dimensional level, namely

$$R_{\mu\nu} + \nabla_\mu Z_\nu + \nabla_\nu Z_\mu = 8\,\pi\,\left(T_{\mu\nu} - \frac{1}{2}\,T\,g_{\mu\nu}\right)\,, \tag{3.78}$$

where the 'zero' four-vector Z_μ plays the role of the supplementary quantity, so that the full set of dynamical fields consists of the pair

$$\{g_{\mu\nu}, Z_\mu\}\,. \tag{3.79}$$

Here again, the solution space of the original Einstein's equations is extended by introducing the extra dynamical quantity Z_μ. The solutions of the original field equations can of course be recovered by imposing the vanishing of this four-vector, namely

$$Z_\mu = 0\,, \tag{3.80}$$

and the components of this algebraic condition will play the role of the four energy and momentum constraints, as we will see later. One can even use the evolving values of Z_μ during a numerical simulation as a good general-covariant indicator of the quality of the approximation. Notice that, in contrast with the precedent formalisms, the extended solution space is also general

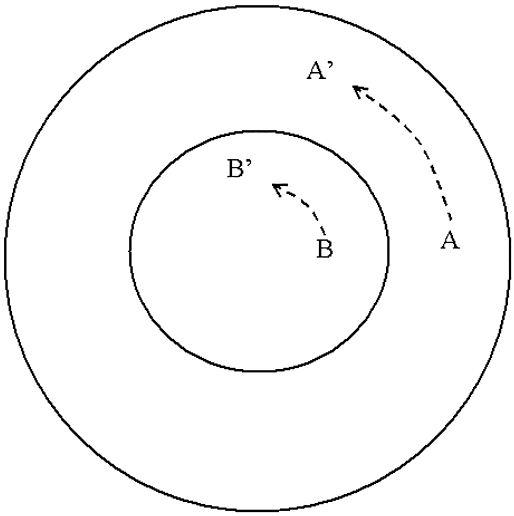

Fig. 3.6. The original Einstein's equations solution space is represented by the *inner circle*, which is contained into the *outer circle*representing the extended solution space of the Z4 system. The plot shows the effect of a general coordinate transformation, represented here as a mapping with circular *dashed lines*. Points A, which represents a Z4-extended solution, and B, representing a true Einstein's solution, are mapped into A' and B', which still represent either a Z4-extended solution or a true Einstein solution, respectively. This is in contrast with the behavior shown in Fig. 3.1 for the ADM system, reflecting the lack of invariance of the ADM-extended solution space

covariant, so that a generic four-dimensional coordinate transformation maps solutions into solutions for both the original Einstein's equations and the Z4 extended ones (3.78) (See Fig. 3.6).

The time evolution of the algebraic constraint (3.80) can be obtained by taking the four-divergence of the field equations (3.78), and allowing for the conservation of both the Einstein tensor $G_{\mu\nu}$ and the Stress-energy tensor $T_{\mu\nu}$. After a straightforward calculation, one gets the linear homogeneous equation

$$\Box\, Z_\mu + R_{\mu\nu} Z^\nu = 0 \ , \tag{3.81}$$

which plays here the role of the subsidiary system (3.5, 3.6). It is of second order in Z_μ, so that the vanishing of both Z_μ and its first time derivatives is needed at the initial slice if we want that the algebraic constraint (3.80) be preserved during time evolution. As we will see below, the vanishing of the first derivatives of Z_μ amounts to imposing the original energy and momentum constraints. This means that the set initial data leading to true Einstein's solutions must consist in an initial metric $g_{\mu\nu}$ verifying the usual energy and momentum constraints plus a zero initial value for the four-vector Z_μ.

3.4.2 The Z4 Evolution System

The general-covariant equations (3.78) can be written in the equivalent 3+1 form [29] (Z4 evolution system)

$$(\partial_t - \mathcal{L}_\beta)\ \gamma_{ij} = -2\,\alpha\,K_{ij} \tag{3.82}$$

$$\begin{aligned}(\partial_t - \mathcal{L}_\beta)\ K_{ij} = &-\nabla_i\alpha_j + \alpha\,\Big[\,R_{ij} + \nabla_i Z_j + \nabla_j Z_i \\ &-2\,K_{ij}^2 + (trK - 2\,\Theta)\,K_{ij} \\ &-S_{ij} + \frac{1}{2}\,(tr\,S - \tau)\,\gamma_{ij}\,\Big]\end{aligned} \tag{3.83}$$

$$\begin{aligned}(\partial_t - \mathcal{L}_\beta)\ \Theta = &\frac{\alpha}{2}\,[\,tr\,R + 2\,\nabla_k Z^k + (trK - 2\,\Theta)\,trK \\ &-tr(K^2) - 2\,Z^k\alpha_k/\alpha - 2\tau]\end{aligned} \tag{3.84}$$

$$\begin{aligned}(\partial_t - \mathcal{L}_\beta)\ Z_i = &\alpha\,[\nabla_j\,(K_i{}^j - \delta_i{}^j trK) + \partial_i\Theta \\ &-2\,K_i{}^j\,Z_j - \Theta\,\alpha_i/\alpha - S_i]\end{aligned} \tag{3.85}$$

where Θ stands for the projection of the four-vector Z_μ along the unit normal n_μ to the space hypersurfaces, namely

$$\Theta \ \equiv\ n_\mu Z^\mu = \alpha\ Z^0\ . \tag{3.86}$$

In the 3+1 form (3.82–3.85), it is evident that the Z4 evolution system consists just in evolution equations. The only constraints (3.80), that can be translated into:

$$\Theta = 0\ , \qquad Z_i = 0\ , \tag{3.87}$$

are algebraic so that the full set of field equations (3.78) is actually used during evolution. As a consequence, a general coordinate transformation will transform Z4-extended solutions into Z4-extended solutions, in spite of the fact that the 3+1 decomposition (3.82–3.85) of the field equations (3.78) is covariant only under the restricted set of transformations (2.43). This point is emphasized in Fig. 3.6.

This is in contrast with the ADM formalism [6], which can be recovered from (3.82–3.85) by imposing (3.87). The first two equations (3.82, 3.83) would transform into the ADM free evolution system, whereas the last two equations (3.84, 3.85) would transform into the standard energy and momentum constraints, that is

$$tr\,R + tr^2 K - tr(K^2) = 2\,\tau \tag{3.88}$$

$$\nabla_j\,(K_i{}^j - \delta_i{}^j trK) = S_i\ . \tag{3.89}$$

These constraints are not enforced in the free evolution approach, so that the ADM-extended solution space is not invariant under a general coordinate transformation (see Fig. 3.1). The same result holds for both the Bona-Massó

and the BSSN formalisms, where the energy constraint (3.88) was still not enforced, although the momentum constraint was treated in a way which anticipated (3.85), as we will see later.

The appearance of the new dynamical quantity Θ, which behaves as a scalar under general space coordinate transformations, allows one to generalize the time slicing condition (3.14) by adding a linear coupling with Θ, that is

$$\partial_t \, ln \, \alpha = -f \alpha \, (tr \, K - m \, \Theta) \; . \tag{3.90}$$

The new gauge parameter m arising here is by no means superfluous, even if it does not change anything for the Einstein's true solutions, where Θ vanishes. The non-trivial parameter value $m = 2$ will be required to get a pseudo-hyperbolic system in the standard harmonic case ($f = 1$), as we will see below.

3.4.3 Plane-Wave Analysis

Let us consider the linearized version of the Z4 system (3.82–3.85) in order to study the propagation of a plane wave in a stationary and homogeneous background (zero shift):

$$\delta \, \gamma_{ij} = e^{i \, \omega \cdot x} \; h_{ij}(\omega, t) \tag{3.91}$$
$$\delta \, \alpha = e^{i \, \omega \cdot x} \; a(\omega, t) \tag{3.92}$$
$$\delta \, K_{ij} = (i \, \omega) \; e^{i \, \omega \cdot x} \; k_{ij}(\omega, t) \tag{3.93}$$
$$\delta \, \Theta = (i \, \omega) \; e^{i \, \omega \cdot x} \; \theta(\omega, t) \tag{3.94}$$
$$\delta \, Z_k = (i \, \omega) \; e^{i \, \omega \cdot x} \; z_k(\omega, t) \; . \tag{3.95}$$

The time evolution of the Fourier coefficients is given by

$$\partial_t h_{ij} = -2 \, (i \, \omega) \; \alpha_0 \; k_{ij} \tag{3.96}$$
$$\partial_t (a/\alpha_0) = -(i \, \omega) \; \alpha_0 \; f \; [\, tr \, k - m \; \theta \,] \tag{3.97}$$
$$\partial_t \theta = -\frac{1}{2} \; (i \, \omega) \; \alpha_0 \; [\, tr \, h - h_{nn} - 2 \, z_n \,] \tag{3.98}$$
$$\partial_t z_i = -(i \, \omega) \; \alpha_0 \; [\, n_i \; (tr \, k - \theta) - k_{ni} \,] \tag{3.99}$$
$$\partial_t k_{ij} = -\frac{1}{2} \; (i \, \omega) \; \alpha_0 \; \lambda_{ij} \tag{3.100}$$

where we have noted

$$\lambda_{ij} \equiv h_{ij} + n_i \; n_j \; (tr \, h + 2 \, a/\alpha_0) - n_i \; (h_{nj} + 2 \, z_j) - n_j \; (h_{ni} + 2 \, z_i) \tag{3.101}$$

and where the symbol n replacing an index means the contraction with the unit vector n_i.

In order to write down the characteristic matrix, it is convenient to re-arrange the dynamical fields array in a way that clearly separates the transverse, longitudinal and gauge sectors, as we did before:

$$\mathbf{u} = (h_{\perp\perp}\ ,\ k_{\perp\perp}\ ,\ h_{n\perp}\ ,\ k_{n\perp}\ ,\ v_{\perp}\ ,\ trh\ ,\ trk\ ,\ a/\alpha_0\ ,\ \theta\ ,\ v_n)\ , \tag{3.102}$$

where the symbol $\perp$ replacing an index means the projection orthogonal to n_i, and we have used the shorthand

$$v_n = \frac{1}{2}\,(tr\,h - h_{nn}) - z_n\ . \tag{3.103}$$

The characteristic matrix of the Z4 evolution system is then given in this basis in the simple block-diagonal form

$$\mathbf{A} = \begin{pmatrix}
0 & 2\alpha_0 & & & & & & & & \\
\alpha_0/2 & 0 & & & & & & & & \\
 & & 0 & 2\alpha_0 & 0 & & & & & \\
 & & 0 & 0 & -\alpha_0 & & & & & \\
 & & 0 & -\alpha_0 & 0 & & & & & \\
 & & & & & 0 & 2\alpha_0 & 0 & & \\
 & & & & & 0 & 0 & \alpha_0 & 0 & -2\alpha_0 \\
 & & & & & 0 & f\alpha_0 & 0 & -mf\alpha_0 & 0 \\
 & & & & & & & & 0 & \alpha_0 \\
 & & & & & & & & \alpha_0 & 0
\end{pmatrix}\ . \tag{3.104}$$

A simple inspection of the this matrix shows that

- A new sector appears (**energy sector**) at the lower right corner, involving the pair of Fourier coefficients.

$$(\theta\ , v_n)\ . \tag{3.105}$$

  The corresponding eigenvalues are given by the background metric light speed $\pm\alpha_0$. There is a non-trivial coupling between the energy and the gauge sectors.
- The **eigenvalues** (propagation speeds) are either zero, or the background metric light speed, or the 'gauge speed' $\pm\sqrt{f}\,\alpha_0$. The requirement of real propagation speeds amounts again to the condition $f \geq 0$ on the gauge parameter f.
- A complete set of **eigenvectors** can be obtained in the generic case, with the only exceptions of geodesic slicing ($f = 0$), where gauge speed vanishes, and the standard harmonic case ($f = 1$), where gauge speed coincides with light speed. In both cases the extra degeneracy is a problem, although in the second one we can still put $\mathbf{A}$ in full diagonal form when $m = 2$.

We can conclude that the Z4 evolution system is strongly pseudo-hyperbolic for all the generalized harmonic slicing cases for which

$$f > 0\ , \qquad m = 2\ \ if\ \ f = 1\ , \tag{3.106}$$

so that we can confirm the relevance of the new gauge parameter m in the generalized harmonic condition (3.90).

3.4.4 Symmetry Breaking

We will address now the question of the relationship of the Z4 system with the precedent ones. To this end, let us consider the following recombination of the dynamical fields

$$\tilde{K}_{ij} \equiv K_{ij} - \frac{n}{2}\,\Theta\,\gamma_{ij} \tag{3.107}$$

so that the Z4 system (3.82–3.85) can be written in a one-parameter family of equivalent forms just by replacing everywhere

$$K_{ij} \rightarrow \tilde{K}_{ij} + \frac{n}{2}\,\Theta\,\gamma_{ij}\ . \tag{3.108}$$

This kind of transformations leave invariant the solution space of the system (it is actually the same system expressed in a different basis of dynamical fields).

But suppose now that we want to enforce the first algebraic constraint in (3.87), that is

$$\Theta = 0\ . \tag{3.109}$$

This amounts to suppress the Θ field as a dynamical quantity. If this suppression is made after the replacement (3.108), one gets a one-parameter family of non-equivalent extended systems with only the three components of the vector Z_i as supplementary quantities (Z3 evolution systems), namely:

$$(\partial_t - \mathcal{L}_\beta)\,\gamma_{ij} = -2\,\alpha\,K_{ij} \tag{3.110}$$

$$\begin{aligned}(\partial_t - \mathcal{L}_\beta)K_{ij} = &-\nabla_i\,\alpha_j + \alpha\,\Big[\,R_{ij} + \nabla_i Z_j + \nabla_j Z_i \\ &-2\,K_{ij}^2 + trK\,K_{ij} - S_{ij} + \frac{1}{2}\,(trS - \tau)\,\gamma_{ij}\,\Big] \\ &-\frac{n}{4}\,\alpha\,[\,tr\,R + 2\,\nabla_k Z^k + tr^2K - tr(K^2) \\ &-\,2\,Z^k\alpha_k/\alpha - 2\,\tau\,]\,\gamma_{ij}\end{aligned} \tag{3.111}$$

$$(\partial_t - \mathcal{L}_\beta)Z_i = \alpha\,[\nabla_j\,(K_i{}^j - \delta_i{}^j\ trK) - 2K_i{}^j Z_j - S_i] \tag{3.112}$$

where we have suppressed the tilde over K_{ij}, allowing for the vanishing of Θ.

The recombination symmetry (3.108) of the original Z4 system (3.82–3.85) is broken in the transition to the Z3 one (3.110–3.112), which is produced by the vanishing of the Θ parameter. This 'symmetry breaking' means that any two different choices of the n parameter in the family of Z3 evolution systems (3.110–3.112) are not mutually equivalent: their solution spaces are different, even at the linear order.

The Bona-Massó system [22, 23] can be easily recovered from the $n = 0$ case in (3.110–3.112). The extra quantities V_i can be obtained from the vector Z_i as follows

$$V_i = \frac{1}{2}\,\gamma^{\,rs}[\,\partial_i\,(\gamma_{rs}) - \partial_r\,(\gamma_{is})\,] - Z_i\ , \tag{3.113}$$

so that the evolution equation for V_i can be computed in an straightforward way. Notice that, contrary to what happened with V_i, the 'zero' vector Z_i behaves as a three-vector under general space coordinate transformations. This difference is clearly pointed out by the relationship (3.113) between these two quantities.

The BSSN system [24, 25] can also be recovered (not so easily) from the $n = 4/3$ case in (3.110–3.112). To do this, the Z3 system must be decomposed into trace and trace-free parts

$$e^{4\,\phi} = \gamma^{1/3}\ , \quad \tilde{\gamma}_{ij} = e^{-4\,\phi}\ \gamma_{ij} \tag{3.114}$$

$$K = \gamma^{ij}\ K_{ij}\ , \quad \tilde{A}_{ij} = e^{-4\,\phi}\ \left(K_{ij} - \frac{1}{3}\ K\ \gamma_{ij}\right) \tag{3.115}$$

$$\tilde{\Gamma}_i = -\tilde{\gamma}_{ik}\ \tilde{\gamma}^{kj}_{\ ,j} + 2\ Z_i \tag{3.116}$$

in order to follow the correspondence with BSSN more closely.

It must be pointed out, however, that one does not get in this way the original BSSN system: there is actually one difference in the lower order terms (only the principal parts are equivalent). The difference is in the term of the form

$$+\ \frac{n}{2}\ Z^k \alpha_k\ \gamma_{ij} \tag{3.117}$$

in the evolution equation (3.111), which is missing in the original BSSN system [25]. This lower order term is needed for consistency with the general covariant equations (3.78).

We have seen how both the Bona-Massó and BSSN systems can be obtained from the more general Z4 formalism. The equivalence transformation (3.107) plays the crucial role because suppressing the Θ field (3.109) produces a sort of symmetry breaking: different values of the parameter n will lead to evolution systems that can no longer be transformed one into another once the set of dynamical fields is reduced by the vanishing of Θ.

We will extend this idea to the remaining supplementary quantity Z_i in the next chapter. Let us just notice here that setting $Z_i = 0$ in the Z3 evolution system (3.110–3.112) leads to a one parameter family of non-equivalent free-evolution ADM systems. We can easily identify the $n = 0$ case as the 'Ricci evolution system' (2.59) and the $n = 1$ case as the 'Einstein evolution system' (2.62) that we introduced as separate options in the previous chapter.

4

First Order Hyperbolic Systems

From the mathematical point of view, the mixed-type systems (first order in time, second order in space) that we have considered in the previous chapter are associated to the parabolic type of equations. The prototype could be the Navier-Stokes equation of fluid dynamics, where second order space derivatives appear in the viscosity terms. Parabolic equations are not the ones usually associated with causal propagation phenomena, where a finite propagation speed can be derived in a natural way from the governing equations.

Causal propagation is more easily described instead by systems of equations of hyperbolic type. The prototype is either the (second order) wave equation, or the (first order) Euler equations of Fluid Dynamics, where viscosity terms are not taken into account. The fact that Computational Fluid Dynamics deals mainly with hyperbolic first order systems has stimulated the research on these systems, leading to interesting developments in Applied Mathematics, both at the theoretical and the computational level. In order to take advantage of these advanced developments, it is convenient to express the mixed-type Numerical Relativity systems in a purely first order form.

4.1 First Order Versions of Second Order Systems

4.1.1 Introducing Extra First Order Quantities

A first order version of the Z4 evolution system (3.82–3.85) can be obtained in the standard way by considering the first space derivatives

$$A_k \equiv \partial_k \, ln\alpha, \quad D_{kij} \equiv \frac{1}{2} \, \partial_k \gamma_{ij} \tag{4.1}$$

as independent dynamical quantities. This means that we must provide evolution equations for the new quantities (4.1).

C. Bona and C. Palenzuela Luque: *Elements of Numerical Relativity*, Lect. Notes Phys. **673**, 67–92 (2005)
www.springerlink.com

The standard way is just to realize that (4.1) are partial space derivatives of the metric coefficients, so that the time derivatives of (4.1) will be mixed second derivatives of these coefficients. By reversing the order of space and time derivatives, one gets

$$\partial_t A_k \; + \; \partial_k [\; \alpha \, Q \;] = 0 \; , \tag{4.2}$$

$$\partial_t D_{kij} \; + \; \partial_k [\; \alpha \, K_{ij} \;] = 0 \; , \tag{4.3}$$

where we have noted

$$Q \; \equiv -1/\alpha \, \partial_t \, ln\alpha \; , \tag{4.4}$$

which will of course depend of the time slicing condition. The choice (3.90) would correspond to

$$Q = f \, (tr \, K - m \, \Theta) \; . \tag{4.5}$$

Notice that the new quantities A_k behave like the components of a 3+1 vector under general coordinate transformation, but the components D_{kij} do not transform in a covariant way. We will consider in what follows the vanishing shift case for simplicity, so that the full set of dynamical fields can be given by

$$\mathbf{u} \; = \; \{\alpha, \; \gamma_{ij}, \; K_{ij}, \; A_k, \; D_{kij}, \; \Theta, \; Z_k\} \tag{4.6}$$

(38 independent fields). The missing shift terms in (4.2) and (4.5) can still be recovered by the standard replacement (2.50), but the shift terms in (4.3) must be obtained instead by a direct computation.

Notice also that the new quantities must be computed now through their evolution equations (4.2, 4.3). The original definitions (4.1) are now considered instead as constraints. These new first order constraints are, by construction, first integrals of the evolution equations, so that it is enough to enforce them on the initial data. It follows that the first order versions will have a larger set of constraints than the original second order systems. This is a complication, both from the theoretical and the computational point of view, as we will see in what follows.

4.1.2 Ordering Ambiguities

The first instance of such complication is the ordering ambiguities of second space derivatives. We can combine the space derivatives of the first constraint in (4.1) to get an ordering constraint for A_k, namely

$$0 \; = \; \partial_i \, A_j - \partial_j \, A_i \; . \tag{4.7}$$

The fact that the ordering constraint (4.7) does not hold identically produces an ordering ambiguity in the second derivatives of the lapse appearing in the evolution equation (3.83) for K_{ij}. This ambiguity can be easily solved by taking the symmetric combination

$$\nabla_i \, d_j \, \alpha \;=\; \frac{1}{2}[\nabla_i(\alpha \, A_j) + \nabla_j(\alpha \, A_i)] \;, \tag{4.8}$$

which is the only one that preserves the symmetric character of K_{ij}.

We can get in the same way an ordering constraint for D_{kij}, namely

$$0 \;=\; \partial_r \, D_{sij} - \partial_s \, D_{rij} \;. \tag{4.9}$$

As far as this ordering constraint does not hold identically, this produces again an ordering ambiguity in (3.83), where second space derivatives of the metric appear through the Ricci tensor R_{ij}.

But this time the ambiguity can not be resolved by invoking the symmetric character of K_{ij}. On one side, we can get the standard Ricci decomposition

$${}^{(+)}R_{ij} \;=\; \partial_k \, \Gamma^k{}_{ij} - \partial_i \, \Gamma^k{}_{kj} + \Gamma^r{}_{rk}\Gamma^k{}_{ij} - \Gamma^k{}_{ri}\Gamma^r{}_{kj} \;, \tag{4.10}$$

where Γ_{kij} stands now for

$$\Gamma_{kij} \;\equiv\; D_{ijk} + D_{jik} - D_{kij}. \tag{4.11}$$

On the other side, we can get the De Donder-Fock [20, 21] decomposition

$$\begin{aligned} {}^{(-)}R_{ij} = &-\partial_k \, D^k{}_{ij} + \partial_{(i} \, \Gamma_{j)k}{}^k - 2D_r{}^{rk} D_{kij} \\ &+ 4D^{rs}{}_i D_{rsj} - \Gamma_{irs}\Gamma_j{}^{rs} - \Gamma_{rij}\Gamma^{rk}{}_k \end{aligned} \tag{4.12}$$

which is most commonly used in Numerical Relativity codes because the second derivatives in (4.12) can be interpreted as (minus) the Laplace operator acting on the metric coefficients plus the symmetrized derivatives of some terms which can be easily related with the extra quantities of either the Bona-Massó or the BSSN systems.

There is no fundamental reason to prefer either the (4.10) or the (4.12) ordering. This is why we will consider an arbitrary combination of both cases, namely

$$R_{ij} \;=\; \frac{1+\zeta}{2} \; {}^{(+)}R_{ij} + \frac{1-\zeta}{2} \; {}^{(-)}R_{ij} \;, \tag{4.13}$$

where we have introduced the ordering parameter ζ so that the choice $\zeta = +1$ corresponds to the standard ordering (4.10), whereas the opposite choice $\zeta = -1$ corresponds to the alternative one (4.12). The intermediate value $\zeta = 0$ corresponds to the symmetrization of all second space derivatives.

4.1.3 The First Order Z4 System

Now we are in position to write down the first order version of the Z4 evolution system (3.82–3.85) (zero shift case)

$$\partial_t\ ln\alpha = -\alpha\, Q \tag{4.14}$$

$$\partial_t\ \gamma_{ij} = -2\,\alpha\, K_{ij} \tag{4.15}$$

$$\partial_t\ K_{ij} = -\nabla_i\alpha_j + \alpha\,\Big[\, R_{ij} + \nabla_i Z_j + \nabla_j Z_i \\ -2\,K^2_{ij} + (trK - 2\,\Theta)\,K_{ij} - S_{ij} + \frac{1}{2}\,(tr\,S - \tau)\,\gamma_{ij}\Big] \tag{4.16}$$

$$\partial_t A_k = -\partial_k[\ \alpha\, Q\ ] \tag{4.17}$$

$$\partial_t D_{kij} = -\partial_k[\ \alpha\, K_{ij}\ ] \tag{4.18}$$

$$\partial_t\ \Theta = \frac{\alpha}{2}\,[\,tr\,R + 2\,\nabla_k Z^k + (trK - 2\,\Theta)\,trK \\ -tr(K^2) - 2\,Z^k\alpha_k/\alpha - 2\tau] \tag{4.19}$$

$$\partial_t\ Z_i = \alpha\,[\nabla_j\,(K_i{}^j - \delta_i{}^j trK) + \partial_i\Theta \\ -2\,K_i{}^j\,Z_j - \Theta\,\alpha_i/\alpha - S_i]\ , \tag{4.20}$$

where the second derivative terms in (4.16) must be replaced by (4.8, 4.13) and the quantity Q in (4.14, 4.17) can be obtained from any algebraic condition of the form (4.5).

The propagation properties of a first order system like (4.14–4.20) are given by the principal part terms, that is the ones containing partial derivatives. It is then interesting for further purposes to write down the principal part of (4.14–4.20) in an explicit way

$$\partial_t\ \alpha = \dots \tag{4.21}$$

$$\partial_t\ \gamma_{ij} = \dots \tag{4.22}$$

$$\partial_t\Theta + \partial_k\ [\alpha\ (D^k - E^k - Z^k)] = \dots \tag{4.23}$$

$$\partial_t\ Z_i + \partial_k\ [\alpha\ (\delta^k_i(trK - \Theta) - K^k{}_i)] = \dots \tag{4.24}$$

$$\partial_t\ A_k + \partial_k\ [\alpha\ f\,(trK - m\,\Theta)] = \dots \tag{4.25}$$

$$\partial_t\ D_{kij} + \partial_k\ [\alpha\ K_{ij}] = \dots \tag{4.26}$$

$$\partial_t\ K_{ij} + \partial_k\ [\alpha\ \lambda^k_{ij}] = \dots \tag{4.27}$$

where the dots stand for terms not containing derivatives and we have noted for short

$$D_i \equiv D_{ik}{}^k\ , \qquad E_i \equiv D_{ki}{}^k\ , \tag{4.28}$$

$$\lambda^k_{ij} \equiv D^k{}_{ij} + \frac{1}{2}\,\delta^k_i(A_j + D_j - 2E_j - 2Z_j) + \frac{1}{2}\,\delta^k_j(A_i + D_i - 2E_i - 2Z_i) \\ -\frac{1+\zeta}{2}\,(D_{ij}{}^k + D_{ji}{}^k - \delta^k_i E_j - \delta^k_j E_i)\ . \tag{4.29}$$

Notice that there is no ordering ambiguity in the evolution equation (4.23) for Θ. This is because the trace of the ζ-dependent terms in (4.29) vanishes identically. One has the full set of 38 evolution equations for the 38 fields in (4.6), containing only f and m as gauge parameters and ζ as ordering parameter.

4.1.4 Symmetry Breaking: The KST System

We have obtained in the previous sections the first order version (4.14–4.20) of the Z4 system by assuming the standard evolution equations (4.17–4.18) for the first order quantities (4.1). But this is not the only way of getting a first order version of a second order system. Kidder, Scheel and Teukolsky obtained a first order version of the original ADM system by combining the energy and momentum constrains with the first order evolution equations (KST system [31]).

The original KST system assumed a direct power-law relationship between the lapse and the space volume element ('densitized' lapse). This original system has been generalized by Sarbach and Tiglio [32] in order to include the wide class of generalized harmonic conditions that we are considering here, in which the lapse is an independent quantity which must be computed from its evolution equation ('dynamical' lapse). In what follows we will use the term 'KST system' to refer also to this generalization.

We will recover here the KST system from the Z4 one by a symmetry breaking mechanism, along the lines sketched in Sect. 3.4.4. Let us consider as a starting point the principal part (4.21–4.27). We will follow a two-step 'symmetry breaking' process, namely

1. Recombine the dynamical fields K_{ij}, D_{kij} with Θ and Z_i in a linear way,

$$\tilde{K}_{ij} = K_{ij} - \frac{n}{2}\,\Theta\,\gamma_{ij}\ , \tag{4.30}$$

$$d_{kij} = 2\,D_{kij} + \eta\,\gamma_{k(i}Z_{j)} + \chi\,Z_k\,\gamma_{ij}\ , \tag{4.31}$$

   where we have used the notation of [31], replacing only their parameter γ by $-n/2$ for consistency with the definition (3.107) in Sect. 3.4.4. Notice that the linear combinations (4.30–4.31) are generic in the sense that they are the most general linear combinations that preserve the tensor character of the dynamical fields under linear coordinate transformations (remember that the D's components are not covariant under general coordinate transformations).
2. Suppress both θ and Z_i as dynamical fields, namely

$$\Theta = 0\ , \qquad Z_i = 0\ . \tag{4.32}$$

   In that way, the principal part (4.22–4.27) becomes

$$\partial_t\ \alpha = \ldots \tag{4.33}$$

$$\partial_t\ \gamma_{ij} = \ldots \tag{4.34}$$

$$\partial_t\ A_k + \partial_k\ [\ \alpha\ f\ tr\,\tilde{K}\ ]\ =\ 0 \tag{4.35}$$

$$\begin{aligned}\partial_t\ d_{kij} + \partial_r[\ \alpha\,\{\,2\,\delta^r_k\,\tilde{K}_{ij} - \chi\,(\tilde{K}^r_k - \delta^r_k\,tr\,\tilde{K})\,\gamma_{ij} \\ + \eta\,\gamma_{k(i}(\tilde{K}^r{}_{j)} - \delta^r{}_{j)}tr\,\tilde{K})\}\ ] = \ldots\end{aligned} \tag{4.36}$$

$$\partial_t\ \tilde{K}_{ij} + \partial_k\ [\ \alpha\ \lambda^k_{ij}\ ] = \ldots \tag{4.37}$$

for the reduced set of 34 dynamical fields

$$\mathbf{u} \;=\; \{\alpha,\; \gamma_{ij},\; \tilde{K}_{ij},\; A_k,\; d_{kij}\}\;, \tag{4.38}$$

where λ^k_{ij} stands now for

$$\begin{aligned} 2\,\lambda^k{}_{ij} &= d^k{}_{ij} - \frac{n}{4}\,(d_{kr}{}^r - d_r{}^{rk})\,\gamma_{ij} \\ &+ \frac{1+\zeta}{2}\,(d_{ij}{}^k + d_{ji}{}^k) - \frac{1-\zeta}{2}\,(\delta^k_i\,d_{rj}{}^r + \delta^k_j\,d_{ri}{}^r) \\ &+ \delta^k_j\left(A_i + \frac{1}{2}\,d_{ir}{}^r\right) + \delta^k_i\left(A_j + \frac{1}{2}\,d_{jr}{}^r\right)\;. \end{aligned} \tag{4.39}$$

This provides the 'dynamical lapse' version [32] of the KST evolution system. In order to recover the original 'densitized lapse' version, one must in addition integrate explicitly the dynamical relationship (4.5) between the lapse and the volume element (remember that now $\Theta = 0$). It can be easily done in the case

$$f \;=\; 2\,\sigma \;=\; \text{constant}\;, \tag{4.40}$$

namely

$$\partial_t(\alpha\gamma^{-\sigma}) = 0\;, \tag{4.41}$$

so that the value of α can be defined in terms of γ for every initial condition. The same thing can be done with their space derivatives, so that we can take

$$A_i \;\equiv\; \sigma\,d_{ir}{}^r\;, \tag{4.42}$$

so that the set of dynamical fields is then further reduced to

$$\mathbf{u} \;=\; \{\gamma_{ij},\; K_{ij},\; d_{kij}\}\;. \tag{4.43}$$

The principal part of the evolution system is then given by (we suppress the tildes over the K_{ij})

$$\partial_t\;\gamma_{ij} = \ldots \tag{4.44}$$

$$\begin{aligned} \partial_t\;d_{kij} &+ \partial_r[\alpha\{\,2\,\delta^r_k\,K_{ij} - \chi\,(K_k{}^r - \delta^r_k\,tr\,K)\,\gamma_{ij} \\ &+ \eta\,\gamma_{k(i}(K^r{}_{j)} - \delta^r_{j)}tr\,K)\,\}] = \ldots \end{aligned} \tag{4.45}$$

$$\partial_t\;K_{ij} + \partial_k\;[\alpha\;\lambda^k_{ij}] = \ldots \tag{4.46}$$

$$\begin{aligned} 2\,\lambda^k{}_{ij} &= d^k{}_{ij} - \frac{n}{4}\,(d_{kr}{}^r - d_r{}^{rk})\,\gamma_{ij} \\ &- \frac{1-\zeta}{2}\,(\delta^k_i\,d^r{}_{rj} + \delta^k_j\,d^r{}_{ri}) + \frac{1+\zeta}{2}\,(d_{ij}{}^k + d_{ji}{}^k) \\ &+ \frac{1+2\sigma}{2}\,(\delta^k_i\,d_{jr}{}^r + \delta^k_j\,d_{ir}{}^r) \end{aligned} \tag{4.47}$$

which corresponds precisely to (the principal part of) the original KST system [31].

Notice that we have lost in the process the second gauge parameter m, and the first one f has been replaced by σ. On the other hand, we have kept the ordering parameter ζ and we have got one extra energy constraint parameter n and two extra momentum constraint parameters χ and η.

4.2 Systems of Balance Laws

We have seen in Sect. 1.2.3 how Einstein's Field Equations can be interpreted as a system of balance laws. In the previous sections, we have written the evolution equations in first order form, like the ones appearing in the Fluid Dynamics domain. Now we are in position to take full advantage of this analogy, both from the theoretical and from the practical point of view. As anticipated, this will open the door to the application of the powerful methods and tools from Computational Fluid Dynamics into Numerical Relativity.

4.2.1 Fluxes and Sources

The principal part of the first order Z4 system (4.21–4.27) is in Flux-conservative form. The same is true for the KST systems (4.33–4.37) and (4.44–4.46). This means that the time evolution of the array $\mathbf{u}$ of dynamical fields can be written in the form

$$\partial_t \, \mathbf{u} + \partial_k \, \mathbf{F}^k = \dots \, , \tag{4.48}$$

where the Flux terms $\mathbf{F}^k$ depend algebraically on the fields, but not on their derivatives:

$$\mathbf{F}^k = \mathbf{F}^k(\mathbf{u}, x^j) \, . \tag{4.49}$$

If one takes into account the full system, not just the principal part, one gets the full balance-law form:

$$\partial_t \, \mathbf{u} + \partial_k \, \mathbf{F}^k = \mathbf{S} \, , \tag{4.50}$$

where the Source terms $\mathbf{S}$ do not contain any derivative,

$$\mathbf{S} = \mathbf{S}(\mathbf{u}, x^j) \, , \tag{4.51}$$

so that they do not contribute to the principal part.

The terms 'Fluxes' and 'Sources' come from the hydrodynamical analogous of the system (4.50). We can integrate term by term the differential system (4.50) over a given domain V in coordinate space in order to get the integral form of the balance law:

$$\partial_t \left[\int \mathbf{u} \, dV \right] + \oint \mathbf{F}^k \, dS_k = \int \mathbf{S} \, dV \, , \tag{4.52}$$

where we have applied Gauss theorem and S_k stands for the boundary surface element along the coordinate direction x^k. The hydrodynamical analogy suggests to interpret $\mathbf{u}$ as a sort of density so that the rate of change of the integrated quantity $\bar{\mathbf{u}}$ defined as

$$\bar{\mathbf{u}} \equiv \int \mathbf{u}\, dV \tag{4.53}$$

depends on the integrated effect of the sources inside V

$$\bar{\mathbf{S}} \equiv \int \mathbf{S}\, dV \tag{4.54}$$

and on the fluxes across every boundary S_k of V, namely

$$\oint \mathbf{F}^k\, dS_k\ . \tag{4.55}$$

4.2.2 Flux-Conservative Space Discretization

The balance law form (4.50) is specially suited for the MoL discretization, as described in Sect. 3.2.1. This is because in the method of lines there is a clear-cut separation between space and time discretization. As a consequence, the source terms contribute in a trivial way to the space discretization, as described in Sect. 3.2.2. The non-trivial contribution comes just from the Flux-conservative part (4.48).

The integral version (4.52) provides then a useful way of getting a finite elements discretization of the first order system (4.50). The space discretization can be obtained directly from:

$$\partial_t\ \bar{\mathbf{u}} + \oint \mathbf{F}^k\, dS_k = \bar{\mathbf{S}}\ , \tag{4.56}$$

so that the evaluation of partial space derivatives has been replaced by that of surface integrals of the flux terms.

The finite elements grid can be obtained as the dual of the finite differences grid, so that the elementary cells are centered on every grid node and their interfaces correspond to the intermediate points between neighbor nodes, as it is displayed in Fig. 4.1 (only two space dimensions are shown for clarity).

Alternatively, a finite differences discretization can be directly obtained from the differential version (4.50), namely

$$\begin{aligned}\mathbf{u}^{n+1} = \mathbf{u}^n &- \frac{\Delta t}{\Delta x}\left[\mathbf{F}^x_{i+1/2} - \mathbf{F}^x_{i-1/2}\right] - \frac{\Delta t}{\Delta y}\left[\mathbf{F}^y_{j+1/2} - \mathbf{F}^y_{j-1/2}\right] \\ &- \frac{\Delta t}{\Delta z}\left[\mathbf{F}^z_{k+1/2} - \mathbf{F}^z_{k-1/2}\right] + \Delta t\ \mathbf{S}\ .\end{aligned} \tag{4.57}$$

Every way of computing the interface Fluxes in terms of the values of the fields at the grid nodes will the lead to a specific numerical algorithm.

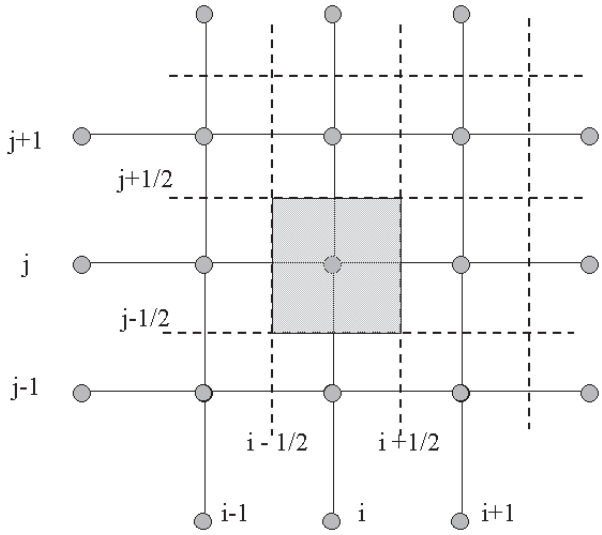

Fig. 4.1. The finite elements grid (*dotted lines*) consists in an array of elementary cells, which can be interpreted as the dual of the finite differences grid (*solid lines*). The prototype elementary cell, shown as the *dark rectangle*, is centered around its corresponding node, shown here as a *small circle*. It provides the region where the balance is to be computed. The Flux terms are evaluated at the interfaces, which are placed halfway between neighbor nodes

Let us consider for instance the scalar advection equation

$$\partial_t \; u + \partial_k \; [\lambda^k \; u] = 0 \; , \tag{4.58}$$

which describes propagation of the scalar field u with speed

$$v^k = \lambda^k \; . \tag{4.59}$$

One can compute the Flux at a given interface just by taking the value of the quantity u at the 'upwind' node, namely

$$F^x_{i+1/2} \;\; = \;\; \begin{array}{ll} \lambda^x \; u_i & (\lambda^x > 0) \\ \lambda^x \; u_{i+1} & (\lambda^x < 0) \end{array} \tag{4.60}$$

and the same way for the other directions. The resulting scheme is known as the first-order upwind discretization method.

One can wonder why a first order method can be obtained by just taking a zero order approximation, like (4.60), to the interface fluxes. This is a generic feature of the flux-conservative discretization (4.57). As far as the fluxes appear in (4.57) only through differences at neighboring interfaces, the leading errors at every interface cancel each other and one gets one extra order of accuracy (when dealing with smooth solutions). In this way, a second-order-accurate algorithm is obtained by using a first order average for the interface fluxes, namely

$$F^x_{i+1/2} \;=\; (F^x_i + F^x_{i+1})/2\;, \tag{4.61}$$

and the same way for the remaining directions.

Quite surprisingly, the simple average prescription (4.61) will be enough for most Numerical Relativity applications. We just need to use it in the Flux-conservative space discretization (4.57), which in turn provides the basic Euler step for the MoL time discretization, as described in Sect. 3.2.1. Our default choice of a finite difference algorithm will be then a combination of the third-order Runge-Kutta algorithm (3.44) for the time discretization and the second-order flux-conservative space discretization arising from the prescription (4.61). This is how the numerical results for the first order formalisms, as shown in Figs. 3.3 and 3.4, were obtained.

4.2.3 Weak Solutions

These order-of-accuracy considerations apply only to smooth solutions of Einstein's field equations. As stated in Sect. (1.2.3), there are also composite solutions in which the metric coefficients can have piecewise continuous first derivatives. In first order systems, these first derivatives are included in the array $\mathbf{u}$ of basic dynamical quantities (4.6). This means that the partial derivatives in the differential version (4.50) of the evolution system are not well defined.

To remedy this, one can complete the integration process leading from (4.50) to (4.56) by integrating also in time, that is

$$\bar{\mathbf{u}}(\Delta t) - \bar{\mathbf{u}}(0) + \oint \bar{\mathbf{F}}^k \; dS_k = \int_0^{\Delta t} \bar{\mathbf{S}} \; dt\;, \tag{4.62}$$

where we have noted

$$\bar{\mathbf{F}}^k = \int_0^{\Delta t} \mathbf{F}^k \; dt\;, \tag{4.63}$$

so that no partial derivative appears in this integral version of the evolution system. Every solution of the differential version (4.50) is a smooth solution of the integral version (4.62). Conversely, there are solutions of the integral version (4.62) (weak solutions) which are not smooth.

The differential version (4.50) does not hold for weak solutions, unless we interpret it in terms of distributions, as discussed in Sect. 1.2.3. In this case, the piecewise continuous first derivatives can be described by using step functions on the surface of discontinuity. Derivatives across this surface, like the ones appearing on the left-hand-side of (4.50), lead to singular Dirac-delta terms in the equations. Cancellation of these singular terms will fix the propagation speeds of the discontinuities wavefronts, as anticipated in Sect. 1.2.3.

We will go here one step further, by computing explicitly these propagation speeds. We will consider then a piecewise continuous solution in which the

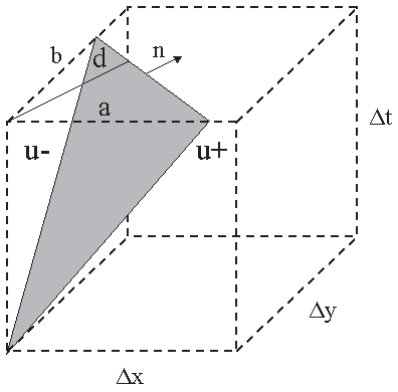

Fig. 4.2. An elementary cell is built in order to analyze the propagation of a discontinuity wavefront, which is entering by the lower left corner and propagating along the direction $\boldsymbol{n}$ (only two space dimensions are shown for clarity). The displacements of the discontinuity points along the x and y axes are labelled by a and b, respectively, whereas the wavefront displacement is labelled by d. The dynamical fields are supposed to be piecewise constant, with values u_+ and u_- ahead and behind the wavefront, respectively

first derivatives are discontinuous across a wavefront surface propagating with coordinate speed v (see Fig. 4.2 for details). As far as we are interested only in the singular terms, we will make the following simplifications:

- The metric coefficients are supposed to be continuous.
- The Source terms will be ignored, because they contain at most piecewise continuous contributions, but no Dirac-delta singularities.
- The remaining dynamical fields in (4.6), corresponding to metric first derivatives, will be taken to be piecewise constant. The values ahead the wavefront are noted u_+, whereas the values behind it will be noted u_-.

This model problem is the General Relativistic analogous of the well known Riemann problem in Fluid Dynamics [33].

With these simplifying assumptions, we can easily evaluate the integral balance law (4.62) for the elementary cell shown in Fig. 4.2:

- For the density terms, we have

$$\bar{\mathbf{u}}(\Delta t) - \bar{\mathbf{u}}(0) = -\frac{a\,b}{2}\,(\mathbf{u}_+ - \mathbf{u}_-)\,. \tag{4.64}$$

- The Flux terms balance gives in turn (two directions only)

$$\oint \bar{\mathbf{F}}^k\, dS_k = \frac{\Delta t}{2}\,[b\,(\mathbf{F}^x_+ - \mathbf{F}^x_-) + a\,(\mathbf{F}^y_+ - \mathbf{F}^y_-)]\,. \tag{4.65}$$

- The final balance can be written then

$$\frac{d}{a}\left(\mathbf{F}^x_+ - \mathbf{F}^x_-\right) + \frac{d}{b}\left(\mathbf{F}^y_+ - \mathbf{F}^y_-\right) = v\ \left(\mathbf{u}_+ - \mathbf{u}_-\right) \tag{4.66}$$

where $v = d/\Delta t$ is the wavefront propagation speed.

It is easy to see from Fig. 4.2 that the coefficients in the left-hand-side of (4.66) are precisely the components of the unit normal $\boldsymbol{n}$ to the wavefront. This means that we can put our final balance into its final form, valid for the generic three-dimensional case:

$$n_k\left(\mathbf{F}^k_+ - \mathbf{F}^k_-\right) = v\ \left(\mathbf{u}_+ - \mathbf{u}_-\right)\ . \tag{4.67}$$

These jump conditions are the General Relativistic analogous of the well-known Rankine-Hugoniot conditions of Fluid Dynamics [33]. These equations govern the propagation of shocks or any other kind of discontinuities across the fluid. In the General Relativity case, they provide in addition matching conditions for composite metrics.

Also, Einstein's field equations are quasilinear. This means that we can express the Flux terms in the form

$$\mathbf{F}^k = \mathbf{A}^k\ \mathbf{u}\ , \tag{4.68}$$

where the matrices $\mathbf{A}^k$ are continuous across the wavefronts because they depend on the metric coefficients, but not on their derivatives. Therefore, the jump conditions (4.67) can be written as a linear eigenvalue problem, namely

$$\left(\mathbf{A}^n - v\,\mathbf{I}\right)\ \left(\mathbf{u}_+ - \mathbf{u}_-\right) = 0\ , \tag{4.69}$$

where the matrix $\mathbf{A}^n = n_k\mathbf{A}^k$ is the characteristic matrix along the direction $\boldsymbol{n}$. The eigenvectors of the characteristic matrix correspond to combinations of the dynamical fields that may have discontinuity surfaces with normal $\boldsymbol{n}$. The corresponding eigenvalues (characteristic speeds) provide the physical propagation speeds for these discontinuity fronts.

This simple behavior in the General Relativity case is due to the quasilinear form (4.68) of the Fluxes. In Fluid Dynamics, instead, one can compute the characteristic speeds (like sound speed) by using the methods of the next section, but one still needs to solve the non-linear Rankine-Hugoniot equations (4.67) in order to compute the physical shock propagation speeds, which do not coincide with characteristic speeds: one can easily get supersonic shocks, for instance.

4.3 Hyperbolic Systems

We have seen yet two independent methods of studying the propagation properties of the field equations:

- The plane-wave analysis (see Sect. 3.1.3). It is valid only for smooth solutions. As far as it is based on the underlying physics, it gives consistent results independently of the way we manage to write down the equations.
- The jump conditions (4.67). It is valid only for non-smooth solutions, containing shocks or discontinuities. It assumes that the evolution system is of first order and has the balance-law structure.

Now we will see still another method: the hyperbolicity analysis, which is currently used in the mathematical literature for first order systems [14]. It is worth to note that the quasilinear nature of Einstein's Field Equations leads to a full coincidence of the results obtained by any of these three methods for the first order version of the equations, where all of them can be applied independently.

4.3.1 Weak and Strong Hyperbolicity

Hyperbolic first order systems have been proposed for Numerical Relativity applications since the seminal work of Y. Choquet-Bruhat and T. Ruggeri [37]. In all of them, the original ADM system [6] is modified by using the constraints in one or another way [22,23,31,32,38,39,40,41,42,43], even taking additional derivatives [37, 44, 45] (but see [46, 47] for a completely different approach).

We will consider a generic first order system, although the specific developments will be carried out for the first order version (4.14–4.20) of the Z4 system [30]. For the purposes of our analysis, we will need to deal only with the principal part, that is the one containing first derivatives of the basic fields $\mathbf{u}$. In our case, this means that the Source terms can be ignored. For the sake of generality, we will not assume here that the principal part is in Flux-conservative form, so that we will start from

$$\partial_t \ \mathbf{u} + \mathbf{A}^k \ \partial_k \ \mathbf{u} = 0 \ , \tag{4.70}$$

which can also be interpreted as a linearized version of (4.48), where the matrices $\mathbf{A}^k$ are given by

$$\mathbf{A}^k = \frac{\partial \mathbf{F}^k}{\partial \mathbf{u}} \ . \tag{4.71}$$

Let us consider now a generic space direction $\boldsymbol{n}$. We will study the following eigenvalue problem

$$(\mathbf{A}^n - v \ \mathbf{I}) \ \mathbf{u} = 0 \tag{4.72}$$

which is the equivalent for smooth solutions of the linearized version (4.69) of the jump conditions (4.67). The matrix $\mathbf{A}^n = n_k \mathbf{A}^k$ will be called again the characteristic matrix along the direction $\boldsymbol{n}$. Their eigenvalues v will be the corresponding characteristic speeds.

We will say that the first order system (4.70) is

- **Strongly hyperbolic** if, for every direction $\boldsymbol{n}$, all the characteristic speeds are real and the characteristic matrix can be put into full diagonal form (there is a complete set of eigenvectors).
- **Weakly hyperbolic** if, for every direction $\boldsymbol{n}$, all the characteristic speeds are real but, at least for some direction, the characteristic matrix can not be fully diagonalized.

These definitions coincide with the strong and weak Pseudo-hyperbolicity, respectively, that were introduced in Sect. 3.1.3, when applied to the homogeneous first order system (4.70).

Hyperbolic systems can be shown, with some additional smoothness assumptions [14], to have a well-posed initial-value problem. This implies the stability of the solutions at the continuum level, which is a necessary condition for the stability of numerical solutions. We have seen in Sect. 3.2 that strong hyperbolicity is actually required to get stability at the numerical level. We will see in the following section how a complete set of eigenvectors is mandatory in order to apply advanced numerical methods from Computational Fluid Dynamics.

Before going further in that direction, let us solve the eigenvalue problem for the first order version (4.14–4.20) of the Z4 system. Let us notice first that the principal terms of the evolution equations (4.21–4.22) for the metric coefficients are trivial, so that we can restrict ourselves to the reduced set of 31 dynamical fields

$$\mathbf{u} \;=\; \{K_{ij},\; A_k,\; D_{kij},\; \Theta,\; Z_k\}\;, \tag{4.73}$$

which are supposed to evolve in the non-homogeneous background provided by the metric coefficients $\alpha,\ \gamma_{ij}$. Let us also introduce the first order version of the quantity (3.113)

$$V_k = D_k - E_k - Z_k\;, \tag{4.74}$$

as an auxiliary variable which will prove very useful for the analysis.

The spectral decomposition of the characteristic matrix $\mathbf{A}^n$ provides the following list of eigenfields:

- **Standing eigenfields** (zero characteristic speed)

$$A_\perp,\ D_{\perp ij},\ A_k - fD_k + f\,mV_k \tag{4.75}$$

  (17 independent fields), where the symbol $\perp$ replacing an index means the projection orthogonal to n_i, for instance

$$D_{\perp ij} \equiv (\delta_k{}^r - n_k n^r) D_{rij}\;. \tag{4.76}$$

- **Light-cone eigenfields** (local characteristic speed $\pm\alpha$)

$$L_{ij}^{\pm} \equiv [K_{ij} - n_i n_j \; tr\, K] \pm [\lambda^n{}_{ij} - n_i n_j \; tr\, \lambda^n] \tag{4.77}$$

$$E^{\pm} \equiv \theta \pm V^n \tag{4.78}$$

(12 independent fields), where the symbol n replacing the index means the contraction with n_i, for instance

$$\lambda^n_{ij} \;\equiv\; n_k \lambda^k_{ij} \; . \tag{4.79}$$

- **Gauge eigenfields** (characteristic speed $\pm\alpha\sqrt{f}$). In the generic, non-degenerate, case ($f \neq 1$), we get

$$G^{\pm} \equiv \sqrt{f}\,[\; tr\, K - \mu\; \Theta \;] \pm [\; A^n + (2-\mu)\; V^n \;] \; , \tag{4.80}$$

where we have written for short

$$\mu = \frac{f\, m - 2}{f - 1} \; . \tag{4.81}$$

In the degenerate case $f = 1$, one must have $m = 2$, as discussed below, and the extra degeneracy allows any value of the combination (4.81). The corresponding eigenfields can be chosen to be, for instance,

$$[\; tr\, K \;] \pm [\; A^n + 2\; V^n \;] \; . \tag{4.82}$$

From the list (4.75–4.80) of eigenvectors and their corresponding eigenvalues, we can easily conclude that

- All the characteristic speeds are real (the system is at least weakly hyperbolic) if and only if $f \geq 0$.
- In the case $f = 0$, the two components of the gauge pair $G^{\pm}$ are not independent, so that the total number of independent eigenfields is 30 instead of the 31 ones required for strong hyperbolicity.
- The case f=1 (harmonic case) is special:
  - if $m \neq 2$, then the gauge pair $G^{\pm}$ can not be fully decoupled from the pair $E^{\pm}$, so that one has only 29 independent eigenfields
  - if $m = 2$, then these pairs can be decoupled in many ways, due to the degeneracy of the gauge and light eigenfields. The pair (4.82) is just one of such choices. One recovers then the full set of 31 independent eigenfields (strong hyperbolicity).
- The first order Z4 system described by (4.14–4.20) is strongly hyperbolic in all the remaining cases ($f > 0$, $f \neq 1$).

The same conclusions apply to the case of a kinematical shift, given independently of the dynamical fields (4.73). The main change is that the characteristic speeds are 'drifted' by a shift term:

$$v^n = (-\beta^n \; , \;\; -\beta^n \pm \alpha \; , \;\; -\beta^n \pm \alpha\sqrt{f}) \; . \tag{4.83}$$

Notice that the use of a superluminal shift can reverse the sign of some characteristic speeds. In the Fluid Dynamics language, these would be 'sonic points' and they will deserve a special treatment in numerical applications.

4.3.2 High-Resolution Shock-Capturing Numerical Methods

We will see now how to take advantage of the strongly hyperbolic nature of the evolution system in order to apply advanced numerical methods, like the ones currently used in Computational Fluid Dynamics.

Let us start from the Flux-conservative discretization (4.57). The interface Fluxes $\mathbf{F}_{i\pm1/2}$ must be computed for every elementary cell (we will consider for the moment only one space direction). The idea is to 'reconstruct' the field values in a consistent way inside the elementary cell, so that one can get $\mathbf{u}_{i\pm1/2}$ and, then, compute the interface Fluxes. For a quasilinear system, this is equivalent to the alternative strategy of computing first the Fluxes at the grid nodes $\mathbf{F}_i$ and then reconstructing the Fluxes at the interfaces (this is what we actually recommend in practical applications).

We show in Fig. 4.3 two different cell reconstructions. Notice that a discontinuity appears at every interface, where the values $\mathbf{u}_-$ are obtained from the previous cell and the values $\mathbf{u}_+$ are obtained instead from the next cell. To be more specific, at the $i+1/2$ interface one gets

$$\mathbf{u}_- = \mathbf{u}_i \qquad \mathbf{u}_+ = \mathbf{u}_{i+1} \tag{4.84}$$

for the zero order reconstruction (first panel in Fig. 4.3), or

$$\mathbf{u}_- = \mathbf{u}_i + \frac{1}{4}\,(\mathbf{u}_{i+1} - \mathbf{u}_{i-1}) \tag{4.85}$$

$$\mathbf{u}_+ = \mathbf{u}_{i+1} - \frac{1}{4}\,(\mathbf{u}_{i+2} - \mathbf{u}_i) \tag{4.86}$$

for the linear reconstruction (second panel in Fig. 4.3).

There are two different ways of dealing with such interface discontinuities. The first one, valid for smooth solutions, is to interpret this discrepancy between the left-hand-side and the right-hand-side interface values just as a consequence of the finite difference discretization. The right strategy in this case would be to improve the accuracy at the interface by taking the average, that is

$$\mathbf{u}_{i+1/2} = (\mathbf{u}_+ + \mathbf{u}_-)/2 \tag{4.87}$$

and then compute the interface Fluxes. In this sense, the simple average (4.61) can be regarded as the result of applying the lowest level reconstruction (4.84) directly to the Fluxes and then averaging at the interfaces.

The second way of dealing with the numerical discontinuities at the interface is to interpret $(\mathbf{u}_-,\ \mathbf{u}_+)$ as initial data for a Riemann problem. In this way, we allow for the possibility that some interface discrepancies arise from real discontinuities, not just from discretization artifacts. Getting the Fluxes at a given interface would amount then to solving the Riemann problem there, so that one gets the physical solution even if a shock or any other kind of discontinuity is crossing through the elementary cell ('Shock- capturing methods').

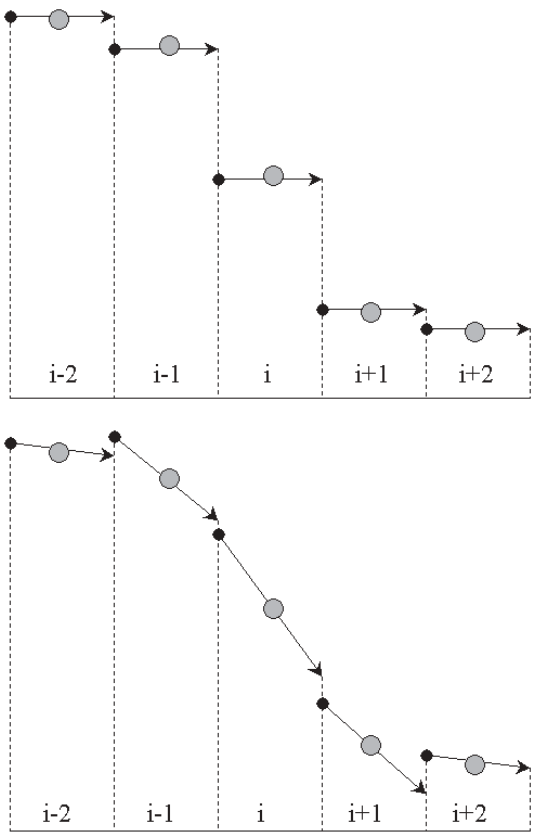

Fig. 4.3. Starting from the values of the dynamical fields (alternatively, the fluxes) at the grid nodes, two different reconstructions are shown inside every elementary cell: the flat one (*first panel*) and a linear one (*second panel*). In both cases, numerical discontinuities appear at every interface (*dotted lines*) between the *left* and *right* values (*arrows* and *dots*, respectively). Notice that the original function was monotonically decreasing: all the slopes are negative. This monotonicity is preserved either by the left interface values (*arrows*) or by the right interface values (*dots*) in the flat reconstruction case. In the linear reconstruction case, however, both the left interface values (at $i - 3/2$) and the right interface ones (at $i + 3/2$) show local extreme values that break the monotonicity of the original function

There are many 'Riemann solver' numerical algorithms, which are currently used in Fluid Dynamics [34]. The General Relativity case, however, is quasilinear so that most of these algorithms give equivalent results. We prefer to use the a simplified version of the one given by Marquina [35]. The prescription for getting the interface values $\mathbf{u}_{i+1/2}$ can be stated as follows:

- Decompose both one-sided predictions ($\mathbf{u}_-$, $\mathbf{u}_+$) as linear combinations of the set of characteristic fields $\mathbf{w}$. Note that the coefficients in these

combinations are not necessarily constant: we must use in general a different set of values on each side of the interface.

- Project the forward prediction $\mathbf{u}_-$, by suppressing any components corresponding to negative characteristic speeds (forward projection $\mathbf{u}^F$).
- Project the backward prediction $\mathbf{u}_+$, by suppressing any components corresponding to positive characteristic speeds (backward projection $\mathbf{u}^B$).
- Add these upwind-projected values at the given interface, that is

$$\mathbf{u}_{i+1/2} \;=\; \mathbf{u}^F + \mathbf{u}^B \;. \tag{4.88}$$

There is no mistake: this is not an average, like in (4.61). One is taking instead the positive speed components from the previous cell and the negative speed components from the next one (note that static characteristic fields, with $v^n = 0$, do not contribute to the Fluxes in the quasilinear case). Notice also that we must assume for consistency a definite sign for the characteristic speed. If v^n changes its sign between both sides of the given interface (a 'sonic' point), then a specific combination must be taken instead of the upwind projections presented here. (see [35] for the details).

The interface Fluxes can then be easily computed from (4.88). Alternatively, if we are reconstructing the Fluxes, the starting point will be the one-sided predictions ($\mathbf{F}_-$, $\mathbf{F}_+$), and the same procedure will apply (a little bit simpler, because static characteristic fields have no Flux, so that they not even appear in the process). The power of the upwind algorithm (4.88) comes from the fact that one is using just the sign of the characteristic speeds, not their values (except at sonic points). This is very helpful in the case of oblique wavefronts (see Fig. 4.2), where the parallax effect causes the discontinuities to propagate along the coordinate axes faster than the corresponding characteristic speeds (notice that both a and b are greater than d in Fig. 4.2). As far as the propagation direction is not reversed by the parallax effect, using just the signs of the characteristic speeds provides a robust algorithm even in the case of oblique shocks, as we will show below.

The combination of the upwind algorithm (4.88) with the zero-order 'flat' reconstruction of the interface values (first panel in Fig. 4.3) is equivalent to the first order upwind method (4.60) that we presented when discussing the advection equation. This is because every eigenfield of the characteristic matrix obeys actually an advection equation along the selected space direction: the propagation speed is precisely the corresponding eigenvalue of the characteristic matrix. Notice, however, that using the upwind algorithm (4.88) instead of the standard average (4.61) downgrades the accuracy from second to first order. This leads to poor numerical results when applied to the modest-size three-dimensional grids that are currently used in Numerical Relativity, as we will see below.

A High-resolution Shock-capturing method can be built instead by combining the upwind algorithm (4.88) with a first order reconstruction of the interface values, like the one presented in (4.85), which will ensure second-order spatial accuracy. There is a price to pay for this: as we can see in

the second panel in Fig. 4.3, the linear reconstruction does not preserve the monotonicity of the dynamical fields. This will cause spurious oscillations in the numerical results, as we will see below.

Notice that this monotonicity breaking can occur only when the centered slope Δ^C that is being used for the reconstruction of a given field u (alternatively, its corresponding flux F) gets at least twice as large as any of the left or right-sided slopes:

$$\Delta_i^L \equiv (u_i - u_{i-1}) \,, \qquad \Delta_i^R \equiv (u_{i+1} - u_i) \tag{4.89}$$

(see Fig. 4.3). Otherwise, the predictions at a given interface are always bounded between the neighbor node values so that monotonicity of the node values would imply that of the interface ones. In our case, we have chosen the average

$$\Delta_i^C \equiv (\Delta_i^L + \Delta_i^R)/2 = (u_{i+1} - u_{i-1})/2 \,, \tag{4.90}$$

and a simple calculation shows that, in this case, the monotonicity breaking can occur only if one of the left and right slopes (4.89) at a given point is at least three times larger than the other. This is very unlikely to occur if one is dealing with smooth solutions using a numerical grid with the required resolution. But this can be a problem in at least two scenarios:

- When one is dealing with piece-wise continuous solutions, where the discontinuities appear independently of the space resolution.
- When one is dealing with smooth solutions that get steep gradients at specific locations during evolution. This is actually the case in Black-Hole simulations when one uses singularity-avoidant slicing conditions, as we will see later.

A monotonicity-preserving algorithm can be obtained by using the nonlinear 'monotonic centered' (MC) slope reconstruction [36]

$$\Delta^{MC} \equiv minmod(\, 2\Delta^L \,,\ \Delta^C \,,\ 2\Delta^R \,) \,, \tag{4.91}$$

instead of the linear average (4.90), in combination with the upwind algorithm (4.88). The *minmod* function is defined as follows:

- If all the arguments have the same sign, then it selects the one with smaller absolute value.
- If one of the arguments has different sign than the others, then it is zero.

In this way, the slopes are limited in order to avoid spurious oscillations. The rule is that interface values must lie between their neighbor node values (see Fig. 4.4). There is a slight amount of numerical dissipation at the extreme points (where left and right slopes have different sign), but this is common to the class of 'High-resolution Shock-capturing methods' (HRSC) that are currently used in Fluid Dynamics. The particular algorithm we have presented here, which we will call MMC because it combines the Marquina solver with the MC limiter, belongs to the class of 'Slope-limiter' (alternatively 'Flux-limiter') methods, as described in [33, 34].

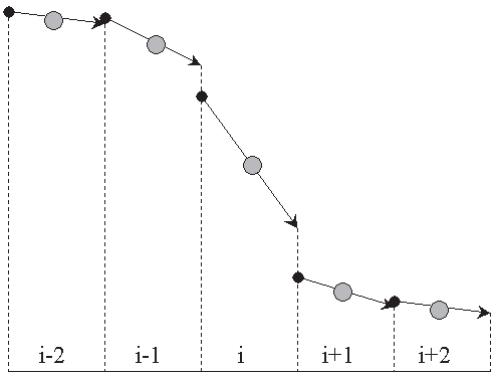

Fig. 4.4. Same as the second panel in Fig. 4.3, but using the monotonic-centered reconstruction. Notice that the interface values are bounded now between the neighbor nodes, so that monotonicity is preserved both for the *left* values (*arrows*) and by the *right* ones (*dots*) at every interface (*dotted lines*)

4.3.3 The Gauge-Waves Test-Bed

Now we will test the developments presented in this chapter in a very peculiar situation: Minkowski spacetime endowed with a non-conventional gauge condition. To understand what we are meaning by this, let us start from Minkowski metric in the standard inertial coordinate system

$$ds^2 = -dt^2 + dx^2 + dy^2 + dz^2 \ , \tag{4.92}$$

and perform a general conformal transformation in the two-dimensional sector spanned by the $t,\ x$ coordinates, namely

$$ds^2 = H^2(t,x)\ (-dt^2 + dx^2) + dy^2 + dz^2 \ , \tag{4.93}$$

where now the $(t,\ x)$ labels refer to the transformed coordinates.

We can simulate here propagation along the x axis (in the positive sense, for instance), by taking

$$H(t,x) = h(x-t) \tag{4.94}$$

(notice that light speed along the x axis is still $v = 1$ in the transformed coordinates). The exact time evolution can be then easily obtained from the initial profile

$$H(0,x) = h(x) \ . \tag{4.95}$$

Note that (4.94) implies

$$\alpha = h \ , \qquad K_{xx} = h' \ , \qquad A_x = h'/h \ , \qquad D_{xxx} = hh' \ . \tag{4.96}$$

The term 'Gauge waves' is justified by the propagation behavior (4.94) and the fact that the only non-trivial eigenfields belong to the gauge sector

(4.82). Notice that the metric form (4.93) corresponds to an harmonic slicing condition ($f = 1$), so that we must have also $m = 2$ to ensure strong hyperbolicity. The ordering parameter ζ is set to zero, but this is irrelevant for the moment because only the x derivatives provide non-trivial contributions.

We can evolve either smooth profiles, like a periodic sine wave [15]

$$h(x) = 1 - A\ sin\left(\frac{2\pi x}{d}\right) \tag{4.97}$$

(with the amplitude $A < 1$, of course) or non-smooth profiles, like the periodic 'saw-teeth' one

$$h(x) = \begin{array}{ll} x & 0 < x < d/4 \\ d/2 - x & d/4 < x < 3d/4 \\ -d + x & 3d/4 < x < d \end{array} \tag{4.98}$$

which corresponds to a discontinuous (step-like) profile for the first derivatives in (4.96). In our simulations we will use periodic boundary conditions, setting the space period along the x axis $d = 1$, so that a round trip will be completed after $\Delta t = 1$.

We will first check the standard Flux-conservative second-order method, defined by the interface average (4.61). In Fig. 4.5, we see the propagation along the x axis of different K_{xx} profiles. The simulation takes place in a 'numerical simulation channel' of $50 \times 5 \times 5$ grid points, with periodic boundaries along every axis.

The smooth wave profile can be compared with the initial condition after one round-trip, showing a very good accuracy, even for our modest grid resolution. The step-like profile is compared with the initial conditions after just

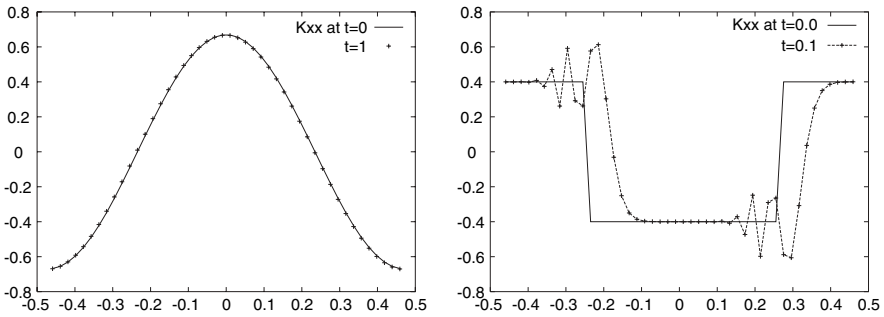

Fig. 4.5. Gauge-wave evolution, as computed with the standard Flux-conservative second-order method. The initial K_{xx} profiles (*solid lines*) propagate along the x axis from left to right. The first plot corresponds to the evolution of a smooth wave profile (*cross marks*), which is compared with the initial condition after one round-trip: the difference can barely be seen. The second plot shows the evolution of a step-like profile, which is compared with the initial condition after 10 iterations, showing spurious oscillations behind both moving discontinuity fronts

10 iterations, showing instead the expected spurious oscillations that would contaminate the full profile after a full round-trip.

The spurious oscillations disappear if we use the first-order upwind method, defined by the upwind prescription (4.88), as shown in Fig. 4.6. Both the sinus and the step-like profile are compared now with the initial condition after a full round trip. Severe numerical dissipation tends to smooth out everything, leading to unacceptable errors. Increasing the grid resolution could improve this results, but this would amount to waste a precious resource in Numerical Relativity applications.

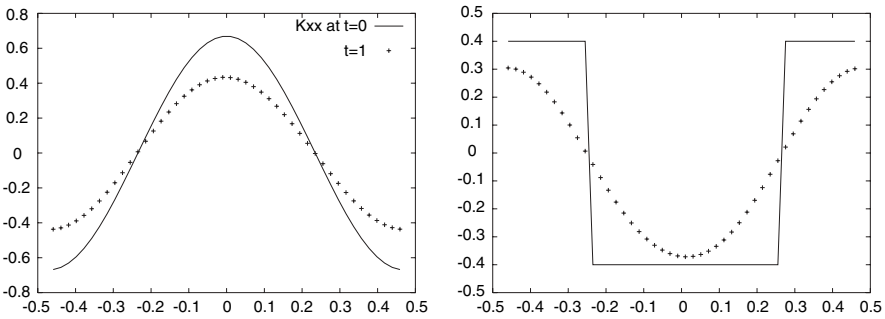

Fig. 4.6. Same as Fig. 4.5, but with the evolution computed with the first-order upwind method, defined by the prescription (4.88). The evolution of a step-like profile is compared now with the initial condition after a full round trip, just like in the smooth case. The monotonicity of the initial solution is preserved: the spurious oscillations have disappeared. However, the profiles after one round trip (*cross marks*) show the effect of excessive numerical dissipation, departing from the initial conditions (*solid lines*) in a clear way

The results for the MMC second-order method, defined by the prescription (4.91), give us the best of both worlds, as shown in Fig. 4.7. Smooth profiles are well resolved, even in our modest-size numerical grid. In addition, step-like profiles are free of spurious oscillations, and keep their shape in the smooth trams. The MMC method will be definitely our choice, unless we are sure that we are dealing just with well-resolved smooth solutions, where the standard second order method provides a simpler alternative.

Multidimensional Cases

Let us consider now the multidimensional case. This is the real challenge, because in the one-dimensional (1D) case there are mathematical theorems that ensure the success of Shock-capturing methods for Flux-conservative Strongly-hyperbolic systems [33]. The slight monotonicity breaking which remains in the right-hand-side plot in Fig. 4.7 is due to the source terms that break the strict Flux-conservative structure required for these theorems to apply.

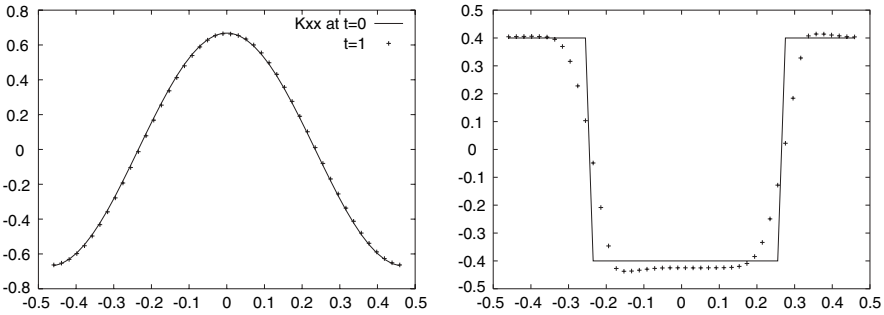

Fig. 4.7. Same as the preceding figures, but with the evolution computed with the monotonic-centered second-order method, defined by the prescription (4.91). The step-like profile is compared now with the initial condition after a full round trip, just like in the smooth case. The spurious oscillations have also disappeared. Numerical dissipation is no longer affecting the sinus profile after one round trip in a significant way

This is no longer true in the multidimensional case, although the current strategies try to mimic the 1D algorithms in one or another way [34]. The difficulty is clearly shown when we decompose the evolution system (4.70) in the following way

$$\partial_t \, \mathbf{u} + \mathbf{A}^x \, \partial_x \, \mathbf{u} + \mathbf{A}^y \, \partial_y \, \mathbf{u} + \mathbf{A}^z \, \partial_z \, \mathbf{u} = 0 \, , \tag{4.99}$$

so that it is evident that every axis has its own characteristic matrix. As far as these three matrices do not commute, there is no common basis of eigenvectors that can be safely be used in order to 'upwind' the interface values when one deals with oblique shocks.

Our approach will be to consider every direction on its own, independently of the others. This means for instance that the y (respectively, z) interface values will be selected by using $\mathbf{A}^y$ (respectively, $\mathbf{A}^z$) as the characteristic matrix, in the same way we did along the x direction in the 1D case. The final update of the computed fields will be done by simultaneously, taking into account every direction, as specified in (4.57) [48].

Coming back to our test-bed problem, the analytic solution for oblique discontinuities can be obtained by performing a simple space rotation around the z axis on the line element (4.93). We will consider a 45 degrees rotation

$$x = (x' - y')/\sqrt{2} \, , \qquad y = (x' + y')/\sqrt{2} \, , \tag{4.100}$$

in order to get a solution which is periodic along both the x and y axes in a square domain. Notice that all the first derivative quantities

$$A_i \, , \qquad K_{ij} \, , \qquad D_{kij} \, , \tag{4.101}$$

transform like tensors under the linear coordinate transformation (4.100).

We will test again the MMC method with the oblique step-like profile given in Fig. 4.8. The simulation takes place now in a 'numerical simulation pool' of $50\times50\times5$ grid points, with periodic boundaries along every axis. The solution after one round trip does not show any sign of spurious oscillations. In order to take a closer look, we plot in Fig. 4.10 a longitudinal section corresponding to the $y=0$ plane.

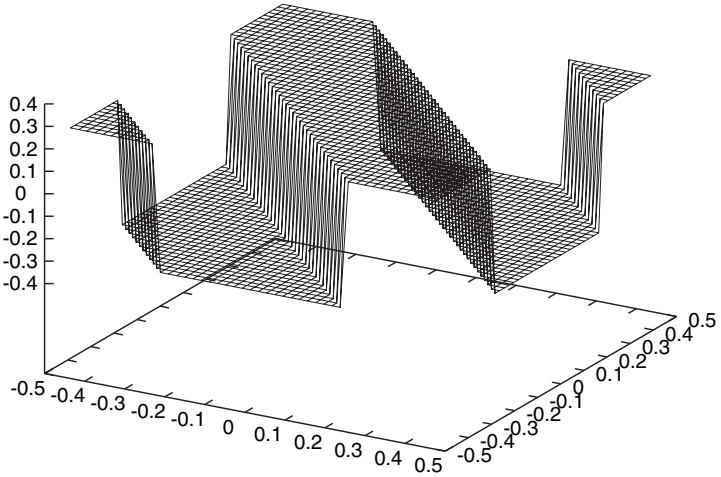

Fig. 4.8. Initial data for the K_{xx} components corresponding to an oblique discontinuity profile in the $x-y$ plane. Notice the periodicity along every space axis. The projection on the front face coincides with the 1D step-like initial profiles in the preceding figures

We still see some overshots that break the monotonicity of the initial profile, but this is not a multidimensional effect: the same feature was yet present in the second plot in Fig. 4.7. The results actually look like what one would get after a 45 degrees rotation from the previous 'numerical channel' simulation, where the propagation direction was aligned with the x axis. We can conclude that the MMC method can be extended to the multidimensional case in the way we have described. The fact that the parallax effect causes super-luminal propagation of the discontinuities along the coordinate axes, as shown in Fig. 4.2, does not seem to be a real problem in our case.

There is another important feature of these CFD methods, related to the gauge instabilities, as it can be seen in Fig. 4.11. We keep the numerical simulations for the smooth profile (4.97) running until 100 round trips in order to see the cumulative effect in every numerical method. The initial amplitude is $A=0.1$, which is larger than the one proposed for this case in [15].

We have represented in Fig. 4.11 the L_∞ norm of $tr\,K$. This means the maximum of (the absolute value of) $tr\,K$, which should be constant allowing for the exact solution (4.94). As expected, the first-order upwind method

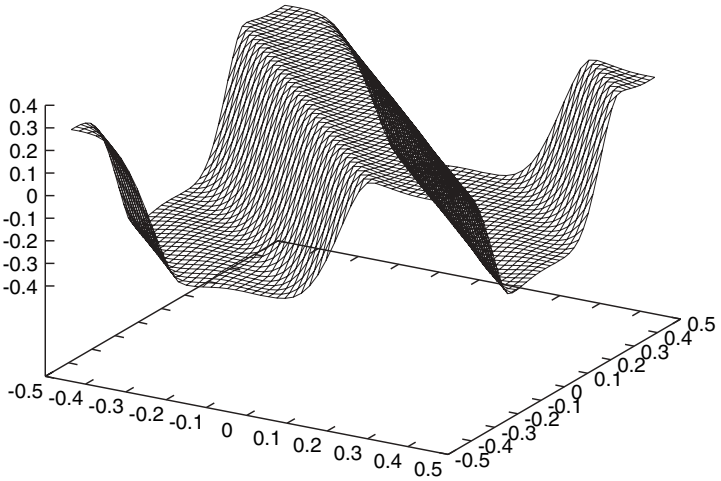

Fig. 4.9. The initial K_{xx} profile shown in Fig. 4.8, corresponding to an oblique step, is evolved during one full period, using the MMC method. The result agrees with what one could get after a 45 degrees rotation from the previous simulation, where the propagation direction was aligned with the x axis, as shown in the second plot in Fig. 4.7

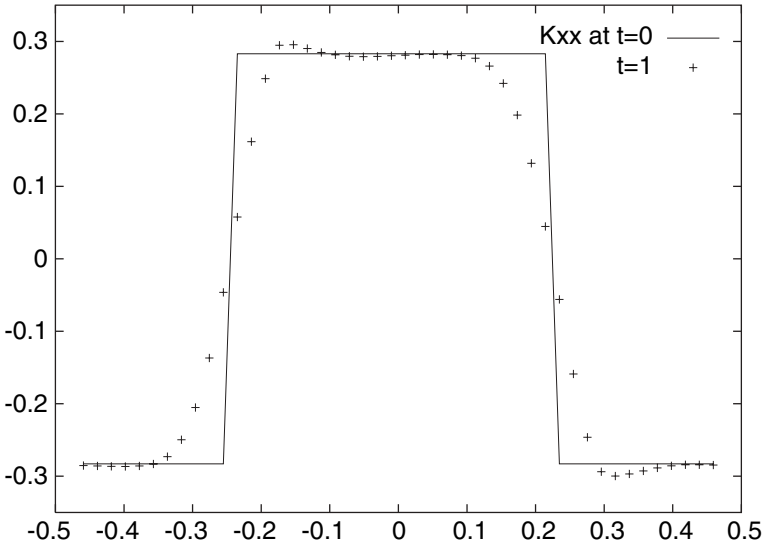

Fig. 4.10. A longitudinal section, corresponding to the $y = 0$ plane, of the results shown in Fig. 4.9. There are slight overshots in the evolved profile (*cross marks*) with respect to the initial K_{xx} profile (*solid line*), similar to the ones appearing in the second plot in Fig. 4.7

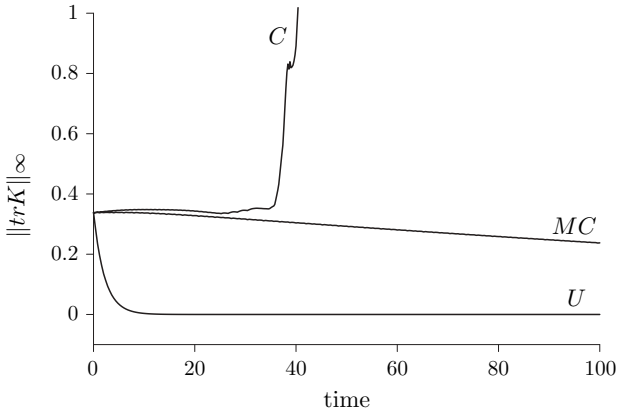

Fig. 4.11. The L_∞ norm of $tr\,K$ is shown for the initial sinus profile, with an initial amplitude $A = 0.1$. The first-order upwind method (labelled as U) produces exponential dissipation. The second-order centered method (labelled as C) starts by keeping the norm constant, but crashes before completing 40 round-trips. The MMC method shows instead a slight linear decrease

flattens the solution very quickly. The standard second-order method keeps the initial value nearly constant, but crashes because of high-frequency gauge instabilities (this crash was avoided in [15] by selecting a much lower initial amplitude). The non-linear MMC method shows a little amount of extra dissipation, but manages to complete the 100 round-trips. Moreover, the final amplitude is still about two thirds of the initial one.

Gauge instabilities are still not fully understood. Our results seem to support the existence of unstable high-frequency gauge modes that can be cured if one replaces the standard (linear) high-resolution algorithms by the MMC (non-linear, Shock-capturing) one. This provides an additional reason to consider Shock-capturing methods as a useful tool, not only for the Hydrodynamic equations, but also for the gravitational field equations in the full 3D case.

5

Boundary Conditions

5.1 The Initial-Boundary Problem

Most Numerical Relativity simulations are devised to approximate the time evolution of the dynamical fields starting from data given on an initial time slice: the General Relativistic Cauchy or initial-value problem (IVP). The theoretical formalisms we have described so far are built with the objective of getting a well-posed Cauchy problem. This ensures, at the continuum level, that the solution is unique and depends smoothly on the initial data. A well-posed Cauchy problem is also a necessary condition for the existence of stable numerical algorithms that transpose the same property at the discrete level: the time evolution of the selected initial data must provide a sound approximation to the corresponding solution (the accuracy must improve with increasing numerical resolution).

The numerical applications we have presented in the preceding chapters were dealing just with periodic solutions. This means that we could identify the first points of the numerical grid with the last ones along every axis: from the continuum point of view, our computational arena has the topology of a three-torus. In this way, there is no genuine 'first' or 'last' point: we can always rotate the torus along one symmetry axis, so that the chosen point gets surrounded by the number of neighbors required for a given computational stencil. As a consequence, only initial data are required to produce a solution, both at the continuum and the discrete levels.

In physical applications, however, we will rarely find this three-torus topology. Three-dimensional Finite Difference grids usually start at some point and end at some other one along every axis, and this fact poses a serious problem both at the continuum and at the discrete level:

- From the discrete point of view, the numerical stencil that is being used for the 'interior' points needs to be modified at end-points, or even at next-to-end points, where the required number of neighbors is not available inside the numerical grid.

C. Bona and C. Palenzuela Luque: *Elements of Numerical Relativity*, Lect. Notes Phys. **673**, 93–118 (2005)
www.springerlink.com

- From the continuum point of view, the computational domain has a border, so that information can cross it in both senses. Of course, incoming information can not be obtained from inside, so it must be specified through additional conditions. These 'Boundary conditions' are relevant to the well-posedness of the system: the pure initial value problem is then transformed into a initial-boundary problem (IBVP).

5.1.1 Causality Conditions: The 1D Case

In order to clarify these points, let us focus for the moment in the one-dimensional (1D) case. We see in Fig. 5.1 the domain of dependence of a boundary point P, displayed as a shaded cone. It is clear that the region outside the numerical grid do have causal influence on P, so that extra physical information is required at the boundary. From the numerical point of view, the stencil at P must be one-sided (like the one displayed as a dotted triangle) instead of the centered stencil discussed in previous chapters: this means that the discretization algorithm must be changed at P.

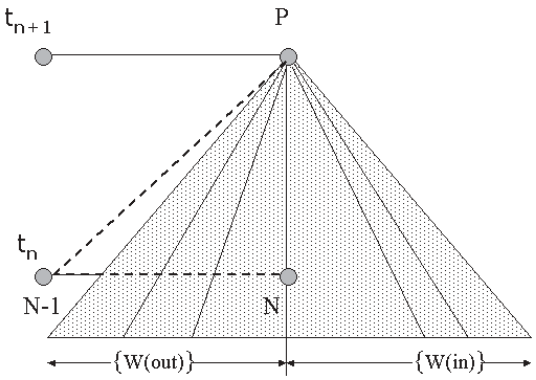

Fig. 5.1. The domain of dependency of a given boundary point P is shown as a *shaded* cone. The outgoing components w^{out} are contained into the left half-cone, so that their values can be computed consistently by using a one-sided (*upwind*) stencil, like the one shown as a *dotted triangle*. The ingoing components w^{in} belong instead to the right half-cone, which is outside the numerical grid: they must be provided by the boundary conditions

To be more specific, let us consider a 1D Strongly-hyperbolic Flux-conservative system (we neglect source terms for the moment)

$$\partial_t \, \mathbf{u} + \partial_x \, \mathbf{F} = 0 \, , \tag{5.1}$$

The characteristic matrix

$$\mathbf{A} = \frac{\partial \mathbf{F}}{\partial \mathbf{u}} \tag{5.2}$$

can be fully diagonalized and the set of dynamical fields $\mathbf{u}$ can be then decomposed in the basis of eigenfields $\mathbf{w}$, that is

$$u_r = \sum_s C_{rs}\ w_s\ . \tag{5.3}$$

We will classify the characteristic eigenfields into two subsets:

- **Incoming** eigenfields $\mathbf{w}^{in}$: the ones with characteristic speed pointing inside the computational region.
- **Outgoing** eigenfields $\mathbf{w}^{out}$: the ones with characteristic speed pointing outside the computational region (this includes the tangent ones).

To justify the use of the 'incoming' and 'outgoing' terms, let us consider the simplest case, when the characteristic matrix (5.2) has constant coefficients. Then, the original system (5.1) can be decoupled into a set of independent advection equations for the characteristic fields, namely

$$\partial_t w_r + \lambda_r\, \partial_x w_r = 0\ , \tag{5.4}$$

so that the propagation behavior is like the one shown in Fig. 5.1. Simple causality considerations lead then to the two main requirements for physically sound boundary conditions

- Boundary conditions must provide the values of all the incoming eigenfields. Otherwise we will loose the uniqueness of the solution (not enough information is given) and this will result into numerical instabilities.
- Boundary conditions must not restrict the values of the outgoing eigenfields. This is because the domain of dependence of these fields is fully contained into the computational region, so that their values are completely determined by inside information. Any further condition would be either redundant or inconsistent.

The prototype of a boundary condition verifying these two main requirements is provided by the linear relationship

$$w_r^{\ in} = \sum_s M_{rs}\ w_s^{\ out} + C_r \tag{5.5}$$

where the coefficients M_{rs} and C_r are independent of the dynamical fields. We will explore the generic conditions (5.5) in more detail in what follows.

5.1.2 1D Energy Estimates

The eigenfield basis $\mathbf{w}$, which is associated to any 1D strongly hyperbolic system, allows one to introduce a positive-definite quadratic form in the space of dynamical fields:

$$E = \sum_r (w_r)^2 \tag{5.6}$$

(Energy metric).

We will consider the 'Energy estimate' $\overline{E}$, obtained as the integrated value of E over the computational domain

$$\overline{E} = \int_a^b E \; dx = \sum_r \int_a^b (w_r)^2 \; dx \; . \tag{5.7}$$

Let us consider again the simplest case, with constant characteristic speeds. The evolution of the eigenfields is governed by (5.4). This is a pure advection process, where the initial profiles are transported without altering its shape. This means that the integrals in the sum (5.7) would not change in time when computed over the full x axis. But, due to the finite size of the computational domain, one has instead some end-point contributions to the time derivative, namely

$$\partial_t \; \overline{E} = -2 \; \sum_r \; \lambda_r \int_a^b w_r \; \partial_x w_r \; dx = - \left[\sum_r \lambda_r (w_r)^2 \right]_a^b \; . \tag{5.8}$$

A well-posed initial-boundary problem can be easily obtained now by requiring that the right-hand-side term in (5.8) be bounded in a suitable way. As far as every dynamical field at every grid point contributes to the energy estimate $\overline{E}$ (which is positive-definite so that there can no be cancellations of any kind), this would mean that the values of the dynamical fields themselves can not grow too fast (at the continuum level at least).

A closer look at (5.8) suggests the following decomposition in terms of incoming and outgoing eigenfields

$$\partial_t \; \overline{E} = - \left[\sum_r \lambda_r^{in} (w_r^{in})^2 + \sum_s \lambda_s^{out} (w_s^{out})^2 \right]_a^b \; , \tag{5.9}$$

where it is clear that the outgoing terms contribution goes in the right sense ($\partial_t \; \overline{E} \; \leq \; 0$), whereas incoming terms contribute instead in the wrong one ($\partial_t \; \overline{E} \; > \; 0$) because their characteristic speed is positive at the first point a and negative at the last point b.

Now we are in position to analyze the effect of different choices in the generic boundary condition (5.5):

- The most conservative one would be to suppress all the incoming fields at the boundaries, that is

$$w_s^{in} = 0 \qquad \forall s \; , \tag{5.10}$$

(maximally dissipative boundary condition). In this case it is clear that the energy estimate $\overline{E}$ will diminish with time at the maximum rate.

- The next safe choice would be to relate every incoming field at the boundary with an outgoing one, grouped by pairs, that is

$$w_s^{in} = \sigma \; w_r^{out} \; , \tag{5.11}$$

  so that the corresponding terms in the sum (5.9) can be grouped as

$$(\lambda_r^{out} + \sigma^2 \lambda_s^{in}) \; (w_r^{out})^2 \; , \tag{5.12}$$

  which will have the right sign provided that the 'reflection coefficient' σ is small enough, that is

$$\lambda_r^{out} + \sigma^2 \lambda_s^{in} \geq 0 \; . \tag{5.13}$$

- An interesting particular case of the former one is when the corresponding outgoing speed λ_r^{out} is zero. Then, there is no 'small enough' non-trivial choice of σ that could verify (5.13). One has instead the contribution

$$\sigma^2 \lambda_s^{in} \; (w_r^{out})^2 \; , \tag{5.14}$$

  which goes always with the wrong sign. Notice, however, that this term is constant in time (λ_r^{out} is actually zero), so that it will produce a linear increasing of the energy estimate $\overline{E}$ in the worst case.
- As an alternative, one could just specify the incoming fields at the boundaries in terms of some given functions, namely

$$w_s^{in} = C_s(t) \; , \tag{5.15}$$

  so that a convenient upper bound for the growth of the energy estimate can be obtained by a suitable choice of the functions $C_s(t)$ at the boundaries.

Note that the Energy metric (5.6) is far from being unique: the characteristic eigenfields could be multiplied by any set of arbitrary factors and, when some characteristic speeds coincide, the linear degeneracy of the corresponding eigenspace produces non-equivalent quadratic forms which could be used as alternative starting points, leading to different energy estimates. There are also other more general choices, as we will see in what follows.

5.1.3 The Multi-Dimensional Case: Symmetric-Hyperbolic Systems

Let us go back to the multidimensional case, to the linear Flux-conservative system

$$\partial_t \; \mathbf{u} + \partial_k (\mathbf{A}^k \; \mathbf{u}) = 0 \; , \tag{5.16}$$

where we will assume again that the characteristic matrices $\mathbf{A}^k$ have constant coefficients for simplicity. This system will be said to be Symmetric-hyperbolic if there exists a basis of dynamical fields $\mathbf{u}$ such that, for every space direction $\boldsymbol{n}$, the corresponding characteristic matrix is symmetric, that is

$$n_k A^k{}_{rs} = n_k A^k{}_{sr} \qquad \forall \boldsymbol{n} \ . \tag{5.17}$$

It is clear that any symmetric-hyperbolic system must be also strongly hyperbolic: every real symmetric matrix can be diagonalized and all the corresponding eigenvalues are real. The converse is not true: there are as many characteristic matrices as space directions and the requirement all of them must be symmetric when expressed in a given basis is not trivial.

We will restrict ourselves to symmetric hyperbolic systems of the form (5.16). Let $\mathbf{u}$ be one the basis in which the symmetry requirement (5.17) is fulfilled. We will then define the Energy metric to be

$$E = \sum_r (u_r)^2 \ . \tag{5.18}$$

Now some comments are in order:

- In the 1D case, using the basis of eigenfields $\mathbf{w}$ ensures that the (only) characteristic matrix is in diagonal form (that is symmetric, of course). This means that in 1D symmetric hyperbolicity is equivalent to strong hyperbolicity.
- In the 3D case, there is no common basis of eigenvectors for the characteristic matrices along different directions (unless all these matrices commute). This means that the basis fields $\mathbf{u}$ are not eigenvectors (at least not in the generic case).
- This suggests, even in the 1D case, a further freedom in choosing the basis vectors for the Energy metric: any combination of the form

$$u_r = \sum_s R_{rs} w_s \ , \tag{5.19}$$

  where $\mathbf{R}$ is any orthogonal matrix, will work, as we will see below.

Now we can proceed along the same lines as in the 1D case. We will consider again the energy estimate, obtained by integrating E over the computational domain

$$\overline{E} = \int E \ dV = \sum_r \int (u_r)^2 \ dV \ . \tag{5.20}$$

Its time variation is given by (we are using the symmetry requirement here)

$$\partial_t \ \overline{E} = -2 \ \sum_{rs} A^k{}_{rs} \int u_r \, \partial_k u_s \ dV = - \sum_{rs} A^k{}_{rs} \oint u_r u_s \ n_k \ dS \ , \tag{5.21}$$

where the surface integral is over the boundary of the computational domain. Notice that we need only one characteristic matrix at a time in order to compute the last integral: the one corresponding to the normal direction $\boldsymbol{n}$ to the given boundary surface, that is

$$\mathbf{A}^n = n_k \mathbf{A}^k \ . \tag{5.22}$$

Note also that the term appearing in each surface integral is a scalar with respect to the orthogonal transformations (5.19). It can be then computed in the basis of characteristic fields, where $\mathbf{A}^n$ takes the diagonal form

$$\mathbf{A}^n = diag(\{\lambda_r^{in}\},\ \{\lambda_s^{out}\})\ , \tag{5.23}$$

so that one finally gets the same kind of result than in the 1D case

$$\partial_t\ \overline{E} = -\oint \left[\ \sum_r \lambda_r^{in}(w_r^{in})^2 + \ \sum_s \lambda_s^{out}(w_s^{out})^2\right]\ dS\ . \tag{5.24}$$

This means that the Energy method can be applied to devise boundary conditions for multidimensional symmetric-hyperbolic systems in the same way as in the 1D case, as discussed in Sect. 5.1.2. Some words of caution are convenient at this point:

- Energy estimates can provide sufficient conditions for a well-posed IBVP in the symmetric-hyperbolic case. But, as far as the Energy metric is not unique, the resulting conditions may not be necessary.
- The arguments presented here apply just to the continuum level. Sufficient conditions at the discrete level will follow only if the numerical algorithm is able to preserve the integration-by-parts rule, which plays a key role in these developments. This restricts the choice of discrete algorithms, both at the interior points and at the boundary ones. See [49] for details.
- The results presented here hold only for pure Flux-conservative systems (no source terms) and for the linearized case, where the coefficients of the characteristic matrices are constant. None of these requirements is fulfilled in Numerical Relativity applications: one must then use Energy estimates just as a guideline.

A simple example of a symmetric-hyperbolic system is provided by the first-order version (4.14–4.20) of the Z4 system in the harmonic slicing case ($f = 1,\ m = 2$), for the choice $\zeta = -1$ of the ordering parameter [29]. The Energy metric can be chosen to be

$$E = K_{ij}K^{ij} + \lambda_{kij}\lambda^{kij} + \Theta^2 + V_kV^k\ , \tag{5.25}$$

but a 'constant' term of the form

$$(A_k - D_k + 2V_k)(A^k - D^k + 2V^k)\ , \tag{5.26}$$

containing just fields with zero characteristic speed, could also be added.

We can now check the results presented in this section by using again the robust stability test-bed. This time periodic boundaries will be replaced by algebraic boundary conditions of the form (5.11) along every axis in a small (20^3 nodes) numerical grid. Note that the outward unit normal $\boldsymbol{n}$ at the boundary must be defined at corner points (see Fig. 5.2).

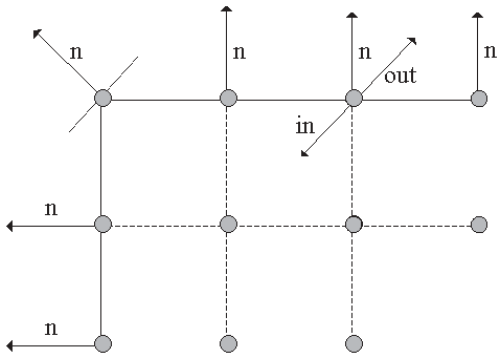

Fig. 5.2. The outward normals to the boundaries of a two-dimensional grid are shown. A normal direction must be chosen at corner points. Notice that the decomposition into incoming and outgoing eigenfields is direction-dependent, so that there are physical 'in' and 'out' modes along every direction, not just normal to the boundary surface

We see in Fig. 5.3 the time evolution of $\|trK\|_\infty$, that is the maximum of the absolute value of trK, which is one of the main contributions to the energy estimate (5.25). For the maximally dissipative case $\sigma = 0$, the expected decreasing is clearly seen. The case $\sigma = \pm 1$ deserves a further comment, because every non-zero eigenvalue appears twice, with different signs (zero shift case), that is

$$\lambda^{in} = -\lambda^{out} \,, \tag{5.27}$$

so that the resulting terms (5.12) do not contribute to the energy decreasing when $\sigma^2 = 1$. Then, a constant value of the energy estimate would be expected at the continuum level. There are two alternative ways of explaining the observed decreasing when $\sigma = \pm 1$ in Fig. 5.3:

- As the effect of the non-linear source terms and/or the non-constant coefficients in the characteristic matrices involved. This could also explain the different behavior of the $\sigma = +1$ and the $\sigma = -1$ cases. This is very unlikely, because the noise level we are using here is so low that non-linear contributions can be safely neglected.
- As the effect of numerical dissipation. This does not come from the numerical algorithms used at interior points, which do not show so much dissipation (see for instance Fig. 3.3). This must be due instead to the use of the first-order upwind method, which is known to be highly dissipative (see Fig. 4.6), as the one-sided algorithm for the outgoing modes at boundary points.

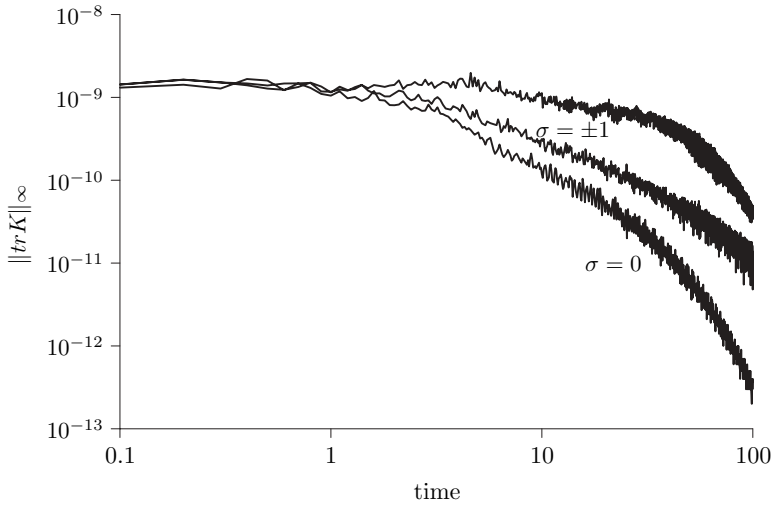

Fig. 5.3. Time evolution of the maximum of the absolute value of trK, which is one of the main contributions to the energy estimate. For the maximally dissipative case $\sigma = 0$, the expected decreasing is clearly seen. The unexpected decreasing of the $\sigma = \pm 1$ cases is due to numerical dissipation, caused by the use of the first-order upwind algorithm at the boundary points

5.2 Algebraic Boundary Conditions

Symmetric hyperbolicity is a strong requirement to be imposed on Numerical Relativity evolution systems. Of course, the sufficient conditions that would follow for the IBVP are rewarding, but Numerical Relativity evolution systems contain both source terms and non-constant characteristic matrices. This means, as stated before, that the resulting conditions must anyway be considered just as guidelines, which have to be validated in test-bed problems.

In addition, we know that true Einstein's solutions must verify the Energy and Momentum constraints. Simple algebraic conditions like (5.11) do not allow for this fact: it follows that constraint-violating modes will appear at the boundaries of the computational region and (the incoming components) will propagate inwards. Then, even if we started from constrained initial data, the computed solution will no longer be a true Einstein's solution once time evolution begins, even at the continuum level. As we will see, constraint-preserving boundary conditions are much more sophisticated than (5.11), and the energy method can not be applied to this kind of boundary conditions in a simple way.

We will consider constraint-preserving boundary conditions in the next section. As a previous step, we will keep considering here simple algebraic conditions, like (5.11). But now we will enlarge the class of evolution systems to include all the strongly hyperbolic ones. As far as Energy considerations

will no longer apply here, we will introduce a different kind of developments that will be used as a guideline for setting up suitable boundary conditions. Other developments have also been considered, like the Fourier-Laplace decomposition [19], which would provide necessary conditions for getting a well posed IBVP problem necessary conditions. The one we will present here is more in keeping with the hyperbolicity analysis presented in Sect. 4.3.1.

5.2.1 The Modified-System Approach

As stated before, boundary points are dealt with in a special way. The fact that we are using boundary conditions there means that the evolution system is being actually modified: a subset of the original equations is replaced by these boundary conditions. For the purposes of our analysis, the modified system can be obtained as follows:

- Starting with the original strongly-hyperbolic system, we compute all the dynamical fields at the boundary points. Notice that this requires using a one-sided algorithm for the space discretization (see Fig. 5.1).
- We decompose the computed dynamical fields in the basis of characteristic eigenfields $\mathbf{w}$ corresponding to the space direction $\boldsymbol{n}$ normal to the boundary surface (a normal $\boldsymbol{n}$ is required even at corner points, see Fig. 5.2). As discussed before, these characteristic fields are classified into incoming and outgoing ones, according to the sign of their characteristic speed.
- We keep the values of the outgoing eigenfields (this includes the tangent ones). Their evolution equations are then the original ones, that is:

$$\partial_t \ \mathbf{w}^{out} + \partial_k (\mathbf{A}^k \ \mathbf{w}^{out}) = \cdots \tag{5.28}$$

  (only the principal part is written here). Notice that the eigenvectors $\mathbf{w}^{out}$ are associated to the $\boldsymbol{n}$ direction only, so that characteristic matrices along other directions are not in diagonal form.
- We replace the original values of the incoming eigenfields by the ones obtained from the boundary conditions, for instance

$$w_r{}^{in} = \sigma_{rs} w_s{}^{out} \tag{5.29}$$

  (no summation here), which is a generalization of (5.11). In this way, the evolution equations for the incoming fields are being modified, so that the evolution system that is being actually used at boundary points is no longer the original one.

We will require the resulting 'modified system' (5.28, 5.29) to be hyperbolic. This means that the (modified) characteristic matrices along every direction must have real characteristic speeds. This is trivial along the selected direction $\boldsymbol{n}$, for which the (modified) basis of eigenfields is formed now by

- the original outgoing eigenfields ${w_s}^{out}$, with characteristic speeds ${\lambda_s}^{out}$.
- the combinations
$$ {w_r}^{in} - \sigma_{rs} {w_s}^{out} \, , \tag{5.30} $$
with zero characteristic speed, as it follows from the algebraic boundary condition (5.29).

But this is far from being trivial along other directions, oblique to the boundary surface, as depicted in Fig. 5.2.

To be more specific, we will consider the characteristic matrix along a generic oblique direction $\boldsymbol{r}$, that is
$$ \mathbf{A}^r = r_k \, \mathbf{A}^k \, , \tag{5.31} $$
where the vector $\boldsymbol{r}$ is related with $\boldsymbol{n}$ by
$$ \boldsymbol{r} = \ \boldsymbol{n} \, cos\varphi + \boldsymbol{s} \ sin\varphi \, , \tag{5.32} $$
and we have taken
$$ \boldsymbol{n}^2 = \boldsymbol{s}^2 = 1 \, , \qquad \boldsymbol{n} \cdot \boldsymbol{s} = 0 \, . \tag{5.33} $$
The hyperbolicity requirement amounts to demand that all the resulting characteristic speeds be real for any value of the angle φ.

5.2.2 The Z4 Case

We will apply the preceding considerations to the first order Z4 evolution system (4.14–4.20). We obtained in Sect. 4.3.1 the complete list of eigenvectors for the generic case, for which the Z4 system is strongly hyperbolic. We will here provide simple algebraic boundary conditions of the form (5.11) for the incoming modes.

Let us consider the boundary which normal $\boldsymbol{n}$ pointing outwards, so that outgoing fields correspond to positive characteristic speeds and vice-versa. We get then
$$ E^- - \sigma_e \ E^+ = 0 \tag{5.34} $$
$$ L_{ij}^- - \sigma_{ij} \ L_{ij}^+ = 0 \tag{5.35} $$
$$ G^- - \sigma_g \ G^+ = 0 \, , \tag{5.36} $$
where different reflection coefficients are allowed for different fields.

These equations replace the evolution equations for the 7 (remember that $L_{ij}^{\pm}$ is traceless) incoming eigenfields of the original system (4.14–4.20), by providing at the same time 7 'outgoing' (actually tangent) eigenfields of the modified system. Another set of 17 tangent eigenfields (zero characteristic speed) is given by
$$ A_p, \ D_{p\,ij}, \ A_k - f D_k + f \, m V_k \tag{5.37} $$
where $\boldsymbol{p}$ is the direction orthogonal to both vectors $\boldsymbol{n}$ and $\boldsymbol{s}$.

The remaining 14 dynamical fields can be grouped into the following sectors:

- **Energy sector** $\{E^+,\ V_s\}$. The corresponding evolution equations are (principal part only):

$$\frac{1}{\alpha}\ \partial_t\ V_s = -sin\varphi\ \partial_s[\ \Theta\ ] = -\frac{1+\sigma_e}{2}\ sin\varphi\ \partial_r[\ E^+\ ] \tag{5.38}$$

$$\frac{1}{\alpha}\ \partial_t\ E^+ = -\partial_r[\ V_r + \Theta\ cos\varphi\ ] = -\partial_r[\ E^+ cos\varphi + V_s\ sin\varphi\ ]\ . \tag{5.39}$$

It follows that the characteristic speeds are given by the solutions of the algebraic equation

$$\lambda(\lambda - \alpha\ cos\varphi) = \alpha^2\ sin^2\varphi\ \frac{1+\sigma_e}{2}\ , \tag{5.40}$$

so that real characteristic speeds are obtained for all φ if and only if

$$\sigma_e \geq -1\ . \tag{5.41}$$

- **Gauge sector** $\{G^+,\ A_s\}$. The corresponding evolution equations are (principal part only):

$$\begin{aligned}\frac{1}{\alpha}\ \partial_t A_s &= -sin\varphi\ \partial_s[\ f(trK - m\ \Theta)] \\ &= -\frac{1+\sigma_g}{2}\sqrt{f}\ sin\varphi\ \partial_r[\ G^+ + \cdots\ ]\end{aligned} \tag{5.42}$$

$$\begin{aligned}\frac{1}{\alpha}\ \partial_t\ G^+ &= -\partial_r[\ \sqrt{f}\ A_r + f\ cos\varphi\ trK\ ] \\ &= -\sqrt{f}\ \partial_r[\ G^+\ cos\varphi\ + A_s\ sin\varphi + \cdots\ ]\ .\end{aligned} \tag{5.43}$$

where the dots stand for coupling terms with the energy sector (these terms are irrelevant here for the eigenvalues calculation). It follows that the characteristic speeds are given by the solutions of the algebraic equation

$$\lambda(\lambda - \alpha\ \sqrt{f}\, cos\varphi) = f\ \alpha^2\ sin^2\varphi\ \frac{1+\sigma_g}{2}\ , \tag{5.44}$$

so that, allowing for the positivity of the gauge parameter f, real characteristic speeds are obtained for all φ if and only if

$$\sigma_g \geq -1\ . \tag{5.45}$$

- **Metric sector** $\{L^+_{ij},\ D_{sij}\}$. The corresponding evolution equations can be obtained from (principal part only)

$$\frac{1}{\alpha}\ \partial_t D_{sij} = -sin\varphi\ \partial_s[\ K_{ij}\ ] = -\frac{1+\sigma_{ij}}{2}\ sin\varphi\, \partial_r[\ L^+_{ij} + \cdots\ ] \tag{5.46}$$

$$\begin{aligned}\frac{1}{\alpha}\ \partial_t\ L^+_{ij} &= -\partial_r[\ \lambda^r_{ij} + cos\varphi\ K_{ij} + \cdots \\ &\quad -\frac{1+\zeta}{2}\ (r_i K_{nj} + r_j K_{ni} - n_i K_{rj} - n_j K_{ri})\ ]\end{aligned}$$

$$
\begin{aligned}
= -\partial_r [\; & L_{ij}^{+} \; cos\varphi + D_{sij} \; sin\varphi + \cdots \\
& -\frac{1+\zeta}{2} \; sin\varphi \; (s_i K_{nj} + s_j K_{ni} - n_i K_{sj} - n_j K_{si}) \\
& -\frac{1+\zeta}{2} \; sin\varphi \; (D_{ijs} + D_{jis} - s_i E_j - s_j E_i) \;] \; . \qquad (5.47)
\end{aligned}
$$

where the dots stand again for coupling terms with the previous sectors.

The evolution equation (5.47) for the outgoing 'metric' fields contains (unless $\zeta = -1$) crossed coupling terms that complicate the analysis. For the sake of simplicity, let us focus on the easiest case, which corresponds to the maximally dissipative condition

$$\sigma_{ij} = 0 \qquad \forall \; i \; , j \; . \qquad (5.48)$$

One gets then three variants of the same algebraic equation

$$\lambda(\lambda - \alpha \; cos\varphi) = \frac{1}{2} \; \alpha^2 \; sin^2\varphi \qquad (5.49)$$

$$\lambda(\lambda - \alpha \; cos\varphi) = \frac{1}{2} \; \alpha^2 \; sin^2\varphi \; \left[1 - \left(\frac{1+\zeta}{2} \right)^2 \right] \qquad (5.50)$$

$$\lambda(\lambda - \alpha \; cos\varphi) = \frac{1}{2} \; \alpha^2 \; sin^2\varphi \; [1 - (1+\zeta)^2] \; , \qquad (5.51)$$

depending on the particular set of components considered (the last two equations appear twice, so that one gets 10 characteristic speeds that complete the full set of 38). The most restrictive is the last one (5.51): it implies that one gets complex characteristic speeds for some values of φ unless

$$\zeta \leq 0 \; , \qquad (5.52)$$

so that the standard ordering case ($\zeta = +1$) is excluded. This provides a counter-example for the common belief that maximally dissipative boundary conditions 'should always work'.

We can check out these results by using again the robust stability testbed. As in the preceding section, where the symmetric hyperbolic case was considered, we will use algebraic boundary conditions of the form (5.29) along every axis in a small (20^3 nodes) numerical grid. In order to compare with the results shown in Fig. 5.3 for the $\zeta = -1$ case, we will keep the same values of the gauge parameters, corresponding to the harmonic slicing condition ($f = 1$, $m = 2$). This means that the only change will be to consider different values of the ordering parameter ζ, so that the evolution system is just strongly hyperbolic, but not symmetric hyperbolic.

We show in Fig. 5.4 the time evolution of the maximum of the absolute value of trK, which is one of the main contributions to the Energy metric (5.25). In the maximally dissipative case (left panel), we see that the choice

$\zeta = +1$ of the ordering parameter is unstable, whereas the two other choices $\zeta = 0\ , -1$ are stable and behave in the same way. In the $\zeta = 0$ case (right panel), we see that the 'extreme' values $\sigma = \pm 1$ of the reflection coefficients lead to code crashing, whereas other choices, closer to the maximally dissipative one $\sigma = 0$, work fine, showing the same decreasing behavior as in the symmetric hyperbolic case.

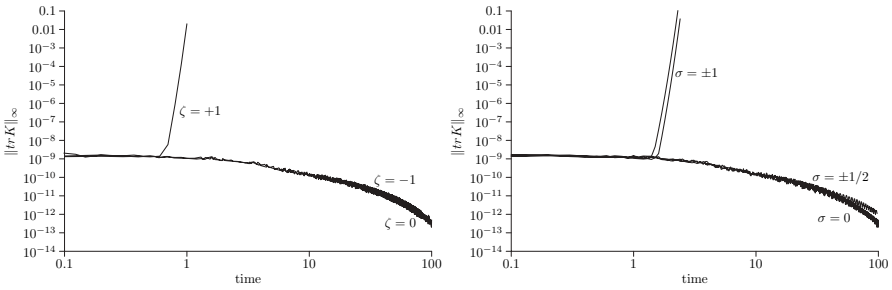

Fig. 5.4. Same as Fig. 5.3 for different values of ζ and σ. The plots in the left panel correspond to different choices of the ordering parameter in the maximally dissipative case ($\sigma = 0$). It follows that the $\zeta = +1$ choice of the ordering parameter is unstable. Conversely, the plots in the right panel correspond to different values of the reflection coefficients in the symmetric ordering case ($\zeta = 0$). The extreme choices $\sigma = \pm 1$ are unstable, while other choices, closer to the maximally dissipative one, still work

5.2.3 The Z-Waves Test-Bed

One can wonder whether the preceding results will still apply in the non-linear regime, where the combined effects of the source terms and the non-constant coefficients must be allowed for. This can be a source of problems, as we saw in Sect. 4.3.3, where the gauge-waves test-bed was used to check gauge-related issues. We have seen there how unstable (non-linear) gauge modes caused the failure of standard numerical algorithms.

We propose here the 'Z-waves' test-bed problem in order to check instead the dynamical issues related with the supplementary fields ($\Theta\ ,\ Z_i$) of the Z4 system. The term Z-waves comes from the expected dynamical behavior, allowing for the subsidiary condition (3.81): every component of the set ($\Theta\ ,\ Z_i$) should propagate as the solution of a wave equation with non-linear source terms.

This does not mean that our evolution equations are replaced by the wave equation. We will actually use the full Z4 first order system (4.14–4.20), with the gauge parameters choice:

$$f = 2\ , \qquad m = 0 \tag{5.53}$$

in (4.5), although other gauge values can be used without much change. The same is true for the ordering parameter: we take here the value $\zeta = 0$, but $\zeta = -1$ could be used as well. The only restriction here is given by (5.52).

The initial data will be consistent with Minkowski spacetime:

$$\alpha = 1 \,, \qquad \gamma_{ij} = \delta_{ij} \,, \qquad A_i = K_{ij} = D_{kij} = 0 \,, \tag{5.54}$$

and also $Z_i = 0$. The dynamics will come from a gaussian bump in Θ, which is initially at rest. (see the first plot in Fig. 5.5). The initial height of the bump is a 10% of the metric values, so we are not going to test just the linear regime. Notice also that the initial values of all metric derivatives are zero, so that the resulting dynamics is fully generated by the Θ field.

The simulation takes place in a $50 \times 50 \times 5$ 'numerical pool' with periodic boundary conditions along the z axis and maximally dissipative boundary conditions along both the x and y axes.

The dynamical behavior of the computed solution is, as expected, identical to that of the wave equation. The initial bump splits into two components. The outgoing one generates a circular wavefront that reaches the boundaries (see the third plot in Fig. 5.5) and gets out. The incoming one passes through the origin (see the second plot in Fig. 5.5), generating a second wavefront with negative amplitude (it can be seen in the fourth plot, contrasting with the zero-amplitude central region). This secondary wavefront finally reaches the boundary and gets out (fifth plot).

This dynamical pattern can be seen even more clearly in Fig. 5.6, where the initial gaussian bump has been replaced by a cylindrical step. In this way, the simulation corresponds to a weak solution, where the discontinuity in Θ is introduced through the initial data. We can no longer use here the second-order centered standard method for the space discretization: it will be replaced instead by the MMC method, as described in Sect. 4.3.2. The initial splitting into two components is now manifest in the second plot of Fig. 5.6. The outgoing one generates again a circular wavefront that reaches the boundaries (third plot) and gets out without any problem (notice that the initial discontinuity gets smoothed out during the simulation). The incoming one starts propagating inwards (second plot), passes through the origin (third plot), and generates again a second wavefront with negative amplitude (fourth and fifth plots), which finally reaches the boundary and gets out.

One can wonder where the small riddles in the last plots of both Fig. 5.5 and Fig. 5.6 come from. These look like partial reflections coming from the boundaries. The question is why these reflections arise at all if we are using maximally dissipative boundary conditions. Some insight can come from Fig. 5.7, where we have plotted the L_∞ norm of both Θ and Z_x (left and right plots, respectively. We see that there is an initial decreasing, corresponding to the phase when the original signal is expanding and passing through the boundaries. But then the decreasing stops, and a fixed level is attained, many orders of magnitude below the initial ones (the initial value for Z_x was actually zero, but a non-zero value is attained at the very first iteration). The

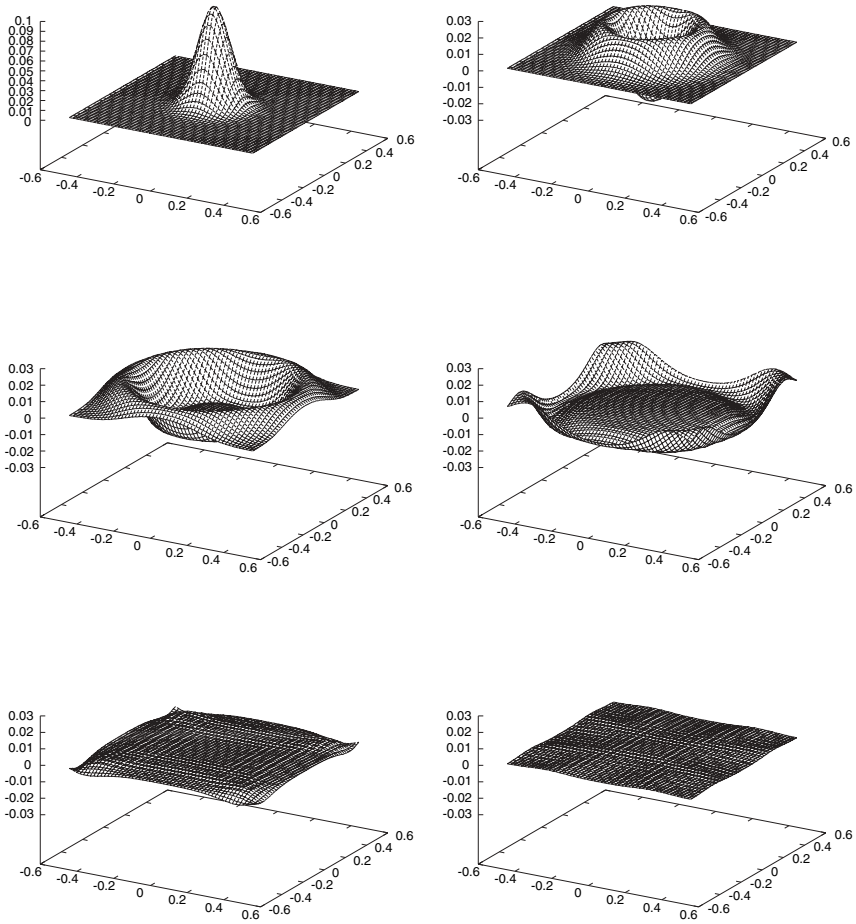

Fig. 5.5. Evolution of a initially static gaussian bump of Θ for flat (Minkowski) initial data. The sequence of plots goes from *left* to *right* and from *top* to *bottom*. The initial bump splits into two components. The outgoing one generates a circular wavefront that reaches the boundaries (*third plot*) and gets out. The incoming one passes through the origin (*second plot*), generating a second wavefront with negative amplitude (it can be seen in the *fourth plot*, contrasting with the zero-amplitude central region). This secondary wavefront finally reaches the boundary and gets out (*fifth plot*). Partial reflection can be detected, in the form of small riddles parallel to the boundaries, in the last two plots

lower limits appearing in Fig. 5.7 are not just due to numerical noise: the actual values depend on the combination of gauge and ordering parameters. This rather looks like a dynamical effect, due to the non-linear source terms in the evolution equations.

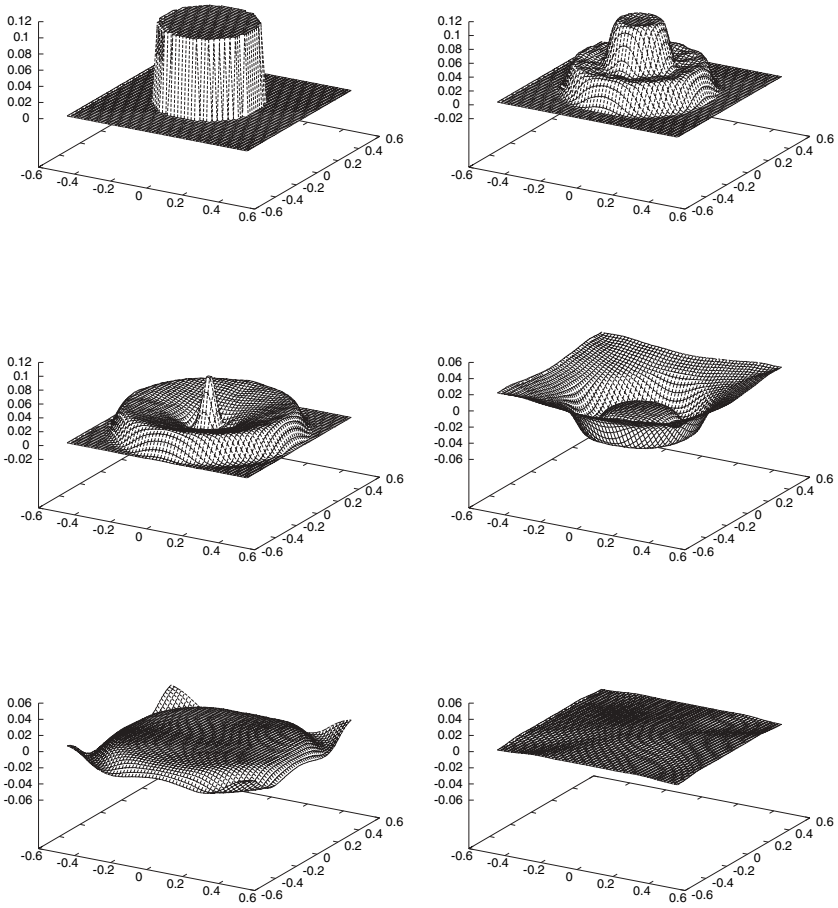

Fig. 5.6. Same of Fig. 5.5, but for an initial profile corresponding to a cylindrical step (*first plot*). The MMC numerical method is used here to deal with the initial discontinuity. The splitting between the incoming and outgoing wavefronts can now be seen more clearly (*second plot*). The outgoing wavefront reaches the boundary at about the same time that the incoming one gets to the origin (*third plot*). After crossing through the origin, the incoming wavefront starts propagating outwards with negative amplitude, leaving behind a zero-amplitude region (*fourth* and *fifth plots*). Notice again the residual riddles in the last plot

This test-bed is also an opportunity to check the common belief that numerical codes can support only a small amount of constraint violations, specially in the case of the Energy constraint. In the Z4 system, energy and momentum constraint violations are represented by non-zero values of the supplementary quantities (Θ , Z_i), respectively. As remarked before, the initial data contain values of Θ up to a 10% of the non-trivial metric coefficients without any sign of code instabilities.

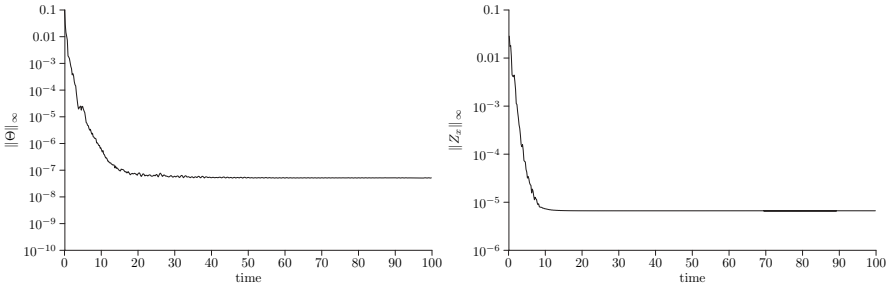

Fig. 5.7. L_∞ norm of both Θ and Z_x (*left* and *right plots*, respectively). There is an initial decreasing, corresponding tho the phase when the original signal is expanding and passing through the boundaries. A lower-limit level is attained in each case, many orders of magnitude below the initial one. These lower limits are not just due to numerical noise: the actual values depend on the combination of gauge and ordering parameters. The results shown here correspond to the choice ($\zeta = 0$, $f = 2$, $m = 0$)

5.3 Constraint-Preserving Boundary Conditions

The restrictions imposed by the maximally dissipative boundary conditions (5.29) are too strong to be physically realistic in most cases. One could only enforce these conditions, in asymptotically flat spacetimes, at spatial infinity. This can actually be the case if one devises a space coordinates transformation that assigns finite coordinate values to space infinity [50]: one needs just to make sure that the computational region extends up to these coordinate values and impose (5.10) there. This means that the numerical grid covers all the spatial slice surface, so that one can wonder whether there is still enough resolution in the strong-field fast-speed region if one has to cover also the rest of the space, up to infinity.

An alternative procedure is to keep using standard coordinates and to set up large numerical grids, so that the boundaries can be placed at the 'wave zone'. This means that one does not pretend to reach infinity, but just the far region where the dynamics can be consistently described as the propagation of outgoing waves in a stationary background. Maximally dissipative boundary conditions can not be applied in the form (5.10) to this case, because the time-independent background can be decomposed as a superposition of outgoing and incoming modes, and suppressing the latter would amount to destroying the background. In this wave-zone case, (5.10) can be generalized as

$$\partial_t \; w_r{}^{in} = 0 \; , \tag{5.55}$$

which would suppress only the time-dependent incoming modes, while preserving the stationary background, which will be determined by the initial data.

There are two weak points in this wave-zone boundaries strategy:

- From the practical point of view, large grids are computationally expensive. Putting the boundaries farther is competing with increasing the resolution in the highly dynamical zone, where it is really needed (but see [51, 52] for an interesting alternative).
- From the theoretical point of view, it can only be applied to the outer boundaries. Inner boundaries, like the ones arising after excising a space-time region (because it contains a singularity, for instance) would require a different treatment.

Our goal is to devise boundary conditions that could be applied even in the 'near zone', that is in the dynamical region. This means that the full complexity of the field equations must be taken into account, so that all the available information should be used in a consistent way. At this point, we should remember that the Z4 system contains four fields,

$$Z_\mu \Leftrightarrow \{\Theta\ ,\ Z_i\} \tag{5.56}$$

representing energy and momentum constraint violations. We know that these fields must vanish for true Einstein's solutions. In what follows, we will take advantage of this information in order to devise constraint-preserving boundary conditions that could be applied in the near zone.

5.3.1 The First-Order Subsidiary System

We have seen that the time evolution of the algebraic constraint (3.80) is given by the inhomogeneous wave equation

$$\Box\, Z_\mu + R_{\mu\nu} Z^\nu = 0\ . \tag{5.57}$$

It is of second order in Z_μ, so that the vanishing of both Z_μ and its first time derivatives is needed at the initial slice if we want to recover a true Einstein's solution.

But these initial data requirements will not be enough in the initial-boundary case. The principal part of (5.57) is precisely a set of uncoupled wave equations, one for every component of Z_μ. This means that we can consider again the standard decomposition into incoming and outgoing modes for every single component. It follows that non-zero values of the incoming modes at the boundaries would introduce constraint-violating modes into the computed solution.

To remedy this, we can write down the second order equations (5.57) as a first order system and impose then maximally dissipative boundary conditions on (the first derivatives of) the Z_μ components. In this way, the boundaries will behave as one-way membranes for constraint-violating modes. Any non-zero value of Z_μ, either contained into the initial data or arising from errors

during the numerical simulation, will find the way out of the computational region.

This sounds perfect, but there is a difficulty at the very beginning: we are dealing now with a first order system, so that there are additional ordering constraints (4.7, 4.9) to be allowed for. It follows that we can not just start from (5.57). We must instead go back to the first order equations for Θ and Z_i, respectively (4.19, 4.20), and take one extra time derivative to get the subsidiary system for the first-order version (4.14–4.20) of the Z4 system. Of course, we must add the time derivatives of the ordering constraints (4.7, 4.9), but these are trivially satisfied, so that only zero-speed modes are added to the system in this way.

We give here (the principal part of) the resulting subsidiary system

$$\partial_t \, [\partial_k \, A_l - \partial_l \, A_k] = 0 \tag{5.58}$$

$$\partial_t \, [\partial_k \, D_{lij} - \partial_l \, D_{kij}] = 0 \tag{5.59}$$

$$1/\alpha^2 \, \partial^2_{tt} \, \Theta - \triangle \, \Theta = \cdots \tag{5.60}$$

$$\begin{aligned} 1/\alpha^2 \, \partial^2_{tt} \, Z_i - \triangle \, Z_i = \frac{1}{2} \, \partial_k \, [\, \partial_i (A^k + D^k) - \partial^k (A_i + D_i) \\ + \, (\zeta - 1) \, (\partial_l D^{kl}{}_i - \partial^k E_i) + \, (\zeta + 1) \, (\partial_l D_i{}^{kl} - \partial_i E^k) \,] + \, \cdots \end{aligned} \tag{5.61}$$

(the dots stand for non-principal terms), and we can see in the right-hand-side of (5.61) the coupling terms with the ordering constraints which were not present in (5.57).

The subsidiary system (5.58–5.61) can be put in first order form in the usual way, by considering the first derivatives of (Θ, Z_i, A_i, D_{kij}) as new independent variables. The following evolution conditions

$$\partial_t \, (\partial_k \Theta) - \partial_k \, [\, \partial_t \Theta \,] = 0 \tag{5.62}$$

$$\partial_t \, (\partial_k Z_i) - \partial_k \, [\, \partial_t Z_i \,] = 0 \tag{5.63}$$

should be added then to complete (the first order version of) subsidiary system.

As anticipated, the light-cone structure of (5.57) is not changed by the coupling with the new zero-speed modes. One gets just some extra terms in the eigenfields. The vanishing of the incoming modes reads now

$$1/\alpha \, \partial_t \, \Theta^{(in)} + n^k \partial_k \, \Theta^{(in)} = 0 \tag{5.64}$$

$$\begin{aligned} 1/\alpha \, \partial_t \, Z_i^{(in)} + n^k \partial_k \, Z_i^{(in)} = -\frac{1}{2} \, n^k \, [\, \partial_i (A_k + D_k) - \partial_k (A_i + D_i) \\ - \, (1 - \zeta) \, (\partial_l D_{ki}{}^l - \partial_k E_i) + \, (1 + \zeta) \, (\partial_l D_{ik}{}^l - \partial_i E_k) \,] \, , \end{aligned} \tag{5.65}$$

where $\boldsymbol{n}$ is the outgoing unit normal to the boundary surface.

Notice that equations (5.64, 5.65) could alternatively be derived by imposing outgoing Sommerfeld conditions on (Θ, Z_i), that is setting the right-hand-side in (5.65) to zero, and then using the ordering constraints to 'trade'

longitudinal by transverse derivatives in the incoming modes of the evolution system, along the lines proposed in [53]. We have presented here a direct derivation from the Z4 evolution system, without any further adjustment.

Equations (5.64, 5.65) meet the two requirements we were looking for:

- They provide maximally-dissipative algebraic boundary conditions for the subsidiary system (5.58–5.63). In this way, no constraint-violating modes are allowed to enter across the boundaries.
- They provide (derivative) boundary conditions for the evolution system (4.14–4.20), which can be consistently imposed on true solutions of Einstein's field equations even in the near zone. Notice that the additional right-hand-side terms that have appeared in (5.65) also cancel out identically for a true Einstein solution.

Of course, there are only four equations in (5.64, 5.65), so that only four independent boundary conditions can be extracted. The remaining boundary conditions, corresponding to the gauge and the gravitational waves (transverse traceless) sector, must be provided separately, as we will see in what follows.

5.3.2 Computing the Incoming Fields

The computed values $(\Theta^{(in)},\ Z_i^{(in)})$ can be used now in order to compute four of the required incoming fields at the boundary. This process is not free from ambiguities. For the sake of clarity, we will recombine first the dynamical fields, so that the original basis

$$(\Theta\ ,\ K_{ij}\ ,\ Z_i\ ,\ D_{kij}\ ,\ A_i) \tag{5.66}$$

is replaced by

$$(\Theta\ ,\ \tilde{K}_{ij}\ ,\ V_i\ ,\ \tilde{D}_{kij}\ ,\ A_i)\ , \tag{5.67}$$

where we have defined

$$V_i = D_i - E_i - Z_i \tag{5.68}$$

$$\tilde{K}_{ij} = K_{ij} - \frac{\Theta}{2}\ \gamma_{ij}\ , \qquad \tilde{D}_{kij} = D_{kij} - \frac{1}{2}\ V_k\ \gamma_{ij}\ . \tag{5.69}$$

Note that the quantities Z_i do not appear explicitly in the new basis. They must be obtained instead from the new quantities $\tilde{D}_{kij}$ by using the algebraic identity

$$\tilde{D}_i - \tilde{E}_i = Z_i\ . \tag{5.70}$$

Note also that the 'combine before replacing' procedure that we are following here was yet the idea behind the symmetry-breaking mechanism we used in Sects. 3.4.4 and 4.1.4. The variable $\tilde{K}_{ij}$ was yet defined in (3.107) in a more general way: we are considering here just the $n = 1$ particular case. The new variable $\tilde{D}_{kij}$ is the natural companion of $\tilde{K}_{ij}$: its evolution equation would read (principal part only)

$$\partial_t\ \tilde{D}_{kij} + \partial_k\ [\ \alpha\ \tilde{K}_{ij}\ ] = \cdots\ . \tag{5.71}$$

The Z4 eigenfields obtained in Sect. 4.3.1 can be now, after some algebra, expressed in terms of the new basis, namely:

- **Standing eigenfields** (zero characteristic speed)

$$A_a,\ \tilde{D}_{aij},\ A_k - f\,\tilde{D}_k + f\left(m - \frac{3}{2}\right)\ V_k\ , \tag{5.72}$$

  where we will use here the indices a, b, c to label the components of the projections orthogonal to $\boldsymbol{n}$. Notice that the transverse components $\tilde{D}_{aij}$ are still zero-speed modes, allowing for (5.71).
- **Energy eigenfields**

$$E^{\pm} \equiv \theta \pm V^n \tag{5.73}$$

  (there is no change in this sector).
- **Metric eigenfields**

$$\tilde{L}_{ij}^{\pm} \equiv [\tilde{K}_{ij} - n_i n_j\ tr\,\tilde{K}] \pm [\tilde{\lambda}^n_{ij} - n_i n_j\ tr\,\tilde{\lambda}^n]\ , \tag{5.74}$$

  where we have noted

$$\tilde{\lambda}^k_{ij} \equiv \tilde{D}^k_{ij} + \frac{1}{2}\,\delta^k_i\left(A_j - \tilde{D}_j + \frac{1}{2}\ V_j\right) + \frac{1}{2}\,\delta^k_j\left(A_i - \tilde{D}_i + \frac{1}{2}\ V_i\right) - \frac{1+\zeta}{2}\,(\tilde{D}_{ij}{}^k + \tilde{D}_{ji}{}^k - \delta^k_i\tilde{E}_j - \delta^k_j\tilde{E}_i)\ . \tag{5.75}$$

  The notation $\tilde{L}_{ij}^{\pm}$ is to emphasize that the original modes $L_{ij}^{\pm}$ have been recombined with the Energy ones $E^{\pm}$, taking advantage of the degeneracy (all of them have light speed as characteristic speed).
- **Gauge eigenfields**. In the generic case ($f \neq 1$), we get

$$G^{\pm} \equiv \sqrt{f}\left[\ tr\,\tilde{K} + \left(\frac{3}{2} - \mu\right)\ \Theta\ \right] \pm [\ A^n + (2-\mu)\ V^n\ ]\ , \tag{5.76}$$

  where μ is defined by (4.81). In the degenerate case ($f = 1$, $m = 2$, arbitrary μ) the eigenfields can be chosen to be, for instance,

$$\left[\ tr\,\tilde{K} - \frac{1}{2}\ \Theta\ \right] \pm [\ A^n\ ]\ . \tag{5.77}$$

Now, it is clear that the incoming value of Θ, given by (5.64), can be used to provide the incoming eigenfield in the energy sector, namely

$$E^- = \Theta^{(in)} - V^n\ . \tag{5.78}$$

We can also compute in the same way the incoming metric eigenfields of mixed type, that is

$$\tilde{L}^-_{na} = \tilde{K}_{na} - \left[\tilde{D}^{(in)}_{nna} + \frac{1}{2} \left(A_a - \tilde{D}_a + \frac{1}{2} V_a \right) - \frac{1+\zeta}{2} \left(\tilde{D}_{ann} - \gamma^{bc} \tilde{D}_{bca} \right) \right] , \tag{5.79}$$

where the mixed components $\tilde{D}^{(in)}_{nna}$ can be computed from $Z^{(in)}_a$ allowing for (5.70), namely

$$\tilde{D}^{(in)}_{nna} = \tilde{D}_a - \gamma^{bc} \tilde{D}_{bca} - Z^{(in)}_a . \tag{5.80}$$

Finally, the trace of the transverse components of the incoming metric fields can be computed as

$$tr(\tilde{L}^-_{\perp\perp}) \;=\; \gamma^{bc} \left[\tilde{K}_{bc} - \tilde{D}^{(in)}_{nbc} + (1+\zeta)\, \tilde{D}_{bcn} \right] , \tag{5.81}$$

where, allowing again for (5.70), we have

$$\gamma^{bc} \tilde{D}^{(in)}_{nbc} = \gamma^{bc} \tilde{D}_{bcn} + Z^{(in)}_n . \tag{5.82}$$

As stated before, the four equations (5.64–5.65) do not provide enough information to determine the values of the transverse traceless incoming fields nor the gauge incoming eigenfield. We will keep using in these cases the safest generalization (5.55) of the maximally dissipative boundary conditions, namely

$$\partial_t\, G^- = 0 , \qquad \partial_t \left[\tilde{L}^-_{ab} - \frac{1}{2}\, tr(\tilde{L}^-_{\perp\perp})\, \gamma_{ab} \right] = 0 , \tag{5.83}$$

although we are aware that more sophisticated choices could be required in physical applications.

5.3.3 Stability of the Modified System

Let us summarize the results of the preceding section. The original evolution system is modified at the boundaries in such a way that the evolution equations for the incoming modes along the selected direction $\boldsymbol{n}$ take the form (principal part only):

$$1/\alpha\; \partial_t\; E^- = 0 \tag{5.84}$$

$$1/\alpha\; \partial_t\; \tilde{L}^-_{na} = -\partial_b \left[\tilde{D}^b{}_{na} - \tilde{D}_{na}{}^b + \frac{1-\zeta}{2}\, \tilde{K}_a{}^b \right] - \partial_a \left[\frac{1+\zeta}{2}\, \tilde{K}_{nn} + A_n + \frac{1}{2}\, V_n - \frac{f+1}{2}\, tr\tilde{K} - \frac{(3-2m)f+1}{4}\, \Theta \right] \tag{5.85}$$

$$1/\alpha\; \partial_t\; tr(\tilde{L}^-_{\perp\perp}) = -\partial_a \left[\gamma^{bc} \tilde{D}^s{}_{bc} + \tilde{D}_{nn}{}^a + \zeta\, \tilde{K}_n{}^a + A^a - \tilde{D}^a + \frac{1}{2}\, V^a \right] \tag{5.86}$$

plus the trivial evolution equations (5.83) for the gauge and the transverse traceless modes.

Notice that only transverse derivatives appear on the modified system equations (5.83–5.86) for the incoming modes. This means that the characteristic speeds along the longitudinal direction $\boldsymbol{n}$ are

$$\{0,\ \lambda^{out}\}\ , \tag{5.87}$$

and the modified system is (strongly) hyperbolic along $\boldsymbol{n}$.

Computing the characteristic speeds along a generic direction $\boldsymbol{r}$, oblique to $\boldsymbol{n}$ is a much harder task, even using an algebraic computing program. We have checked the particular cases

$$\zeta = 0\ ,\ \ \pm 1 \tag{5.88}$$

and we have found that the modified system is hyperbolic (real characteristic speeds) only in the $\zeta = 0$ case. Instead of reproducing here the derivation of this result, we will rather check it by using the robust stability test-bed.

To do this, we will proceed as in Sect. 5.2.2. We show in Fig. 5.8 the L_∞ norm of trK for different values of the ordering parameter ζ, so that we can directly compare with the analogous results for the algebraic boundary conditions case, as shown in Fig. 5.4. It follows that the constraint-preserving boundary conditions (5.84–5.86) are stable only for the $\zeta = 0$ choice, corresponding to a symmetric ordering of the space derivatives.

Notice that in our analysis we have just asked for real characteristic speeds (weak hyperbolicity), so that strong hyperbolicity is not ensured. We can

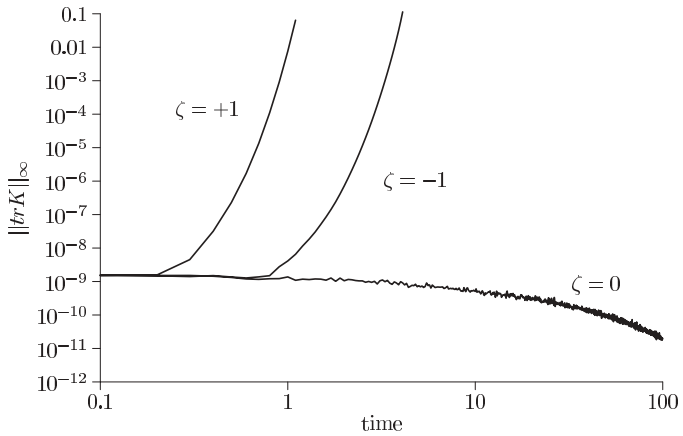

Fig. 5.8. L_∞ norm of trK for different values of the ordering parameter ζ and constraint-preserving boundary conditions along one single direction (periodic boundaries along the other two). Only the choice $\zeta = 0$ leads to a stable behavior. Even this choice gets unstable when the constraint-preserving conditions are applied to more than one direction, due to inconsistencies at the corner points.

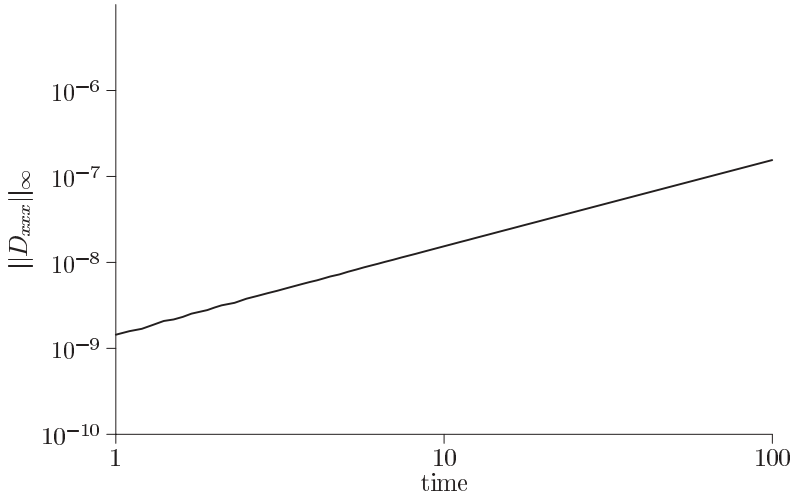

Fig. 5.9. Same as Fig. 5.8, but now for the L_∞ norm of D_{xxx} and $\zeta = 0$. A linear growing mode shows up, confirming that the modified system is just weakly, but not strongly, hyperbolic

actually see in Fig. 5.9 a growing linear mode in the L_∞ norm of some fields corresponding to space metric derivatives: this confirms that the modified system (5.83–5.86) is just weakly hyperbolic in the best ($\zeta = 0$) case.

Note also that the comparison with Fig. 5.4 is not exact. In Fig. 5.4, algebraic boundary conditions were imposed along every coordinate axis. In Figs. 5.8 and 5.9, constraint-preserving boundary conditions are imposed instead only along the x axis whereas periodic boundary conditions are used for dealing with the y and z directions.

We are not losing in this way the multi-dimensional character of the problem: the $x = constant$ boundary surfaces are actually surfaces, not just points, so that oblique modes are still present and can lead to instabilities, as it is actually the case when $\zeta = \pm 1$. The only thing we are avoiding in this way is to apply constraint-preserving boundary conditions to corner points (which are assigned to the y and z boundary surfaces, where periodic boundary conditions are applied). If we try to apply conditions (5.84–5.86) along every space direction, then instabilities appear even for the $\zeta = 0$ choice of the ordering parameter.

The problem at corner points comes from the inconsistency inherent to the choice of a (unique) normal direction there (see Fig. 5.2). Different faces get different normal vectors, but corner points belong to two different faces at the same time. This inconsistency does not lead to instabilities in the algebraic boundaries case, where we have some range of reflection coefficients to play with, and a clever choice of the normal direction at the corners allows one to be safely inside the stability domain of both faces at the same time.

But this is not the case for the boundary-preserving boundary conditions (5.84–5.86), where the adjustable reflection coefficients are replaced by precise conditions for many dynamical fields. This is a problem in practical applications, where more work should be done along any of the following lines:

- Devising an specific treatment for corner points, instead of just choosing a 'clever' value of $\boldsymbol{n}$.
- Building numerical grids with smooth boundaries (not just 'cartesian' ones), so that the constraint-preserving boundary conditions (5.84–5.86) can be applied consistently to the boundary surface in an stable way.

6

Black Hole Simulations

6.1 Black Hole Initial Data

The simplest Black Hole initial data can be obtained from the Schwarzschild line element. The 'Schwarzschild coordinates' expression (1.54), can be replaced by the 'isotropic coordinates' version

$$-\left(\frac{\rho - M/2}{\rho + M/2}\right)^2 dt^2 + \left(1 + \frac{M}{2\rho}\right)^4 \delta_{ij}\, dx^i dx^j \,, \tag{6.1}$$

which is better suited for the 3D case.

In order to start a numerical simulation, we must provide the initial values of every dynamical field (we assume here that we are using a first-order evolution system). As far as we are trying to get a true Einstein solution, these initial data can not be prescribed arbitrarily: the initial values of $(\gamma_{ij},\, K_{ij})$ must verify the energy and momentum constraints

$$\mathcal{E} \equiv \frac{1}{2}\left[\, tr\, R + (tr\, K)^2 - tr(K^2)\,\right] - \tau = 0 \tag{6.2}$$

$$\mathcal{M}_i \equiv \nabla_j\, (K_i{}^j - trK\ \delta_i{}^j) - S_i = 0\,. \tag{6.3}$$

This is true even if we are using the Z4 formalism, where we must also impose

$$\Theta = 0\,, \qquad Z_i = 0 \tag{6.4}$$

on the initial slice. The algebraic conditions (6.4) are not first integrals of the Z4 evolution system (4.14–4.20). Therefore, the vanishing of the first time derivative of (6.4) must also be imposed on the initial slice and, allowing for (4.19, 4.20) this amounts precisely to the energy and momentum constraints (6.2, 6.3). The second order subsidiary equation (3.81) ensures that no further conditions are required on the initial data in order to recover a true Einstein solution.

The easiest (but tricky) way of solving the initial-data constraints (6.2, 6.3) is just to take a $t = constant$ slice of a known exact solution of Einstein's

C. Bona and C. Palenzuela Luque: *Elements of Numerical Relativity*, Lect. Notes Phys. **673**, 119–143 (2005)
www.springerlink.com

field equations. If we do so with the isotropic form (6.1) of the Schwarzschild line element, we notice a number of features that can be then extrapolated to other (simple) sets of Black Hole initial data:

- It is a **vacuum** solution. This is good for testing just the geometrical sector of the numerical codes, independently of the hydrodynamical sector, where matter quantities should be computed from their own evolution equations.
- It is initially at rest (**time symmetric** initial data), that is

$$K_{ij} \mid_{t=0} \; = \; 0 \; . \tag{6.5}$$

  This means that the momentum constraint (6.3) automatically holds true. The energy constraint (6.2) gets the simpler form

$$tr\, R = 0 \tag{6.6}$$

- The space metric γ_{ij} is **conformally flat** (conformal to the Euclidean metric). This can be used in order to further simplify equation (6.6), as we will see in what follows.
- The space metric contains a **singularity**. This is the origin of the main complications we will face in this chapter, and this is why Black Hole simulations deserve an special treatment. In the Schwarzschild case, the singularity is located at the origin

$$\rho = 0 \; , \tag{6.7}$$

  where the space metric in (6.1) diverges. Notice that the line element (6.1) has also a coordinate singularity (vanishing of the lapse), which corresponds to the apparent horizon (6.10), as we will see below.
- There is an **apparent horizon**. It can be defined as the two-surface where outgoing light rays have zero expansion, that is

$$\theta = \nabla_k \, n^k + K_{ij} \, n^i n^j - trK = 0 \; , \tag{6.8}$$

  where $\boldsymbol{n}$ is here the outgoing unit normal to this two-surface (the wavefront). Quite surprisingly, only the dynamical field values at a given time slice are needed in order to locate the apparent horizon (which is a local, slicing-dependent feature). It follows from (6.8) that, for time-symmetric initial data, apparent horizons are also **minimal surfaces** (surfaces of minimal area), that is

$$\nabla_k n^k = 0 \; . \tag{6.9}$$

  In the Schwarzschild case, it is natural to consider spherical wavefronts. Allowing for (6.1, 6.9), the apparent horizon on the initial slice is the sphere given by

$$\rho = M/2 \; , \tag{6.10}$$

  which corresponds to $r = 2M$ in Schwarzschild coordinates.

In order to provide a geometrical interpretation of these features, we will analyze in more detail the Schwarzschild space metric in (6.1). Let us consider for instance the geometry of a plane passing through the origin. The two-dimensional metric for this plane can be written in polar coordinates as

$$d\sigma^2 = \left(1 + \frac{M}{2\rho}\right)^4 \left[\, d\rho^2 + \rho^2 d\varphi^2 \,\right]. \tag{6.11}$$

The line element (6.11) can also be considered as the metric of some two-dimensional surface in the three-dimensional Euclidean space. In this way, the geometry of the original plane in the Schwarzschild (curved) space is 'embedded' in Euclidean space, which is more familiar to everyone.

We have plotted in Fig. 6.1 the surface with metric (6.11) in flat space. Quite surprisingly, the singularity at $\rho = 0$ arises from the fact that the 'center' ($\rho = 0$) really corresponds to a spherical surface at space infinity. There is a minimal surface (corresponding to the minimal circle in the figure) at $\rho = M/2$, so that lower values of ρ lead back to circles of greater area. This minimal surface (the 'throat' in Fig. 6.1) coincides also with the location

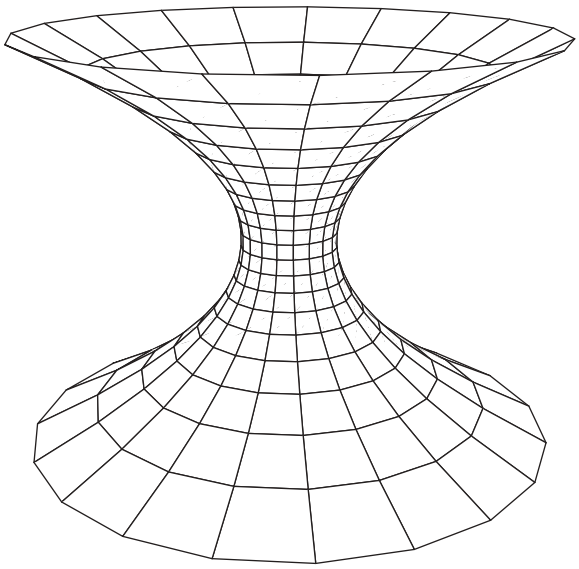

Fig. 6.1. Embedding of the Schwarzschild space metric as an ordinary surface in Euclidean spacetime. It is the revolution surface obtained from an horizontal parabola with vertex at the Schwarzschild radius ($\rho = M/2$ in isotropic coordinates). Radial lines beginning at infinity in the *upper side* come to the *center*, but reach a minimal circle at $\rho = M/2$ (the locus of the parabola vertices, seen as a 'throat' in the plot) and then go back by the lower side again to infinity. The singularity comes precisely from the counter-intuitive fact that $\rho = 0$ is not actually the center point, but it corresponds instead to a spherical surface placed at spatial infinity

of the apparent horizon in the initial (time-symmetric) slice, as it follows by comparing (6.8) with (6.9). The overall image is a sort of 'wormhole', where the interior geometry is just a replica of the exterior one.

6.1.1 Conformal Decomposition

The fact that the space metric in (6.1), namely

$$\left(1+\frac{M}{2\rho}\right)^4 \delta_{ij} \ , \tag{6.12}$$

is conformally flat suggests to consider the conformal decomposition of a generic three-dimensional metric:

$$\gamma_{ij} = e^{2U} \ \hat{\gamma}_{ij} \ , \tag{6.13}$$

where $\hat{\gamma}_{ij}$ is a given conformal metric (the Euclidean one in the Schwarzschild case).

The connection coefficients of the original and the conformal space metric are related by

$$\Gamma^k_{ij} = \widehat{\Gamma}^k_{ij} + \delta^k_{\ i} U_j + \delta^k_{\ j} U_i - U^k \hat{\gamma}_{ij} \ . \tag{6.14}$$

It follows that the corresponding Ricci tensors verify

$$R_{ij} = \widehat{R}_{ij} - \widehat{\nabla}_i U_j + U_i U_j - (\widehat{\nabla}_k U^k + U_k U^k)\, \hat{\gamma}_{ij} \ , \tag{6.15}$$

where the conformal metric is used in all index contractions. The corresponding relationship between both Ricci scalars is then

$$tr\, R = \widehat{tr}\, \widehat{R} - 4\, \widehat{\nabla}_k U^k - 2\, U_k U^k \ . \tag{6.16}$$

When the conformal metric $\hat{\gamma}_{ij}$ is flat, that is

$$\widehat{R}_{ij} = 0 \ , \tag{6.17}$$

it is convenient to express the conformal factor in (6.13) in the form

$$e^{2U} = \Psi^4 \ , \tag{6.18}$$

so that the vacuum time-symmetric Energy and Momentum constraints reduce to the Laplace equation on Ψ [4]

$$\widehat{\triangle}\ \Psi = 0 \ . \tag{6.19}$$

By a suitable choice of the space coordinates on the initial slice, one can always assume that the flat conformal metric takes the Euclidean form, namely

$$\hat{\gamma}_{ij} = \delta_{ij} \ . \tag{6.20}$$

The spherically symmetric solutions of (6.19) can then be obtained from

$$\partial_\rho \ [\ \rho^2\ \Psi_\rho\ ] = 0 \ , \tag{6.21}$$

so that one gets the Schwarzschild conformal factor in (6.12) as a result.

6.1.2 Singular Initial Data: Punctured Black Holes

We will consider here a class of initial data which is common to many Black Hole simulations:

- Time-symmetric, conformally flat initial slice, that is

$$K_{ij}\,|_{t=0} \;=\; 0\,, \qquad \gamma_{ij}\,|_{t=0} \;=\; \Psi^4\delta_{ij}\,, \tag{6.22}$$

  where Ψ is a solution of (6.19).
- Gauss initial gauge

$$\alpha\,|_{t=0} \;=\; 1\,, \qquad \beta^i\,|_{t=0} \;=\; 0\,. \tag{6.23}$$

- No extra fields on the initial slice. In the Z4 formalism, for instance,

$$\Theta\,|_{t=0} \;=\; 0\,, \qquad Z_i\,|_{t=0} \;=\; 0\,. \tag{6.24}$$

The problem of getting consistent initial data leading to true Einstein's solutions is then reduced to finding solutions of the three-dimensional Laplace equation (6.19) in the conformal Euclidean space.

This is exactly the same equation as that of the electrostatic potential in vacuum. We know that any non-trivial electrostatic potential is generated by some charge distribution. This means that the solutions Ψ of the vacuum Laplace equation will usually contain singularities, corresponding to the location of point charges acting as sources. We have yet seen this in the Schwarzschild case: the 'potential'

$$\Psi = 1 + \frac{M}{2\rho} \tag{6.25}$$

can be interpreted in electrostatic terms as a trivial (constant) contribution plus a Coulomb term at the origin.

It follows from these considerations that the Schwarzschild case is a good representative of Black Hole initial data, in the sense that 'puncture' singularities appear in the initial metric through the conformal factor Ψ (the term 'puncture' is actually suggested by the embedded geometry diagram in Fig. 6.1). Dealing with these singularities in numerical simulations is then the very first challenge.

The 'punctured Black Holes' approach [54,55,56] makes use of the conformal decomposition (6.13) to deal with this problem. We can summarize this method as follows:

- The conformal factor is assumed to be time-independent and identified with the initial (singular) conformal factor, that is

$$e^{2U} = \Psi^4\,|_{t=0}\;. \tag{6.26}$$

- Expressions (6.14, 6.15) are used for replacing the original ones in the evolution equations. The conformal factor and its derivatives are computed analytically from (6.26).
- As a result, the conformal metric $\hat{\gamma}_{ij}$ replaces the original one as the basic dynamical quantity (the same is true for its derivatives). In numerical simulations one computes $\hat{\gamma}_{ij}$ starting from the regular initial data

$$\hat{\gamma}_{ij} \mid_{t=0} \;=\; \delta_{ij} \; . \tag{6.27}$$

To summarize, the punctured Black Hole approach provides a clever way of dealing with singular initial data by computing analytically the singular contributions and numerically the regular ones. But the singularities are still there:

- Care must be taken to avoid placing any grid node at a singular point. Otherwise one would get infinite contributions from the analytical (singular) terms.
- Increasing grid resolution leads always to higher contributions from the (analytical) singular terms: convergence can not be achieved near a singular point.

This is why other approaches, dealing with regular initial data, have been considered.

6.1.3 Regular Initial Data

One can wonder wether it is possible at all to start a Black Hole simulation with regular initial data. The idea is to take advantage of the 'one-way membrane' paradigm: no physically meaningful information can get out from the horizon in a (classical) Black Hole. This means that one can modify the geometry of the interior region without affecting the exterior one, provided that it is done in a consistent way. One can use this idea to get rid of the unwanted interior singularities, as we will see below.

To be more precise, a number of comments are in order:

- The one-way membrane is not the apparent horizon (a local feature), but the event horizon, which can be defined as the boundary of the region which has no causal effect at infinity. This is a non-local feature (requires information from all future slices) although it can be computed numerically [57, 58]). However, as far as we know, the apparent horizon is interior to the event horizon, so that a safer strategy is to restrict any change to the interior of the apparent horizon, which can be easily located at any time slice.
- Gauge speed can be higher than light speed. This means that gauge modes can cross the horizon in both directions. However, this is not against the one-way membrane idea, because gauge conditions are not part of the field equations, nor carry any physically relevant information: one can choose them in a quite arbitrary way. Gauge modifications inside the horizon can

then be regarded just as one more way of determining the coordinate conditions.

- The stability of the numerical code requires that the numerical speed (3.37) be higher than the physical speed. It follows that numerical errors propagate faster than light and, then, they can also cross the horizon in both directions. Any change whatsoever in the interior region, must then be consistent and accurate if one wants the get a physically sound solution for the Black Hole exterior region.

Black Hole Excision

The most popular way of getting Black-Hole regular initial data is to excise any region, interior to some apparent horizons, that contains singular points [59]. This means that we are setting inner boundaries on our computational grid, and suitable boundary conditions must be provided there. The problem with inner boundary conditions is that they should hold in the strong-field high-speed region. This is in contrast with outer boundary conditions, which could in principle be placed in the weak-field zone, making things much easier.

One interesting possibility is to place the inner boundaries at minimal surfaces (the throat in Fig. 6.1). In the wormhole geometries we are considering, the interior region is just a replica of the exterior one. This is not so surprising if one remembers that the Laplace equation (6.19) is the one currently used in electrostatics, where the method of images provides precisely this kind of mirror-like solutions. In the Schwarzschild case, the inversion transformation

$$\rho \qquad \longleftrightarrow \qquad \frac{M^2}{4\rho} \tag{6.28}$$

leaves the spacetime metric (6.1) invariant.

The discrete mirror-like symmetry (6.28) allows one to set up 'virtual points' near the inner boundary by using just physical information from the grid nodes, without any extra input or assumption. After all, every point inside the throat is identical to another one outside, both related by (6.28). In the spherically symmetric case, this provides a nice way of excising the singular region which has been used successfully in Black Hole simulations [13, 23, 60].

In the generic three-dimensional case, however inner boundaries are not usually placed at the throats. The most common choice is to place the inner boundaries close to the (expanding) apparent horizon [61]. In contrast with the fixed throat location, apparent horizons are usually expanding with time. Inner boundaries are then forced to move during evolution, departing from their initial location at the throat. This makes the whole issue much more complicated:

- The apparent horizon surface must be located in real time, not just for tracking purposes, but in order to determine wether the inner boundary needs to be further expanded or not.

- Moving the inner boundary to the next grid point may cause numerical jumps that must be kept under control.
- Most important: the region behind the inner boundary is no longer a replica of the exterior one, so that one must provide physically sound and numerically stable boundary conditions there.

Stuffed Black Holes

Regular initial data can also be obtained without introducing internal boundaries. The idea comes once more from the electrostatic analogy suggested by (6.19), which we will write here in the non-vacuum case as

$$\widehat{\triangle}\,\Psi = -\frac{1}{4}\,\tau\,\Psi^5\,. \tag{6.29}$$

It is well known that the external (Coulomb) field of a spherical charge distribution is the same as the one generated by a point charge. In the same way, the exterior Schwarzschild geometry is the same as the one generated by a interior matter distribution with the same total mass.

The idea is then to match the Schwarzschild exterior space metric with a (non-singular) interior space metric corresponding to some matter distribution ('stuffed' Black Holes [62]). The easiest choice is again that of a conformally flat metric with a conformal factor verifying (6.29). The matching must be made precisely at the throat of the vacuum solution to make sure that

- The exterior geometry is fully preserved. This means that the matching can not be made outside the throat.
- There is no 'shell crossing', so the minimal surface is not actually a local minimum of the surface area. This means that the matching can not be made inside the throat.

In the Schwarzschild case, the simplest example of this minimal-surface matching of a non-vacuum interior metric is provided by the well known Friedman-Robertson-Walker space metric (1.50) in the 'closed' case ($k = +1$). In isotropic coordinates, the resulting conformal factor can be expressed as:

$$\Psi^4 \;=\; \begin{array}{ll} (1+\frac{M}{2\rho})^4 & \rho \geq \frac{M}{2} \\ 64\,[\,1+(\frac{2\rho}{M})^2\,]^{-2} & \rho < \frac{M}{2}\,, \end{array} \tag{6.30}$$

so that we get a constant interior distribution of energy density on the initial slice, that is

$$\tau \;=\; \begin{array}{ll} 0 & \rho > \frac{M}{2} \\ 3/4\;M^{-2} & \rho < \frac{M}{2}\,. \end{array} \tag{6.31}$$

The resulting composite geometry can be better understood by looking at Fig. 6.2, where the corresponding line element is embedded in Euclidean

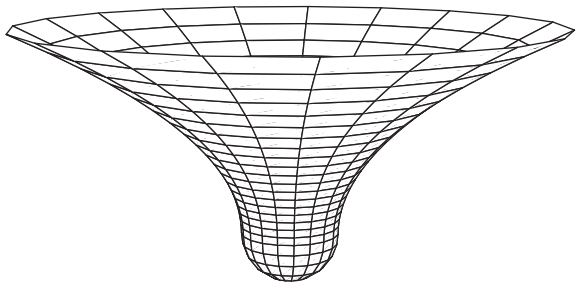

Fig. 6.2. Same as Fig. 6.1, but with the *lower* part replaced by the embedding of the (*closed*) Friedman-Robertson-Walker line element, which is a half-sphere. Both parts match smoothly at the Schwarzschild radius, so that the locus of the parabola vertices coincides with the equator of the sphere. The resulting composite geometry is perfectly regular and the radial lines coming from infinity can reach without problems the center, which corresponds now to $\rho = 0$

space, as we did in Fig. 6.1 for the wormhole case. There is no singularity of any kind. The radial coordinate extends now from the center to spatial infinity. The area of spherical surfaces increases monotonically with their radius, so that there is no shell crossing.

Explicit expressions have been provided for time-symmetric initial configurations containing an arbitrary number of stuffed Black Holes with arbitrary masses [62]. Robust 3D numerical simulations have also been performed by using a second order formalism which is a mixture of the Bona-Massó and the BSSN ones [26]. But remember that there is a price to pay for this:

- The (dust) matter inside the holes must be evolved consistently.
- Although the first derivatives are continuous at the matching surfaces, second derivatives are not, so that standard numerical methods may have problems there.

Free Black Holes

An even simpler alternative is possible in the framework of the Z4 formalism. In this case, the energy and momentum constraint violations are represented by the supplementary dynamical fields

$$Z_\mu \Leftrightarrow (\Theta,\ Z_k)\ . \tag{6.32}$$

As far as non-zero values of these fields can be evolved without problems, we can conclude that the Z4 formalism is tolerant to energy and momentum constraint violations.

Moreover, we know that both Θ and Z_k can be computed from light cone eigenfields, with light speed as characteristic speed. It follows that non-zero values of these supplementary fields in the initial data would propagate

along light cones. In the region exterior to the Black Hole, the outgoing part will reach the outer boundary and (provided that we are using constraint-preserving boundary conditions) will finally leave out the computational region. The incoming part will instead cross the horizon, entering the interior region. As far as nothing travelling with light speed can get out the Black Hole interior, non-zero values of Θ and Z_k will cumulate there.

Playing again with the idea that the interior region has no causal physical influence on the exterior one, we can devise a simple way of obtaining regular initial data without either using excision or stuffing:

- Use the physical initial data (the ones verifying the energy and momentum constraints) in the exterior region. This part is common to either the excising and the stuffing methods.
- Forget about the energy and momentum constraints in the interior region ('Free Black Holes'). Just take there any regular and smooth extension of the exterior geometry.

As a consequence, allowing for the corresponding evolution equations (4.19, 4.20), non-zero values of Θ and Z_k will start appearing and cumulating in the Black Hole interior. But, as we will see later, this poses no problem to numerical simulations in the Z4 formalism.

In the Schwarzschild case, one can take for instance the smooth conformal factor (6.30) (see Fig. 6.3), but now in the context of a fully vacuum metric,

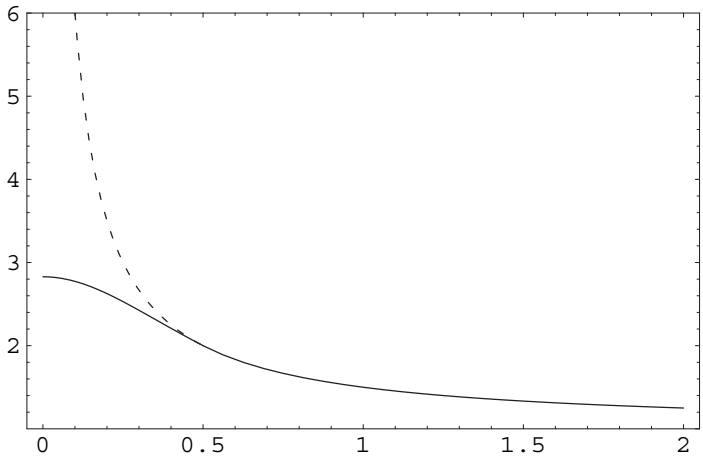

Fig. 6.3. Plot of a conformal factor Ψ providing time-symmetric conformally-flat initial data for a free Schwarzschild Black Hole. Values on the x axis correspond to the isotropic radial coordinate ρ, measured in units of M. The singular expression (6.25) in the interior region (*dashed line*) is replaced by a regular one (*continuous line*). In this case we have taken (6.30), just as an instance. Both expressions coincide in the exterior region. Notice that the matching is smooth at the apparent horizon ($\rho = M/2$)

so that the energy constraint (6.19) is no longer fulfilled in the interior region. Alternatively, we can take any other smooth continuation of the exterior conformal factor to the interior region.

This approach is different from that of the matching problem (finding a suitable interior solution for a given exterior three-metric), which was that of the previous section. Here, one just extends smoothly the exterior geometry without imposing any constraint to the interior part. Only regularity conditions must be required.

6.2 Coordinate Conditions

One can wonder why to choose Black-Hole regular initial data if singularities will appear anyway during time evolution. This is a good point. In the stuffed Black Hole case (6.30), for instance, the interior region is filled with dust fluid, which will collapse by its own gravity to a singularity (there is no opposing force, not even pressure, to prevent this) in a finite amount of proper time.

Collapse singularities arise when two nearby, but different, time lines (the world lines of two different Eulerian observers) meet at the very same point. Then, the proper distance between these time lines, which are labelled with different space coordinates, vanishes. This means that the space metric is no longer invertible there (the space volume element $\sqrt{\gamma}$ vanishes). Of course, this would be fatal for a numerical simulation, which will crash when trying to compute the (divergent) components of the inverse space metric.

This behavior is generic in Black-Hole spacetimes. Remember that the apparent horizon is defined as the surface for which the expansion of a outgoing congruence of light rays vanishes (6.8). This expansion is then negative inside the apparent horizon, meaning that even outgoing light rays are actually collapsing. As far as the time slices are space-like hypersurfaces, their normal lines (the world lines of the Eulerian observers) are time-like, that is interior to the local light cones. It follows that the expansion of the Eulerian observers (2.29) must also be negative, that is (2.32)

$$\theta < 0 \;\Leftrightarrow\; trK > 0\,, \tag{6.33}$$

inside the apparent horizon, so that the normal lines are actually collapsing.

6.2.1 Singularity Avoidance

We have seen in Sect. 2.1.2 how coordinate time (the time label that our computer is using when proceeding from one time slice to the next) is related with proper time through the lapse function α. The idea is to slow down the evolution, by choosing smaller values of α, in the regions that are going to collapse, whereas keeping constant values of α in the outer regions, where information about the collapse can actually be recovered. The sequence of

time slices would then cover most of the outer region, while keeping safely away from the singularity which is going to form inside the Black Hole (see Fig. 2.1 for a schematic representation).

Let us be more precise. Let us choose the normal time line corresponding any fixed point x_0 on the initial slice (normal coordinates). Let us suppose now that this time line is going to meet a collapse singularity in a finite amount of proper time, that is

$$\sqrt{\gamma} \to 0 \qquad \text{for} \qquad \tau \to \tau_S \ . \tag{6.34}$$

The coordinate time elapsed in the process is then given by

$$\Delta t = \int_0^{\tau_S} \frac{d\tau'}{\alpha} \ . \tag{6.35}$$

A necessary condition for the singularity to be avoided is that (6.35) be an improper integral, because the result is the coordinate time at which the singularity will actually occur. This means that the lapse function α should 'collapse' to zero, that is

$$\alpha \to 0 \qquad \text{for} \qquad \tau \to \tau_L \leq \tau_S \ . \tag{6.36}$$

Otherwise, it is clear that the singularity will be attained in a finite amount of coordinate time.

We will assume for the moment that the lapse collapses precisely at the singular point, that is

$$\tau_L = \tau_S \tag{6.37}$$

(the case $\tau_L < \tau_S$ will be considered in the next section). In this case, singularity avoidance is achieved if and only if the improper integral (6.35) diverges, so that the singularity is not attained in a finite amount of coordinate time. We can put this condition in an equivalent differential form: the improper integral (6.35) will diverge if and only if the proper time derivative of the lapse does have a finite value at the singularity, namely

$$\partial_\tau \, \alpha \, |_{\tau=\tau_S} = \lim \left(\frac{\alpha}{\tau - \tau_S} \right) < \infty \ . \tag{6.38}$$

We can check this condition for the class of generalized harmonic slicing conditions (3.90) that we are considering here,

$$\partial_\tau \, \alpha = -f \alpha \, tr \, K \tag{6.39}$$

(remember that $\Theta = 0$ for true Einstein's solutions), which we know that leads to strongly hyperbolic evolution systems for $f > 0$. It follows that singularity avoidance will be achieved in our case if and only if

$$f \alpha \, tr \, K \, |_{\tau=\tau_S} \ < \ \infty \ . \tag{6.40}$$

We can still refine a little bit more our analysis by assuming that

$$\partial_\tau \sqrt{\gamma} \; < \; \infty \; . \tag{6.41}$$

This means that we are dealing just with ordinary collapse singularities ('focusing singularities' in [63]), and not with stronger singularities in which the space volume element could vanish at an infinite proper-time rate. It follows that, for generalized harmonic slicing, singularity avoidance is achieved if and only if either there is a limit surface or

$$\frac{f\alpha}{\sqrt{\gamma}} \; < \; \infty \; . \tag{6.42}$$

Simple examples of singularity avoidance are provided by the choice $f = n$ (constant), which is currently used in numerical simulations. In that case condition (6.39) can be easily integrated to give

$$\alpha/\alpha_0 = (\gamma/\gamma_0)^{n/2} \; , \tag{6.43}$$

so that the lapse is collapsing precisely at the singular point, where the space volume element is vanishing (no limit surface appears). Allowing for (6.42), the singularity will not be reached in a finite amount of coordinate time if and only if

$$n \geq 1 \; . \tag{6.44}$$

The case $n = 1$ corresponds to the original harmonic slicing condition, which verifies (6.44) marginally. This is why higher values, like $n = 2$ are preferred in Black Hole numerical applications: they lead to more robust simulations.

6.2.2 Limit Surfaces

Another preferred choice in Black Hole numerical simulations is given by the generalized '1+log' slicing condition $f = n/\alpha$. Condition (6.39) can be easily integrated again to give

$$\alpha - \alpha_0 = \frac{n}{2} \; ln(\gamma/\gamma_0) \; , \tag{6.45}$$

which justifies the '1+log' name (the initial lapse is usually taken to be one). Notice that the lapse is collapsing here even before the singular point is reached, at a surface defined by

$$\gamma = \gamma_L \equiv \gamma_0 \; \exp\left(-\frac{2\alpha_0}{n}\right) > 0 \; . \tag{6.46}$$

This is a first example of a limit surface. It occurs when and where the lapse collapse occurs before the metric collapse, that is

$$\tau_L \; < \; \tau_S \; . \tag{6.47}$$

The final slice is then bounded away from the singularity, so that we can assume that both the space metric and the extrinsic curvature are regular tensors there. It follows that condition (6.42) can be replaced by

$$f\alpha\,|_{\alpha=0} \;<\; \infty\,. \tag{6.48}$$

This would imply that the limit surface will not be reached in a finite amount of coordinate time.

Hitting the limit surface, however, would not be a big problem, provided one avoids crossing the line and running into negative lapse values. Anyway, one must be very careful in order to avoid the divergence of some gauge-related quantities, that could crash the numerical simulations:

- By rescaling some dynamical fields. The ordinary space derivative of the lapse
$$a_k \equiv \alpha\; A_k \tag{6.49}$$
could be used instead of the logarithmic one A_k. Also, the rescaled gauge factor
$$\tilde{f} = f\alpha^2 \tag{6.50}$$
could be used instead of the original one, and so on.
- By implementing some mechanism in the numerical code that avoids running into negative lapse values. The idea is to freeze the evolution of the set $\mathbf{u}$ of dynamical fields once the limit surface has been reached.

A completely different example of slicing condition leading to a limit surface is provided by the maximal slicing condition (2.95), that is

$$trK = -\,\partial_\tau\; ln(\sqrt{\gamma}) = 0\,, \tag{6.51}$$

so that the space volume element is not even allowed to depart from its initial value. In the Schwarzschild case, maximal slicing is known to produce a limit surface given by [64]

$$r = r_L \equiv\; 3M/2 \;>\; 0\,, \tag{6.52}$$

where r is the Schwarzschild 'radial' coordinate, which is actually a time coordinate inside the horizon ($r = 2M$), so that (6.52) corresponds to a regular spacelike hypersurface, bounded away from the $r = 0$ singularity.

We have seen that, when using maximal slicing, the lapse function must be computed by solving an elliptic differential equation (2.96), and this is why we have not considered it in the context of the hyperbolic evolution formalisms that appeared in the 1990's. Before these dates, maximal slicing was currently used in numerical simulations [12] mainly because of its excellent singularity avoidance properties. It was actually the slicing of choice in the first 3D colliding Black Hole simulations [13].

6.2.3 Gauge Pathologies

One can wonder whether singularity avoidant slicing conditions can have some unwanted side effects. From the theoretical point of view, it is clear that the direct relationship (6.39) between (the proper time variations of) the lapse and the volume element will be helpful in the collapse scenario (6.33), where the lapse diminishes in response to the positivity of trK.

But, conversely, this will make the lapse function to increase in the zones which, for any reason, are expanding so that trK becomes negative. We will have then a sort of 'runaway' solution, with the time slicing accelerating precisely in the expanding regions. The lapse could grow then without limit, leading to a gauge blowup, as we will see in the following section.

Gauge instabilities have also been studied from another perspective (see [65,66], although a coordinate-dependent definition of velocity is used instead of ours). The idea is that gauge characteristic speeds

$$v_G = \pm\, \alpha \sqrt{f} \tag{6.53}$$

depend actually on the lapse, which is dynamically related through its evolution equation (3.90) with the corresponding gauge eigenvectors. Allowing for this dependence, transport-related pathologies ('gauge shocks') have been predicted to occur unless

$$\tilde{f}' = 2\alpha \ , \tag{6.54}$$

where we have noted again $\tilde{f} \equiv f\alpha^2$ and the prime is the derivative with respect to α.

That dependence, however, is indirect, coming only from the source term in the lapse evolution equation (3.90). In order to analyze this point in more detail, let us take the time derivative of (3.90). Allowing for the Z4 evolution equations, we get after some algebra

$$\begin{aligned}(1/\tilde{f})\ \partial^2_{tt}\ \alpha - \triangle\ \alpha = & - \left[\alpha\ tr\,(K^2) - \tilde{f}'\ (trK - m\Theta)^2 + \frac{\alpha}{2}\ (\tau + \ trS)\right] \\ & - \alpha\ \left(1 - \frac{m}{2}\right)\ [\ trR + 2\nabla Z - tr(K^2) + (trK - 2\Theta)\ trK - 2\tau\ ] \\ & + m\ Z^k a_k \ ,\end{aligned} \tag{6.55}$$

where we have taken the parameter m as a constant.

As far as all the evolution formalisms share the same Einstein's solutions, we can simplify our analysis by switching to the BSSN formulation, so that (6.55) takes the simpler form [66]:

$$(1/\tilde{f})\ \partial^2_{tt}\ \alpha - \triangle\ \alpha = -\ [\ \alpha\ tr\,(K^2) - \tilde{f}'\ (trK)^2\ ] - \frac{\alpha}{2}\ (\tau + \ trS)\ , \tag{6.56}$$

which amounts here to take $m = 2$ and making Θ and Z_k to vanish in (6.55).

Now we can introduce a 'gauge characteristic time' λ, defined locally by

$$\Delta\lambda \equiv \alpha \sqrt{f}\, \Delta t\ . \tag{6.57}$$

The corresponding time derivative operator is given by

$$D_\lambda \equiv \frac{1}{\alpha\sqrt{f}}\, \partial_t\ . \tag{6.58}$$

This allows one to write the principal part of (6.56) in the form

$$D_\lambda^2\, \alpha - \triangle\, \alpha = -\ \left[\alpha\ tr(K^2) - \frac{\tilde{f}'}{2}\ (trK)^2\right] - \frac{\alpha}{2}\ (\tau + \ trS)\ , \tag{6.59}$$

which can be interpreted as an inhomogeneous wave equation. The left-hand-side describes just transport with constant propagation speed, when measured in terms of length per gauge time intervals. The right-hand-side (source) terms are of two types:

- **Matter terms**
$$-\ \frac{\alpha}{2}\ (\tau + \ trS)\ , \tag{6.60}$$
which will contribute to the lapse collapse in the physically sound case, when both the matter density and the pressure are positive.
- **Kinetic terms**
$$-\ \ \alpha\ tr(K^2) + \frac{\tilde{f}'}{2}\ (trK)^2\ , \tag{6.61}$$
which will contribute either to the lapse collapse or to a lapse rebound, depending on the value of $\tilde{f}'$.

Let us discuss the behavior of these source terms. A lapse blowup could appear in the solution whenever the kinetic terms (6.61) have a positive value which is not compensated by the matter terms. Condition (6.54) amounts actually to require the exact cancellation of (6.61) in the one-dimensional case.

In the three-dimensional case, it is convenient to decompose the extrinsic curvature tensor K_{ij} into its irreducible components, namely

$$A_{ij} \equiv K_{ij} - \frac{trK}{3}\ \gamma_{ij}\ , \qquad K \equiv trK \tag{6.62}$$

(shear tensor and expansion factor, respectively), in order to express the kinetic terms (6.61) as

$$-\ \alpha\ tr(A^2) + \left(\frac{\tilde{f}'}{2} - \frac{\alpha}{3}\right)\ K^2\ , \tag{6.63}$$

so that a sufficient condition for avoiding the lapse blowup would be

$$\tilde{f}' \leq \frac{2\alpha}{3} \ . \tag{6.64}$$

Notice however that the condition (6.64) is derived just from the tr^2K source terms in the original equation (6.55). Their effect can be compensated by other source terms, so that the violation of (6.64) does not imply necessarily a lapse blowup.

Our conclusion is that any pathological behavior of the gauge-dependent degrees of freedom, which manifests itself as an blowup of either the lapse function or its first derivatives, can be interpreted consistently as the combined effect of the non-linear source terms in the evolution equations, independently of their origin. This prediction is confirmed by the simple numerical Black-Hole simulations presented in the following section.

6.3 Numerical Black Hole Milestones

We will present in this section the results of applying the techniques discussed so far to Black Hole simulations. The idea is to choose a simple example and to follow it in a step-by-step way. We will therefore avoid unnecessary complications and go directly to the hearth of the problem, where much insight can be gained. The natural choice is that of a single Schwarzschild Black Hole, because it is the simpler one that shows the first difficulties that we will encounter in generic Black Hole simulations.

There are some decisions to take at the very beginning. These are our choices:

- **Evolution system**: The first order version (4.14–4.20) of the Z4 system
- **Numerical algorithm**: The Method of Lines, with Finite-differences Flux-conservative discretization. We will keep two options open for the crucial choice of the interface Fluxes: the standard centered Flux (4.61) and the MMC method, as described in Sect. 4.3.2.
- **Boundary conditions**: Maximally-dissipative algebraic conditions at the outer boundaries, as described in Sect. 5.2.
- **Initial data**: Free Black Hole initial data (6.22–6.24).
- **Coordinate conditions**: Singularity avoidant slicing, given by the algebraic condition (4.5), with zero shift. We keep all options open for the values of the gauge parameters f and m.

In keeping with the philosophy of this section, we will restrict ourselves to modest-size simulations that can be performed in any personal computer. This implies using small numerical grids of, let us say, 60^3 nodes and being ready for overnight calculations in the worst case.

Even if we are using cartesian 3D coordinates for a spherically symmetric problem, we can take advantage of some discrete space symmetries. The initial data are mirror-symmetric across every coordinate plane. This Octant

Symmetry is preserved by the evolution equations, and this allows us to compute just over one octant of the spacetime domain. To illustrate how it can be done, let us focus for instance on the mirror symmetry across the z plane:

- We must classify every dynamical field as being either even or odd under the transformation
$$z \quad \longleftrightarrow \quad -z \, . \tag{6.65}$$
- We can then replace the negative z region of the numerical grid by a single layer of mirror points.
- The dynamical fields values at these mirror points are defined to be the same ones as the corresponding ones in the first layer of the positive z region: the sign of the odd fields is just reversed.

Octant symmetry allows us to double space resolution (that is a factor 8 in memory space) for a given grid size. In our case, we will put the outer boundary at about $\rho = 6M$, which is definitely too close, in order to get a reasonable resolution, that is

$$\Delta x = \Delta y = \Delta z = 0.1M \, . \tag{6.66}$$

Notice that a value of $6M$ along the coordinate axes means about $10M$ along the cube diagonals, which is the cut that we will show, unless otherwise stated, in the figures that follow. This will be enough to begin with.

6.3.1 Lapse Collapse and Landing ($0 - 5M$)

The first stages of the simulation show a collapse of the space volume element which, allowing for the singularity avoidance properties of the gauge conditions discussed in this chapter, translates itself into a collapse of the lapse function α. This lapse collapse can be slower or faster, depending on our choice of gauge parameters.

We show in Fig. 6.4 the lapse collapse for different choices of the gauge parameter f. The pattern is very similar: a fast collapse at the beginning (the lines shown are evenly spaced in time), followed by a slowing down and eventually 'landing' very close to a zero value in the innermost region, which means that the dynamics gets locally frozen there.

This is the first milestone in a Black Hole simulation. We have not shown the equivalent results for the harmonic slicing case because our code crashed before reaching that point. Notice that this was just the limit case at which the slicing still should manage to avoid the singularity at the continuum level. In our case, numerical errors make the code to cross the line and the singularity is not avoided at the discrete level. Of course, different numerical algorithms could make numerical errors go into the opposite sense. But we will try to avoid here this kind of 'fine tuning', following instead more robust alternatives when available.

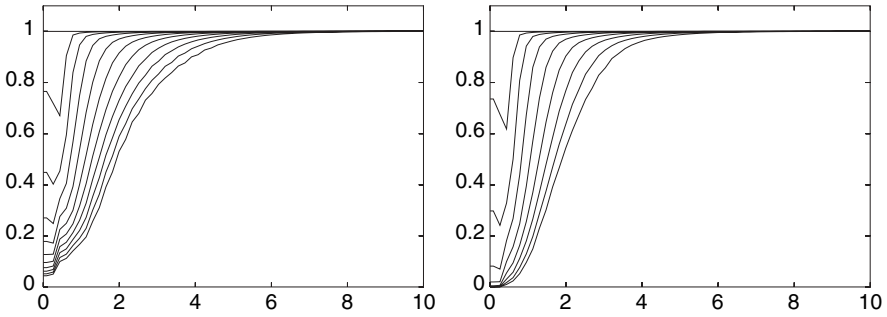

Fig. 6.4. Lapse collapse for different slicing conditions: the lapse values are shown every $0.5M$. The *left panel* corresponds to the $f = 2$ slicing, which has no limit surface. Notice that the lapse is still away from zero in the last plot ($t = 5M$). The *right panel* shows the same thing for the $f = 2/\alpha$ slicing, which does have a limit surface. The lapse collapses faster here, so that it gets very close to zero in the innermost region, as it can be seen in the last plot ($t = 4M$)

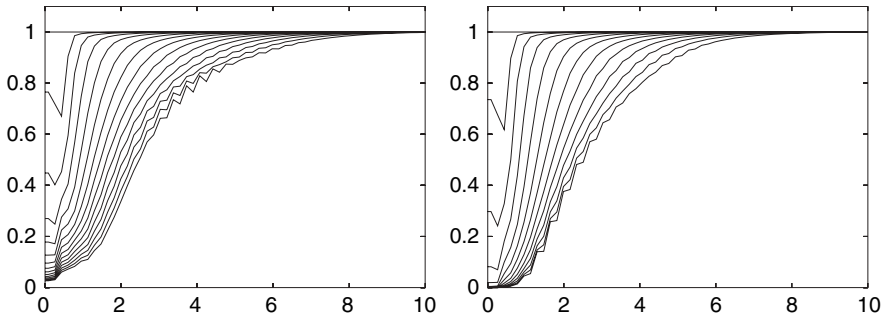

Fig. 6.5. Same as Fig. 6.4, but with the simulations running for a longer time ($t = 7M$ in the *left panel* and $t = 6M$ in the *right* one). Spurious oscillations appear in the zones where the slope is changing more abruptly. This suggests that these zones are poorly resolved by the standard finite difference method

Let us see what happens when allowing our simulations to proceed for a longer time. We see in Fig. 6.5 how spurious oscillations start appearing in the regions where the lapse slope is changing more abruptly. This is a numerical artifact: the appearance of such oscillations can be delayed by improving the space resolution (but keeping all the remaining parameters fixed). This is why we qualify these oscillations as spurious: they are a symptom of some lack of resolution that appears dynamically (and gets worse) during the simulation.

6.3.2 Slice Stretching ($3 - 20M$)

More insight can be gained by taking a look to Fig. 6.6.

We see that trK is positive at that time (about $6M$ in our case), so that we have an overall collapse pattern. But if we look at a radial component

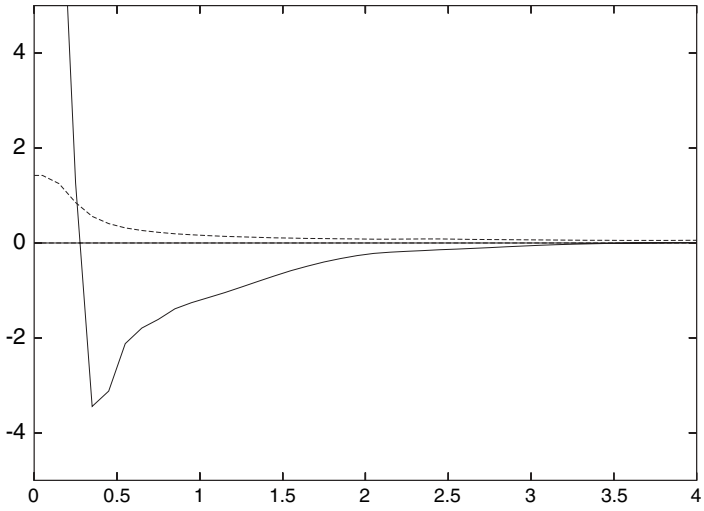

Fig. 6.6. Plots of K_{xx} (*solid line*) and trK (*dotted line*) along the x axis, corresponding to the $f = 2/\alpha$ slicing at $t = 6M$. Negative values of K_{xx} correspond to the increasing of γ_{xx}, that is a radial stretching of the time slice. Notice that this is compatible with an overall collapse pattern, as shown by the positivity of trK: the radial stretching is then compensated by the collapse along the angular directions. Slice stretching is at the origin of the growing lack of resolution which causes the spurious oscillations shown in Fig. 6.5

(K_{xx} along the x direction for instance), we see that radial directions are actually expanding. The geometrical meaning of this behavior can be better understood by looking at the wormhole embedding diagram in Fig. 6.1. The radial expansion can be interpreted as the 'stretching' of the throat by pulling up from the top. This stretching is accompanied by the shrinking of the throat perimeter (the spherical surface area in the 3D case). The total effect on the space volume element is that of a highly inhomogeneous collapse. The radial expansion is at the origin of the lack of resolution which causes the numerical oscillations in Fig. 6.5.

An unwanted numerical effect can be corrected by using better numerical techniques. We show in Fig. 6.7 exactly the same simulations as in Fig. 6.5, but now using the MMC method, as described in Sect. 4.3.2. There is no trace of the oscillations. This is the second milestone we find in Black Hole simulations: getting rid of the spurious oscillations due to slice stretching. The way we have done it is by not means unique: similar results could be achieved by adding suitable fourth-order dissipative terms to the numerical algorithm [19].

Notice however that slice stretching is a dynamical feature that is still there, independently of the numerical algorithm one is using. In fact, the plots in Fig. 6.6 where obtained using the MMC method instead of the standard centered one (probably you have suspected it by the smoothness of the plot).

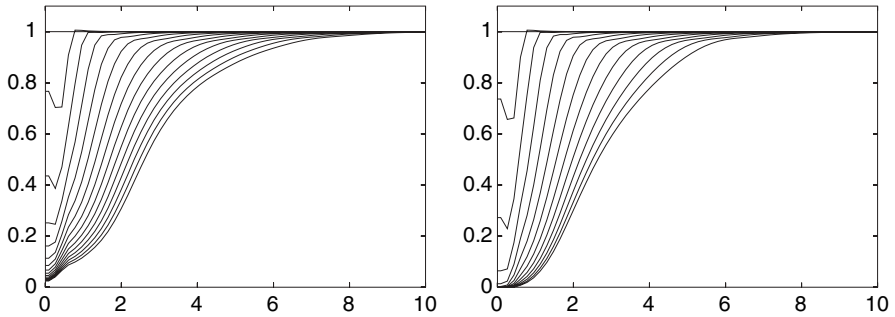

Fig. 6.7. Same as Fig. 6.5, but using the MMC numerical algorithm for the space discretization, as described in Chap. 5. The spurious oscillations have completely disappeared. Slice stretching is still there (Fig. 6.6 corresponds actually to the last plot in the *right panel*), but it is no longer a problem for numerical simulations

6.3.3 Lapse Rebound ($10 - 30M$)

Let us see again what happens when allowing our simulations to proceed for a longer time (the precise value will depend both on the gauge and the ordering parameter choices).

We see in Fig. 6.8 that the spurious oscillations do not show up anymore. What we see instead is a sort of rebound of the lapse, which looks like propagating backwards in time in the region near to $\rho = 2M$. This will be fatal for the simulation because, as discussed in Sect. 6.2.3, singularity-avoidant slicing conditions are devised for collapse problems and can produce a lapse blowup in the expanding regions.

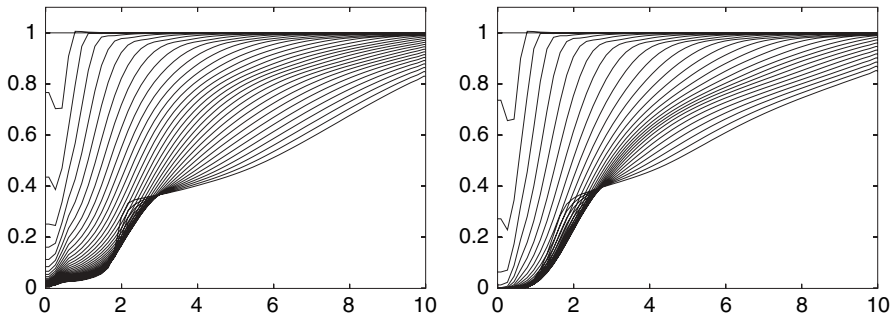

Fig. 6.8. Same as Fig. 6.7, but with the simulations running for a longer time ($t = 17M$ in the *left panel* and $t = 14M$ in the *right* one). No spurious oscillations appear anymore. However, the lapse collapse stops and a sort of rebound starts near the frozen innermost region. The lapse looks then just going backwards there: a runaway solution will appear causing the code to crash by a lapse blow-up

To understand what is going on, let us take a look to Fig. 6.9, where we have plotted the same quantities as in Fig. 6.6. As a word of caution, let us remember that the lapse in the innermost region is yet collapsed, so that the dynamics is frozen there. This means that the features we see in the innermost region in Fig. 6.9 correspond to an earlier stage (measured in proper time) than what we see around $\rho = 2M$, which is the region we are going to analyze now.

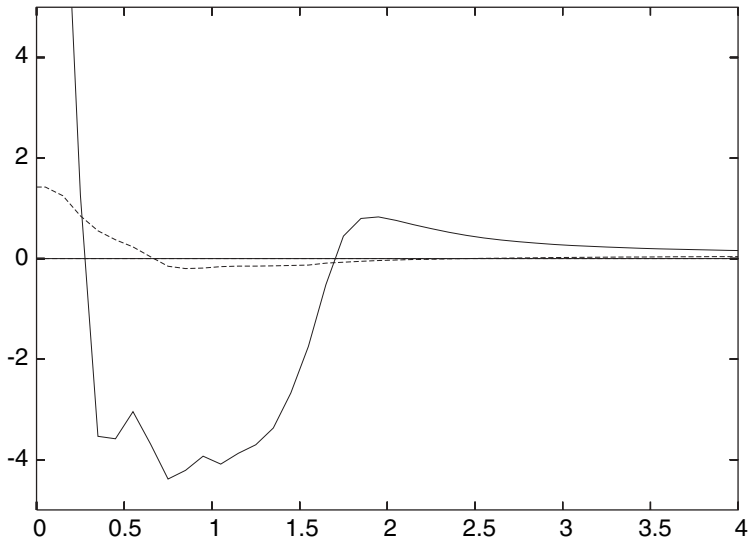

Fig. 6.9. Same as Fig. 6.6, but now for $t = 14M$, corresponding to the last plot in Fig. 6.8 (*right panel*). The dynamics in the innermost region is frozen (the lapse is fully collapsed there). In the region around $2M$, however, positive values of K_{xx} appear, corresponding to a radial collapse, whereas trK becomes negative, corresponding to a global expansion pattern. This is just the behavior opposite to slice stretching, and it explains the lapse rebound that can be seen in Fig. 6.8. Notice that the collapse pattern (positive trK values) is recovered in the outermost region, where the lapse collapse proceeds as expected

What we see there is just the opposite that what we saw in Fig. 6.6: trK is now negative, so that we have an overall expansion pattern. But the radial component (K_{xx} along the x direction) is collapsing. The geometrical meaning of this behavior can be better understood by looking again at the wormhole embedding diagram in Fig. 6.1. Remember that we visualized the slice stretching at the throat as a result of pulling up from the top. The rebound can be then interpreted as a sort of elastic response of the Black Hole geometry to that pull. The whole picture looks like moving backwards in time in the rebounding region.

We can circumvent the rebound problem by making use of the energy-constraint violations in the Black Hole interior. If we look at (6.55), we see some matter terms that are actually neglected in the Free Black-Hole scenario. This means that the energy constraint is not fulfilled inside the horizon and the value of the gauge parameter m is no longer irrelevant. For instance, neglecting the energy density terms in (6.55), as we do in the Free Black Hole case, amounts to add an $m-$dependent counter-term to the right-hand-side of the equation, namely

$$-\alpha \left(\frac{3}{2} - m\right) \tau \,, \tag{6.67}$$

which is contributing to the collapse for $m < 3/2$.

We show in Fig. 6.10 the same simulation as in (the left panel of) Fig. 6.8, but now with $m = -3$. Although the collapse is slowing down in the region between $2M$ and $3M$, it proceeds without showing any rebound, nor any other kind of gauge pathology. Notice however that the sequence of slices tends to cumulate in some regions (not only in the innermost one), signaling that the collapse is slowing down there.

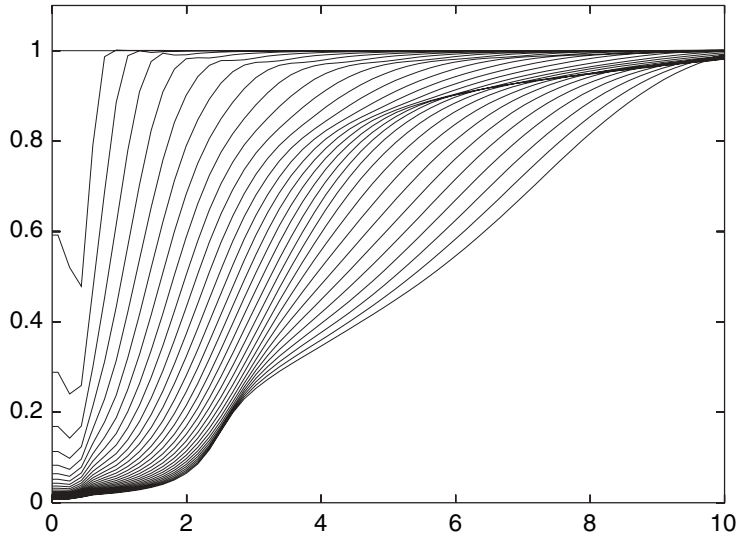

Fig. 6.10. Same as Fig. 6.8 (*left panel*), but now with the choice $m = -3$ for the second gauge parameter. The rebound no longer appears (the plots do not cross), although the collapse is slowing down at the regions where the different plots tend to cumulate

6.3.4 Boundary Conditions (30M and beyond)

Let us see once more what happens when allowing our simulations to proceed for an even longer time. We see in Fig. 6.11 that the lapse rebound does not show up anymore. What we see is the collapse of the whole computational region, which ends up completely inside the apparent horizon. At this point, one must remember that the lapse function provides the scale factor between coordinate and proper time: the lapse collapse in the outermost region in Fig. 6.11 means that proper time gets frozen there slightly above $30M$, whereas coordinate time goes till $50M$ and beyond.

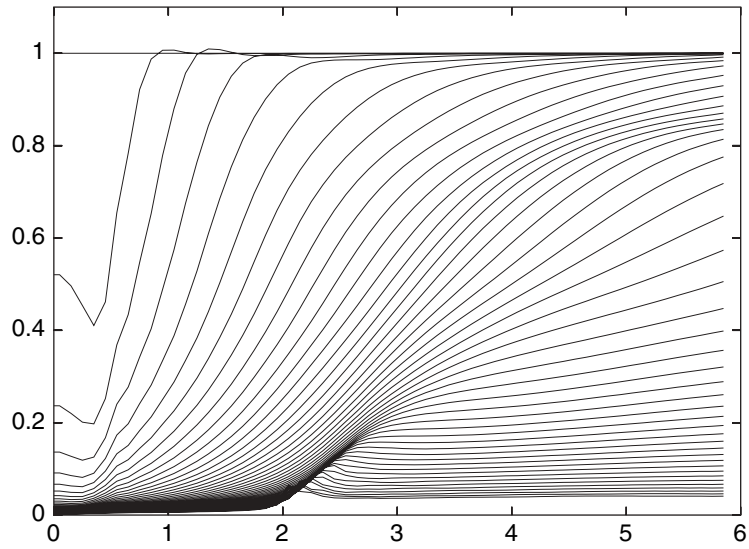

Fig. 6.11. Same as Fig. 6.10, but now running up to $50M$ (coordinate time at the outer boundary). The plots are shown now with a larger time interval in order to get a clearer picture. The whole computational region gets inside the Black Hole horizon. Notice that we show here a cut along one coordinate axis, not along the cube diagonal like we did in the previous figures. The outer boundary is then placed precisely at the plots endpoints ($\rho = 6M$)

When one reaches this point, two opposite thoughts come to the mind:

- A positive one: the proposed calculation has been completed. The main obstacles (spurious oscillations, gauge pathologies) have been passed. The boundary conditions (algebraic ones, remember) are doing a good job, even if the outer boundary is placed definitely too close, at $\rho = 6M$. So, it is an achievement.
- A negative one: even if one could evolve the Black Hole simulation further, this would be of no value for extracting any physical consequence for the

outside geometry. We have reached the limit of our (modest) computational resources.

As scientists, however, we will always try to overcome our limits. There is a number of ways in which we could do that in this case:

- **Getting more computational resources**. We can switch from our modest PC to a bigger computer, maybe just a PC cluster. This will allow to put the outer boundary farther away, so that we can model even Black Hole collisions and predict the waveforms of the resulting gravitational radiation [28, 55]. This is a limited improvement, however. Every factor 2 in resolution means a factor 2^3 in the number of nodes in a three-dimensional grid (this means 8 times the original memory requirements). Moreover, if one is using explicit finite-differences methods, there is an extra doubling on the number of required time steps, allowing for the Courant condition. This amounts to a 16 factor in the required computing power.
- **Implementing even better numerical methods**. In the CFD arsenal, we can find for instance Multi-Patch and Adaptive Mesh Refinement (AMR) methods [67, 68]. Instead of a homogeneous numerical grid, Multi-Patch methods make use of different coordinate patches (each one with its own adapted grid) to cover the computational region. AMR methods go even farther, by dynamically increasing (or decreasing) the grid resolution exactly where it is needed. These advanced techniques are devised in order to optimize the available computational resources at the cost of an extra load on the numerical algorithm.
- **Taking advantage of the space-coordinates degrees of freedom**. Instead of adapting the numerical grid, like in the AMR methods, one could just adapt the space coordinate system (and keep a simple, homogenous, grid). This could mean to provide a dynamical shift choice that drives grid points to the places where more resolution is needed [8, 9, 10]. Also, in Black Hole simulations, one expects the spacetime going through a highly dynamical transient phase, then approaching a quasi-stationary final stage. Coordinate choices in which the time lines tend to follow the corresponding 'quasi-Killing' vector would be of a great help in these cases.

The way ahead is by no means simple, no matter which one (or which combination) of the preceding options is chosen. The peculiarities of real physical applications will enter into the scene. Our hope is that at this point one should be familiar with the basic arsenal of Numerical Relativity tools. The door is wide open to more advanced developments.

References

1. H. Stephani et al: *Exact Solutions of Einstein's Field Equations*, 2nd edn (Cambridge, Cambridge New York 2003)
2. http://www.ligo.caltech.edu.
   http://www.virgo.infn.it.
   http://www.geo600.uni-hannover.de.
   http://tamago.mtk.nao.ac.jp.
3. http://www.minigrail.nl/
   http://www.das.inpe.br/ graviton/English/
   http://www.roma1.infn.it/rog/nautilus/nautilus.html
   http://www.roma1.infn.it/rog/explorer/explorer.html
   http://sam.phys.lsu.edu/
   http://www.gravity.uwa.edu.au/bar/bar.html
   http://www.auriga.lnl.infn.it/
4. A. Lichnerowicz, J. Math. Pures et Appl. **23**, 37 (1944).
5. Y. Choquet-Bruhat: J. Rat. Mec. Analysis **5**, 951 (1956).
6. R. Arnowit, S. Deser and C. W. Misner. In: *Gravitation: an introduction to current research*, ed. by L. Witten, Wiley, (New York 1962).
7. R. Gomez et al., Phys. Rev. Lett. **80**, 3915 (1998).
8. M. Alcubierre and B. Brugmann, Phys. Rev. **D63**, 104006 (2001).
9. M. Alcubierre et al, Phys. Rev. **D67**, 084023 (2003).
10. L. Lindblom and M. A. Scheel, Phys. Rev. **D67** 124005 (2003).
11. J. Centrella, Phys. Rev. **D21**, 2776 (1980).
12. L. Smarr and J. W. York, Phys. Rev. **D17**, 1945 (1978), Phys. Rev. **D17**, 2529 (1978).
13. P. Anninos et al., Phys. Rev. Lett **71**, 2851 (1993),
14. H. O. Kreiss and J. Lorentz, *Initial-Boundary problems and the Navier-Stokes equations*, Academic Press, New York (1989).
15. M. Alcubierre et al, Class. Quantum. Grav. **21**, 589 (2004).
16. O. A. Liskovets, Differential equations I 1308-1323 (1965).
17. S. Gottlieb, C. -W. Shu and E. Tadmor, SIAM Review **43**, 89 (2001).
18. W. H. Press, B. P. Flannery, S. A. Teukolsky and W. T. Veterling, *Numerical Recipes*, Cambridge, Cambridge (1989).
19. B. Gustafson, H. O. Kreiss and J. Oliger, *Time dependent problems and difference methods*, Wiley, New York (1995).

20. T. De Donder, *La Gravifique Einstenienne* Gauthier-Villars, Paris (1921).
21. V. A. Fock, *The theory of Space, Time and Gravitation*, Pergamon, London (1959).
22. C. Bona and J. Massó, Phys. Rev. Lett. **68** 1097 (1992)
23. C. Bona, J. Massó, E. Seidel and J. Stela, Phys. Rev. Lett. **75** 600 (1995).
24. M. Shibata and T. Nakamura, Phys. Rev. **D52** 5428 (1995).
25. T. W. Baumgarte and S. L. Shapiro, Phys. Rev. **D59** 024007 (1999).
26. A. Arbona, C. Bona, J. Massó and J. Stela, Phys. Rev. **D60** 104014 (1999).
27. M. Alcubierre et al. , Phys. Rev. **D64** 061501 (2001).
28. M. Alcubierre et al. , Phys. Rev. Lett **87** 271103 (2001).
29. C. Bona, T. Ledvinka, C. Palenzuela, M. Žáček, Phys. Rev. **D67** 104005 (2003).
30. C. Bona, T. Ledvinka, C. Palenzuela, M. Žáček, Phys. Rev. **D69** 064036 (2004).
31. L. E. Kidder, M. A. Scheel and S. A. Teukolsky, Phys. Rev. **D64** 064017 (2001).
32. O. Sarbach and M. Tiglio, Phys. Rev. D**66** 064023 (2002).
33. R. J. LeVeque, in *Numerical methods for conservation laws*, Birkhauser, Basel, (1992).
34. E. Toro, *Riemann Solvers and Numerical Methods for Fluid Dynamics*, Springer, Berlin Heidelberg (1997).
35. R. Donat and A. Marquina, J. Comp. Phys. **125**, 42 (1996).
36. B. van Leer, J. Comput. Phys. **23**, 276 (1977).
37. Y. Choquet-Bruhat and T. Ruggeri, Comm. Math. Phys. **89**, 269 (1983).
38. S. Frittelli and O. A. Reula, Commun. Math. Phys. **166** 221 (1994).
39. S. Frittelli and O. A. Reula, Phys. Rev. Lett. **76** 4667 (1996).
40. O. Brodbeck, S. Frittelli, P. Hubner and O. Reula, J. Math. Phys. 40, 909–923 (1999).
41. A. Anderson and J. W. York, Jr., Phys. Rev. Lett. **82** 4384 (1999).
42. S. D. Hern: Numerical Relativity and Inhomogeneous Cosmologies. Ph. D. Thesis, gr-qc/0004036 (2000).
43. K. Alvi, Class. Quantum Grav, **19** 5153 (2002).
44. A. Abrahams, A. Anderson, Y. Choquet-Bruhat and J. W. York, Phys. Rev. Lett. **75**, 3377 (1995).
45. H. Friedrich, Class. Quantum. Grav. **13**, 1451 (1996).
46. M. H. P. van Putten and D. M. Eardley, Phys. Rev. **D53**, 3056 (1996).
47. M. H. P. van Putten, Phys. Rev. **D55**, 4705 (1997).
48. F. Banyuls, J. A. Font, J. M. Ibáñez, J. M. Martí, and J. A. Miralles, Astrophys. J. **476**, 221 (1997).
49. P. Olsson, Mathematics of Computation **64**, 1035 (1995).
50. H. Friedrich: "Conformal Einstein evolution". In: *The conformal structure of space-times: Geometry, Analysis, Numerics*, ed by J. Frauendiener and H. Friedrich, Springer Lecture Notes in Physics, vol 604 (Springer, Berlin Heidelberg New York 2002) pp 1–50.
51. J. Baker, B. Brügmann, M. Campanelli and C. O. Lousto, Class. Quantum Grav. **17**, L149 (2000).
52. J. Baker, M. Campanelli and C. O. Lousto, Phys. Rev. **D65**, 044001 (2002).
53. G. Calabrese et al. , Commun. Math. Phys. **240**, 377 (2003).
54. R. Beig and N. O Murchadha, Class. Quantum Grav. **11**, 419 (1994).
Class. Quantum Grav. **13**, 739 (1996).
55. P. Anninos et al. , Phys. Rev. **D52**, 2059 (1995).
56. B. Brügmann, Int. J. Mod. Phys. **D8**, 85 (1999).

57. P. Anninos et al., Phys. Rev. Lett. **74**, 630 (1995).
58. J. Libson et al., Phys. Rev. **D53**, 4335 (1996).
59. J. Thornburg, Class. Quan. Grav. **4**, (1987).
60. C. Bona, J. Massó, E. Seidel and J. Stela, Phys. Rev. **D56**, 3405 (1997).
61. E. Seidel and W. M. Suen, Phys. Rev. Lett. **69**, 1845 (1992).
62. A. Arbona et al., Phys. Rev. **D57**, 2397 (1998).
63. C. Bona and J. Massó, Phys. Rev. **D38**, 2419 (1988).
64. F. Estabrook et al., Phys. Rev. **D7**, 2814 (1973).
65. M. Alcubierre, Phys. Rev. **D55**, 5981 (1997).
66. M. Alcubierre, Class. Quantum Grav. **20**, 607 (2003).
67. M. J. Berger and R. J. LeVeque, SIAM Journal of Numerical Analysis **35**, 2298 (1998).
68. F. Pretorius and L. Lehner, J. Comput. Phys. **198**, 10 (2004).

Index